ALTERING THE SURFACE AND INTERLAYER COMPOSITION OF 2D MATERIALS

Kaci Lee Kuntz

A dissertation submitted to the faculty of the University of North Carolina at Chapel Hill in partial fulfillment of the requirements for the degree of Doctor of Philosophy in the Department of Chemistry.

Chapel Hill
2019

Approved by:

Scott C. Warren

Joanna M. Atkin

Carrie L. Donley

Jillian L. Dempsey

Jinsong Huang

©2019
Kaci Lee Kuntz
ALL RIGHTS RESERVED

ABSTRACT

Kaci L. Kuntz: Altering the Surface and Interlayer Composition of 2D Materials
(Under the direction of Scott C. Warren)

The use of two-dimensional nanomaterials in technology, such as plasmonic sensors and optoelectronic devices, requires precise control of composition and dimensions. The large surface area of 2D materials naturally creates opportunities to investigate surface science and intrinsic quasi-surface science in ultra thin samples. As a species is brought in contact with these materials, either at the surface or an interlayer space, charge transfer may occur. The extent of this charge transfer can alter the carrier concentration of the material, effectively doping it. However, if this charge transfer is large in magnitude, it may also lead to a chemical reaction and a physical change of the surface composition. Here, I investigate 2D materials after these charge transfer events (e.g. surface and interlayer composition, and carrier concentration). Specifically, I focus on altering the carrier concentration of graphene though various methods and explore the role of the physical dimensions on the emerging properties. Additionally, I characterize the composition of a 2D material as it is oxidizes due to charge transfer with oxidant species and then spatially-resolve the resulting surface oxide composition.

Graphene is a semi-metal with a carrier concentration of $\sim 10^{12}$ cm^{-2}; however by altering the carrier concentration of this 2D material, it can become metallic. When graphene is doped, it behaves as an exceptional plasmonic material, demonstrating tunable plasmons in the THz and mid-infrared regimes. Despite investigation of graphene plasmons in various arrays, there is limited research in anti-dot (e.g. hole or nanomesh) lattices, especially at very high carrier concentrations. Here, we explore the plasmons that emerge in graphene anti-dot lattices, with low to high levels of doping (0.1–1.35 eV) corresponding to in-plane carrier concentrations of $1 \cdot 10^{12}$—$5 \cdot 10^{14}$ cm^{-2}. Furthermore, we investigate the effect of geometric variations (i.e. radius, periodicity, number of layers) on the the plasmon resonance. We find that the plasmon resonance of these few-layer, anti-dot lattices can be blue-shifted well into the near infrared regions of the electromagnetic spectrum by varying geometric parameters and levels of doping, opening new opportunities for graphene in

NIR plasmonics. Finally, we propose methods to further increase tunability, potentially enabling this material to have a plasmon in the visible spectrum, as well as schemes to realize these structures experimentally.

Phosphorene is emerging as an important two-dimensional semiconductor, but controlling the surface chemistry of phosphorene remains a significant challenge. This material readily undergoes surface degradation in ambient environments, due to significant charge transfer events with oxidants. Here we show that controlled oxidation of phosphorene determines the composition and spatial distribution of the resulting oxide. We used X-ray photoemission spectroscopy to measure the binding energy shifts that accompany oxidation. We interpreted these spectra by calculating the binding energy shift for 24 likely bonding configurations, including phosphorus oxides and hydroxides located on the basal surface or edges of flakes. After brief exposure to high-purity oxygen or high-purity water vapor at room temperature, we observed phosphorus in the +1 and +2 oxidation states; longer exposures led to a large population of phosphorus in the +3 oxidation state. To provide insight into the spatial distribution of the oxide, transmission electron microscopy was performed at several stages during the oxidation. We found crucial differences between oxygen and water oxidants: while pure oxygen produced an oxide layer on the van der Waals surface, water oxidized the material at pre-existing defects, such as edges or steps. We propose a mechanism based on the thermodynamics of electron transfer to interpret these observations. This work opens a route to functionalize the basal surface or edges of 2D black phosphorus through site-selective chemical reactions and presents the opportunity to explore the synthesis of 2D phosphorene oxide by oxidation.

To my family and my mentors.

ACKNOWLEDGEMENTS

First and foremost, I must thank my husband, Alan, and my son, Elias. Your unending support and love are the reasons I was able to pursue my doctorate. I appreciate you both more than I can express.

To my advisor—Scott C. Warren, thank you for your guidance in my research and helping me develop the skills I need for success in my career. Most of all, thank you for fostering an environment where I was free to explore, free to fail, and free to excel as a scientist.

To my previous mentors—Dr. Peng Zhang and Mr. Robert Cope, thank you for encouraging me to pursue my love of chemistry. Thank you for seeing my potential and leading me in the right direction.

Additionally, I want to thank Dr. Carrie Donley for her assistance in learning and interpreting photoemission spectroscopy. Additionally, I appreciate the assistance of Dr. Bob Geil, Dr. Amar Kumbar, Dr. Wallace Ambrose, and Dr. Jun Yan. The assistance and knowledge of each of these individuals are invaluable assests to research at UNC.

Finally, I would like to thank all of the Warren lab members, especially Bernadette Lee, Jennifer Zou, Elena Kovalik, and Carolyn Chen. To each of my mentees–I appreciate all of your diligent efforts in lab and your patience with me as I learned to be a better mentor. Thank you all for the fruitful discussions and encouragement over the last few years. It has been a privilege doing research at UNC.

TABLE OF CONTENTS

LIST OF TABLES xi

LIST OF FIGURES xii

LIST OF ABBREVIATIONS xiv

1 INTRODUCTION 1

1.1 Layered Materials 1

1.1.1 Two-dimensional Materials 1

1.2 Tuning Properties of 2D Materials 3

1.2.1 Oxidation, Reduction, & Carrier Concentration of 2D Materials 4

1.2.1.1 Optical Response to Carrier Concentration 4

1.2.1.2 Electrostatic Doping 5

1.2.1.3 Electrochemical Doping 6

1.2.2 Surface Composition 8

1.2.2.1 Oxidation of 2D Black Phosphorus 8

2 METHODS 9

2.1 Bulk Material 9

2.1.1 Synthesis by Chemical Vapor Transport 9

2.1.1.1 BP CVT Synthesis 10

2.1.1.2 MoS_2 CVT Synthesis 11

2.2 Exfoliation of Bulk Material 12

2.2.1 Mechanical Exfoliation 13

2.2.1.1 Monolayer Method 14

2.2.1.2 Consistent-thickness Method 15
2.2.1.3 Transfer & Cleaning 15
2.2.2 Liquid Exfoliation 16
2.2.2.1 Liquid Exfoliation of BP 17
2.2.3 Electrochemical Exfoliation 17
2.3 2D Flakes 18
2.3.1 Substrate Preparation 18
2.3.1.1 Marker Pattern Microfabrication 19
2.3.2 Doctor Blade Technique 21
2.3.3 Drop-casting 21
2.3.4 Sealed Inert Environments 22
2.3.4.1 Epoxy Selection 23
2.4 Oxidation of 2D Black Phosphorus 24
2.5 2D Flake Characterization 25
2.5.1 Optical Microscopy Images 26
2.5.1.1 Bright-field and Dark-field Microscopy 26
2.5.1.2 Lateral Dimensions 27
2.5.2 TEM 27
2.5.2.1 TEM: Black Phosphorus Oxides 27
2.5.2.2 TEM Image Processing 28
2.5.2.3 Diffraction: Black Phosphorus Oxides 29
2.5.3 XPS & UPS 30
2.5.3.1 Introduction to XPS 30
2.5.3.2 Quantification of Composition 30
2.5.3.3 Composition of 2D Material Surfaces by XPS 31
2.5.3.4 Charging 33
2.5.3.5 Differential Charging 34
2.5.3.6 Differential Charging in 2D Electrides 34

2.5.3.7 Introduction to UPS 35
2.5.3.8 Metallic Nature of 2D Ca_2N by UPS 36
2.5.4 UPS & Band Diagram 37
2.5.5 DFT 38
2.5.6 Raman Spectroscopy 39
2.5.6.1 Raman Spectroscopy of 2D BP & Oxide 41
2.6 Simulations of Optical Response to Carrier Concentration 42
2.6.1 Simulation Environment 42
2.6.1.1 FDTD Region 43
2.6.1.2 Meshing and Mesh Order 44
2.6.2 Doping & Refractive Indicies 45
2.6.2.1 Electrostatically Doped-Graphene: Conductivity Model 45
2.6.3 Electrochemically Doped-Graphene: Drude Model of KC_8 46
2.6.4 Parameter Space 47
2.7 Experimentally Altering Carrier Concentration 48
2.7.1 Thermal Intercalation 48
2.7.2 Electrochemical Intercalation 48
2.7.2.1 Planar Battery Cell 49
2.7.2.2 *In situ* Raman Spectroscopy 49
3 CONTROL OF SURFACE AND EDGE OXIDATION PHOSPHORENE 51
3.1 Introduction 51
3.2 Experimental Section 54
3.2.1 Material Preparation 54
3.2.2 Oxidant Exposure 54
3.2.3 Characterization 55
3.3 Results & Discussion 55
3.3.1 XPS Characterization 55

3.3.2 Time-lapsed TEM 57
3.3.3 Binding energy shift, ΔE_B^F, of Phosphorus Oxides 59
3.3.4 Deconvolution of XPS Spectra 64
3.3.5 Mechanism of Oxidation by O_2 or H_2O 64
3.4 Conclusion 68
4 TUNING THE PLASMON RESONANCE OF FEW-LAYER GRAPHENE ANTI-DOT ARRAYS 69
4.1 Introduction 69
4.2 Background 69
4.3 Experimental Methods 70
4.3.1 Refractive Index of Doped-Graphene 72
4.4 Results & Discussion 73
4.5 Conclusion 78
BIBLIOGRAPHY 79

LIST OF TABLES

2.1 XPS binding energies (eV) of Ca 2p electrons from Ca_2N & oxides 32

2.2 Percent of phosphorus oxides on thin films of 2D BP 33

3.1 Observed oxidation mechanisms in ambient conditions for 1—100 hours 59

3.2 Absolute reduction potentials E_{abs} at 25°C 65

LIST OF FIGURES

1.1 Layered Materials: 3D vs. 2D 2

1.2 Structure and Band Gap of 2D Materials 3

1.3 Density of States of Graphite with Electrochemical Doping 4

1.4 Tuning Carrier Concentration by Electrostatic Doping 6

1.5 Tuning Carrier Concentration by Intercalation 7

2.1 Mechanical Exfoliation Methods 14

2.2 Microfabricated Marker Patterns 20

2.3 Thin Film Assembly: Doctor Blade Technique 21

2.4 Sealed Inert Samples for Characterization 22

2.5 Oxidation of Thin Films of BP 25

2.6 Optical Microscopy: Bright-field & Dark-field 27

2.7 TEM: Image Processing 29

2.8 TEM: Diffraction Pattern 29

2.9 XPS: Core Electron Photoejection 30

2.10 XPS: Ca_2N 32

2.11 UPS: Differential Charging in Electrides 35

2.12 UPS: Metallic Nature of Ca_2N 37

2.13 DFT: Equivalent Cores Approximation 39

2.14 Raman Spectroscopy 40

2.15 Raman Spectroscopy: Oxidized 2D BP 42

2.16 FDTD Simulation Environment 43

2.17 Refractive Index of Graphene, KC_8, and Metals 47

2.18 *In situ* Raman Spectroscopy of Intercalation 50

3.1 Liquid exfoliation of black phosphorus and characterization of thin films 54

3.2 XPS Spectra of 2D Black Phosphorus Exposed to Different Oxidants 56

3.3 TEM Images of 2D Black Phosphorus Exposed to Different Oxidants 58
3.4 Depiction of the Thermodynamic Born-Haber Cycle for Oxidized Phosphorene 61
3.5 Deconvolution of XPS Spectra of Oxidized Phosphorene 63
3.6 Oxidation Mechanism of 2D Black Phosphorus Flakes 67

4.1 Simulations of Graphene Anti-dot Structure 71
4.2 Relationships of Plasmon Resonance & Doping 75
4.3 Geometric Effects on Plasmon Resonance 77

LIST OF ABBREVIATIONS

2D	two-dimensional
3D	three-dimensional
A	area
AFM	atomic force microscopy
BFM	bright-field microscopy
BP	black phosphorus
CV	cyclic voltammetry
CVT	chemical vapor transport
CP	chronopotentiometry
DFM	dark-field microscopy
D	diameter
DFT	density functional theory
e	charge of an electron
ε_o	permittivity of free space
E	edge-to-edge distance
E	reduction potential
E^o	standard reduction potential
E_{abs}	absolute vacuum level
E_B^F	core electron binding energy
EBL	electron-beam lithography
E_F	Fermi energy
E_K	kinetic energy
E_{SECO}	secondary electron cut-off energy
FDTD	finite-difference time domain
FIR	far-infrared
FL	few-layer
FWHM	full-width at half-maximum
GIC	graphite intercalation compound

GO	graphene oxide
h	Planck's constant
$\hbar$	reduced Planck's constant
hBN	hexagonal boron nitride
HS	heterostructure
IPA	isopropyl alcohol
IR	infrared
k_B	Boltzmann constant
λ_o	excitation wavelength
m	mass of an electron
MIR	mid-infrared
MIBK	methyl isobutyl ketone
MMA	methyl methacrylate
N	carrier concentration
NA	numerical aperture
n_e	number of electrons
NHE	normal hydrogen electrode
NIR	near-infrared
NMP	*N*-methyl-2-pyrrolidone
NPGS	Nanometer Pattern Generation System
NTO	Nb-doped tin oxide
ν	frequency
NUV	near-ultraviolet
P	periodicity
PAW	projector augmented wave
PBE	Perdew-Burke-Ernzerhof
PML	perfectly matched layer
PMMA	poly(methyl methacrylate)
PV	photovoltaic

Q	reaction quotient
%R	percent reflection
R	ideal gas constant
R	spatial resolution
rpm	revolutions per minute
SEM	scanning electron microscope
SHE	standard hydrogen electrode
s-SNOM	scattering-scanning near-field optical microscopy
%T	percent transmission
T	temperature
T_b	boiling temperature
TEM	transmission electron microscope
THz	terahertz
T_m	melting temperature
UPS	ultraviolet photoemission spectroscopy
UV	ultraviolet
vdW	van der Waals
v_F	fermi velocity
VIS	visible
V	voltage
ϕ	work function
WD	working distance
ω_p	plasmon frequency
XPS	X-ray photoemission spectroscopy

INTRODUCTION

"The greatest challenge to any thinker is stating the problem in a way that will allow a solution"

- Bertrand Russell

1.1 Layered Materials

The structure of layered materials enables interesting research avenues from optical switches[1–4] to memristors[5] to batteries[1,6,7] to drug delivery.[8–10] In these materials, the interactions within a layer are stronger than interactions between layers (Figure 1.1a). For example, graphite has strong intralayer covalent bonds between carbon atoms while only weak van der Waals (vdW) interlayer interactions are present between adjacent layers. Therefore, many of these structures can be cleaved along the weaker interlayer interactions to yield thin, two-dimensional (2D) materials.

1.1.1 Two-dimensional Materials

In 2004, an atomically-thin layer to graphite with a thickness of 0.34 nm, commonly known as graphene, was experimentally observed.[11] Interestingly, as graphite is thinned to graphene, some properties are maintained while others are altered. For example, graphite is a grey and reflective semimetal with high mobility and conductivity (Figure 1.1b,c). As graphite is cleaved to $\leq$10 layers, ($\approx$3.4 nm), different properties emerge, which are indicative of the transition to 2D. More specifically, the material becomes nearly transparent (Figure 1.1b,c) and an induced infrared (IR) tunable band gap as a monolayer has been observed (Figure 1.2).[12,13] Furthermore, few-layer (FL) graphite and graphene retain some properties of its bulk counterpart, such as its semi-metallic electronic nature and ultra-high mobility.[14–16]

[1]Portions of this chapter reproduced from Stark, M. S.; Kuntz, K. L.; Martens, S. J.; Warren, S. C. Intercalation of Layered Materials from Bulk to 2D. *Advanced Materials* **2019**, *1808213*. Copyright WILEY-VCH Verlag GmbH & Co. KGaA, Weinheim.

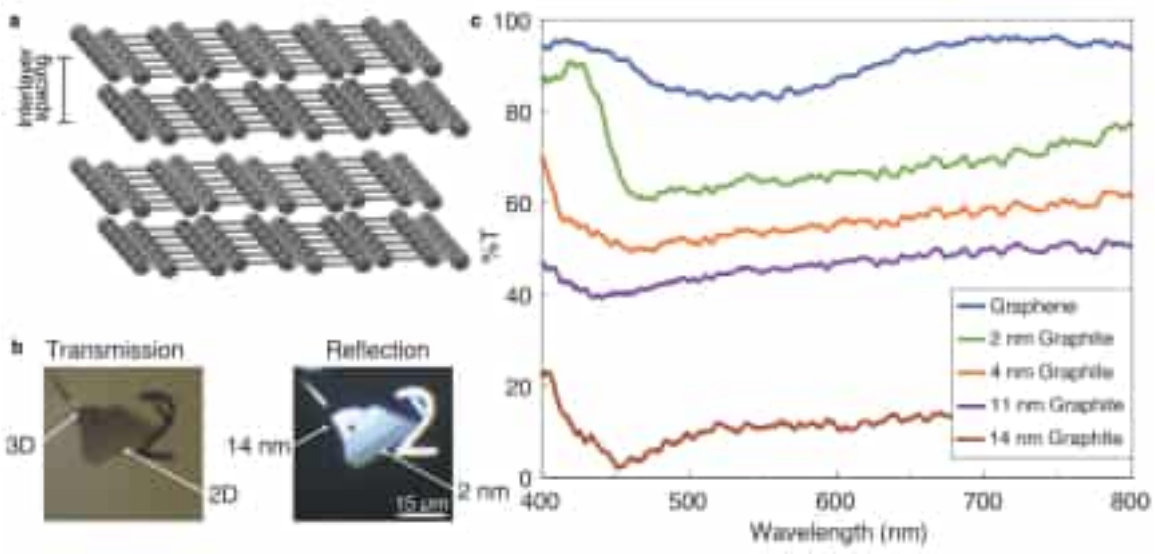


Figure 1.1: Graphite is (a) a layered structure with strong intralayer bonds and weak interlayer interactions that can be cleaved along the interlayer interface. As the material is cleaved, transitioning from 3D to 2D, the material changes from (b) highly reflective to highly transparent. In the bright-field microscopy (BFM) images, in transmission mode, thicker material appears dark and thinner material is lighter on the transparent glass slide. In reflection images, thicker material appears brighter as more light is reflected than thinner materials. With each successive removal of a layer(s), (c) the transmission %T increases until it is nearly transparent as a monolayer of graphene.

Since the discovery of graphene, many other types of 2D materials have been observed (e.g. insulator, semiconductor, metal). With the continual expansion of known 2D materials, new and novel properties that are dependent on each material, its dimensions, and its environment are being discovered. For example, the semiconductor, MoS_2, has an indirect band gap in the bulk layered structure, but a direct band gap as a monolayer which leads to photoluminesence (Figure 1.2b,c).[17–20] Interestingly, the stacking of 2D dissimilar materials, known as vdW heterostructures, emerged as a new research field.[21] These structures can demonstrate improved properties or the emergence of new ones that are not inherent to any single material within the vdW structure. For example, when graphene is placed on FL hexagonal boron nitride (hBN) (Figure 1.2c)–an insulator–the electronic properties of graphene are improved by an order of magnitude.[21,22] This highlights the importance of surface interactions and the surrounding environment of 2D materials and vdW heterostructures. Furthermore, properties of these materials can be altered by adding in dopants, surface modifications, or even interlayer species.[22–25] The diverse avenues to alter 2D materials make them desirable for applications of ultra-thin, tunable devices.

1.2 Tuning Properties of 2D Materials

The emergence of 2D materials is now creating exciting opportunities to address fundamental questions in this new regime such as how properties depend on material dimensions, composition, and the interlayer space. This leads to interesting avenues of research, characterizing and then engineering properties of 2D materials through thickness or lateral size, surface alteration, doping, or modification of the interlayer space by intercalation or stacking of 2D materials. An example of a 2D material that demonstrates highly-tunable properties through its size, surface, and interlayer composition is the semiconductor, black phosphorus (BP).

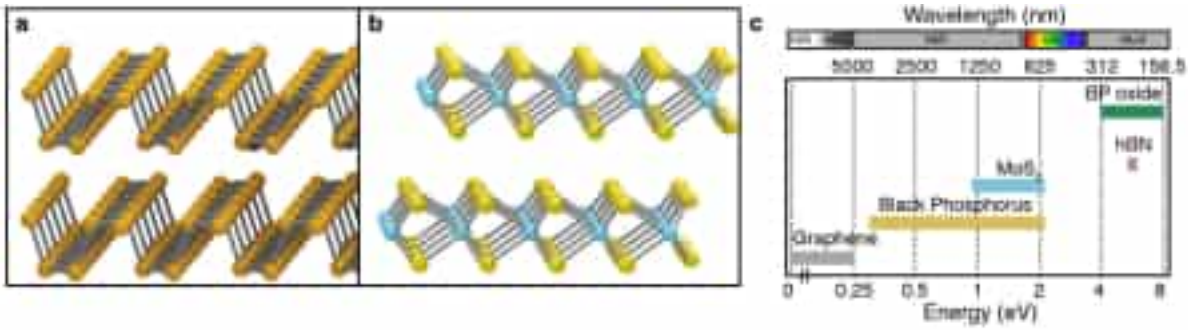


Figure 1.2: Structure of bilayers of 2D semiconductors: (a) Orthorhombic, puckered crystal structure of black phosphorus, where the yellow atoms represent P and (b) hexagonal crystal structure of MoS_2 where the outer, yellow atoms represent S and middle blue atoms represent Mo. (c) Band gap ranges of select monolayer to bulk layered materials, as well as their respective oxides.

BP is a layered orthorhombic crystal, shown in Figure 1.2a; its structural anisotropy results in properties that are sensitive to the number of layers[26], the surface composition[24], and the carrier concentration[27–29]. BP is a semiconductor with a thickness-dependent band structure, exhibiting a mid-infrared (MIR) band gap of 0.3 eV in bulk form and a visible (VIS) band gap of approximately 2.1 eV as a monolayer (Figure 1.2c).[26,30–34] Interestingly, BP is easily oxidized in the presence of O_2 or H_2O, which can be exploited to yield an insulating surface oxide.[24] Furthermore, this oxide can have a large band gap that is dependent on the composition ratio of P:O, resulting in a band gap between $\sim$4 to 8.6 eV (Figure 1.2c).[35,36] Finally, the carrier concentration of the material can be altered, doping it by intercalating a guest species into the interlayer space (Figure 1.5), where the resulting properties will depend on the identity of the species in the interlayer space. Recently, potassium was incorporated into the interlayer space, resulting in an increase in the carrier concentration and a semi-metallic material.[37] BP is an interesting layered material with properties that can be engineered in the

2D realm by altering its thickness, surface composition, and carrier concentration. By selectively altering one of these parameters, the 2D material can be tuned from semi-metallic to semiconducting to highly insulating.

1.2.1 Oxidation, Reduction, & Carrier Concentration of 2D Materials

Because of the ultra-thin dimension of 2D materials, changes of the carrier concentration can drastically alter properties. For example, by electrostatically increasing the carrier concentration of graphene, the zero-gap semimetal (Figure 1.3) can become a semiconductor with an induced band gap of $\sim$0.25 eV (Figure 1.2).[12,13]. Additionally, by adding electron-withdrawing or electron-donating species to the surface or interlayer space of 2D materials, the carrier concentration will change, altering the electronic and optical properties. For example, when an electron-acceptor or electron-donor is adhered onto the surface or incorporated within the interlayer space of FL or 2D graphite,[38–41] the material becomes metallic due to the increase in charge carrier density surrounding the Fermi energy level E_F (Figure 1.3).[41] These methods of tuning the carrier concentration can be divided into two classes: electrostatic (Section 1.2.1.2) or electrochemical (Section 1.2.1.3).

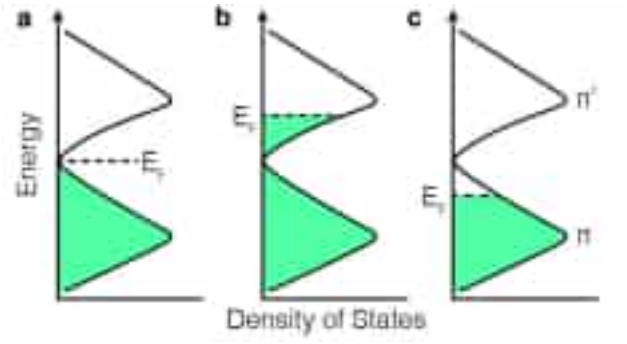


Figure 1.3: The density of states of (a) graphite with electrochemical doping by (b) electrons and (c) holes at 0 K, depicting the shift of E_F with respect to the bonding π-type and antibonding π^*-type bands.

1.2.1.1 Optical Response to Carrier Concentration

The plasma frequency ω_p of a metal is dependent on the concentration of charge carriers N, according to the Drude model, shown in Equation 1.1,

$$\omega_p = \sqrt{\frac{Ne^2}{\epsilon_o m}} \tag{1.1}$$

where e is the charge of an electron, ϵ_o is the permittivity of free space, and m is the effective mass of an electron. Furthermore, metallic structures with dimensions smaller than the wavelength of incident light

(e.g. a 25 nm particle and 460 nm incident light) can have a collective response of electrons, oscillating at a frequency identical to an incident light excitation; this is known as a localized surface plasmon. Additionally, the E_F scales with the square root of the N, shown in Equation 4.2,

$$E_F = \hbar v_F \sqrt{\pi N} \tag{1.2}$$

where $\hbar$ is the reduced Planck's constant and v_F is the fermi velocity. Therefore, the E_F scales linearly with the plasmon resonance. Thus, by tuning the N, the E_F and optical response of a material can be tuned.

To demonstrate the tuning optical responses to carrier concentration, consider metallic and semi-metallic plasmonic materials. Noble metals, such as silver and gold have a high carrier concentration ($\sim 6 \cdot 10^{22}$ cm^{-3});[42] therefore, their plasmonic response is at a higher energy within visible spectra.[43] In contrast to these metals, graphene is a 2D semimetal with a carrier concentration of $2 \cdot 10^{19}$ cm^{-3}.[1,44] This lower carrier concentration leads to a plasmon frequency at lower energies in the THz.[45,46] In graphene, the linear band dispersion around the E_F (Figure 1.3) enable the plasmonic response of this 2D material to be readily altered with small changes in the carrier concentration, shifting from the THz[45,46] to the MIR[47–51] region. However, plasmonic responses with high levels of doping remain unexplored.

Most commonly, plasmon frequencies are tuned by altering the N through electrostatic[52] or electrochemical doping[53,54] or reducing the dimensions[13] of a structure. Therefore, 2D materials are an ideal candidate for investigating the tunability of plasmonic responses of large area, ultra-thin materials.

1.2.1.2 Electrostatic Doping

Electrostatic doping allows for the carrier concentration to be altered by an external voltage source (Figure 1.4), where the applied voltage determines whether the material is doped with electrons or holes. Furthermore, this explicit control of the carrier concentration enables *in situ* characterization of the material's response. Since the N is related to the ω_p of a material according to Equation 1.1, as the carrier concentration of a material increases, the plasmonic response shifts to higher energies, depicted in Figure 1.4b. Electrostatic doping of, such as that of graphene nanoribbons, can enable optical responses that can be used in sensing applications.[49]

However, when a 2D material is doped, the E_F shifts due to the change in the carrier concentration, which affects absorption processes.[43] However, at low levels of doping, such as those attainable with electrostatic

techniques, interband transitions can be minimized and intraband transitions allow for the application of the Drude model to these systems. In order to investigate the optical response of 2D and FL materials with interesting structures, we employ simulations at different levels of electrostatic doping.

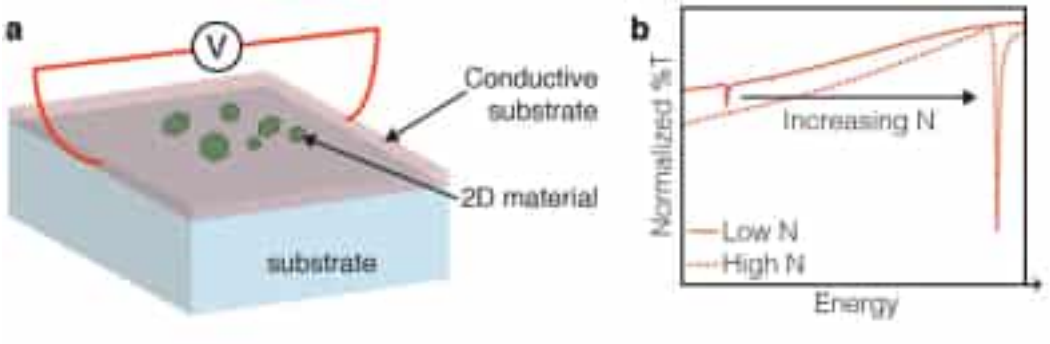


Figure 1.4: The carrier concentration can be altered by (a) applying an external voltage source to a conductive substrate with 2D material, changing the N of the 2D material. (b) As N increases, the ω_p increases.

1.2.1.3 Electrochemical Doping

Electrochemical processes involve the transfer of charge between two chemical species. One interesting example of this is the process of intercalation, which is the insertion of guest species into the void space of a host. The magnitude of charge transfer between the host and intercalant alters the carrier concentration, and can profoundly alter the chemical, electrical, optical, and magnetic properties. Here, simulations and experiments are employed to investigate electrochemically-doped 2D and FL compounds.

Layered materials are promising hosts for intercalation because of the weak vdW interlayer interactions that allow the lattices to readily expand (Figure 1.5a) and the guest to diffuse. As guest species insert into the interlayer gap of a layered host, the chemical and physical properties are radically altered as charge is transferred between the materials.[39,55,56] Depending on the nature of the intercalant and the host, a donor or acceptor intercalation compound forms. The charge transfer between the guest and host is described from the perspective of the intercalant. For example, in donor-type compounds, the guest species (D) donate electrons to the host layer (H), as shown in Equation 1.3. However, in acceptor compounds, the inserted species (A) accept electrons from H, as shown in Equation 1.4.

$$H_x + D \rightleftharpoons H_x^- \cdot D^+ \tag{1.3}$$

$$H_x + A \rightleftharpoons H_x^+ \cdot A^- \tag{1.4}$$

An example of this is shown in Figure 1.5. Graphite is a grey semimetal with an in-plane carrier concentration of $5.5 \cdot 10^{12}$ electrons cm^{-2},[1,44] while potassium-intercalated graphite KC_8 is a golden metal with a carrier concentration of $5 \cdot 10^{14}$ electrons cm^{-2} (Figure 1.5b).[1] This substantial increase in carrier concentration shifts the plasmon frequency from the MIR to the VIS spectrum (Figure 1.5a), according to Equation 1.1. As can be seen in Figure 1.5b, the reflection of graphite or FL graphene is grey while the that of KC_8 is golden. However, the transmission of graphite is negligible, while that of KC_8 is blue and can be attributed to the shift of the plasmon to a blue frequency. Here, we explore electrochemical doping as an approach to tune properties of 2D materials.

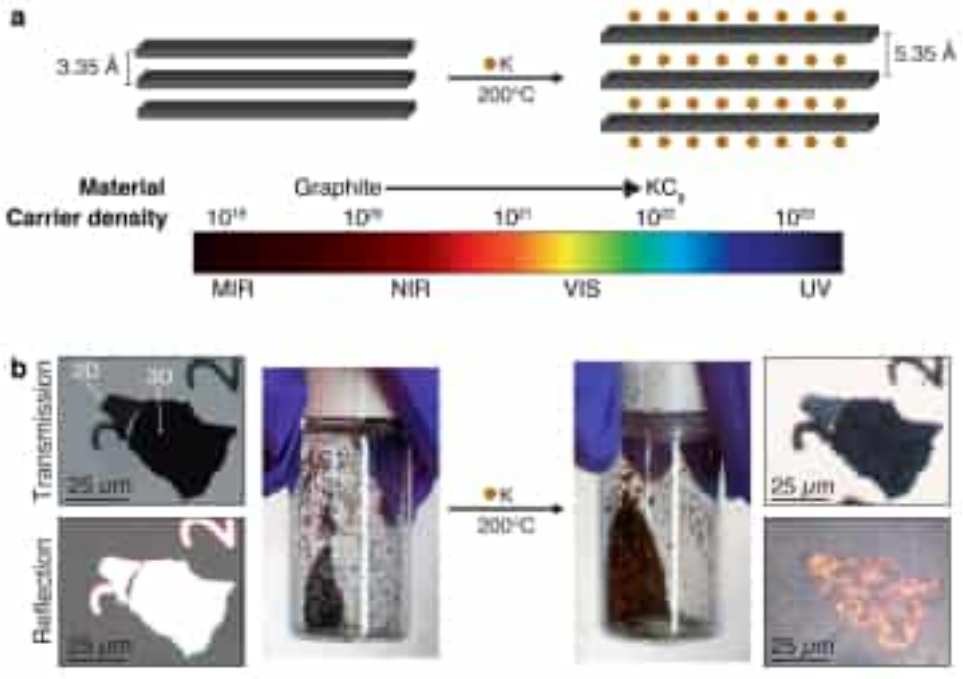


Figure 1.5: Intercalation is the insertion of a guest species into the interlayer void space of a layered structure. (a) As K inserts the interlayer space of FL graphite, the lattice expands. Moreover, the K donates electrons to the graphite host, causing the carrier concentration to radically increase. This change in concentration leads to the color change in the materials. (b) Graphite appears grey and reflective in bulk form, while bulk KC_8 is gold and reflective. As the material is thinned to the 2D realm, it can be seen that the highly reflective grey FL graphite becomes a highly reflective gold material. Moreover, the transmission increases with intercalation and the material is blue, due to the carrier concentration being related to a blue absorption.

1.2.2 Surface Composition

Due to the inherent structure of 2D and FL materials, surfaces (e.g. interactions and composition) play a more important role than in bulk. When a species adsorbs onto the surface of a 2D material and charge is transferred,[57,58] the extent of charge transferred can exceed that of electrochemical doping and the 2D material may become oxidized or reduced.[24,25] As the composition of the surface changes, the properties of the 2D material may be altered.[24] In order to better understand the role of the surface composition, here, FL and 2D BP are oxidized. Then, the surfaces of unoxidized and oxidized material were characterized and compared.

1.2.2.1 Oxidation of 2D Black Phosphorus

Although 2D BP exhibits desirable characteristics and potential to become an integral part of numerous devices, it is well-known that black phosphorus flakes undergo oxidation in ambient conditions[59–63], resulting in the degradation of its electronic properties. In spite of the subsequent degradation, appropriately controlled oxidation may transform the oxidation from a liability to a pathway for chemical functionalization—introducing properties in 2D black phosphorus similar to those found in graphene oxides.[12,64,65] As BP is oxidized, oxides form on the surface; BP, which is a semiconductor, is anticipated to transfer electrons to the oxidant and become a more p-type material. Here, water and/or oxygen are used as oxidants of 2D and FL BP. Then, by coupling transmission electron microscopy (TEM) images and X-ray photoemission spectroscopy (XPS) spectra of oxidized black phosphorus with density functional theory (DFT) computations of oxides, the spatial-distribution of the surface functional groups are resolved. Characterization of the oxidized material allows for insight into the role of oxygen and water in the oxidation process of FL and 2D BP, while also providing insight into the role of the surface on the composition on the properties of this 2D material.

METHODS

2.1 Bulk Material

Many bulk layered crystals are naturally-occurring, while some are synthetically-produced. For each, there are advantages and challenges that come with their use. For example, synthetic crystals can be of a high quality with low levels of contaminants. However, the synthesis of each layered material will require different conditions and equipment, which may not be accessible to all researchers. In contrast, naturally-occurring crystals generally have more defects and contaminants than synthetic ones, which will affect the resulting properties of the material. However, these materials are easier for many research groups to use because they can be readily purchased and do not require synthetic equipment. Therefore, in this dissertation, both synthetic and naturally-occurring crystals are described.

2.1.1 Synthesis by Chemical Vapor Transport

Chemical vapor transport (CVT) is a heterogenous synthetic method for the growth of crystals. Initially, the material(s) that is the component(s) of the crystal and additional precursors for the synthesis are placed on one end of a sealed growth chamber, referred to a the source zone. The chamber is heated, causing some species to enter a vapor phase. A temperature gradient is typically employed, allowing the added precursors to act as transport agents and facilitate the movement of the reactant to the cooler end of the chamber, referred to as the growth zone, where it undergoes deposition as a crystal.[66]

[1]Portions of this chapter reproduced from Kuntz, K. L.; Wells, R. A.; Hu, J.; Yang, T.; Dong, B.; Guo, H.; Woomer, A. H.; Druffel, D. L.; Alabanza, A.; Tománek, D.; Warren, S. C. Supporting Information: Control of Surface and Edge Oxidation on Phosphorene. *ACS Appl. Mater. Interfaces* **2017**, *9126-9135*. Copyright 2017 American Chemical Society.

[2]Portions of this chapter reproduced from Druffel, D. L.; Kuntz, K. L.; Woomer, A. H.; Alcorn, F. A.; Hu, J.; Donley, C. L.; Warren, S. C. Experimental Demonstration of an Electride as a 2D Material. *Journal of the American Chemical Society* **2016**, *16089-16094*. Copyright 2016 American Chemical Society.

2.1.1.1 BP CVT Synthesis

CVT was employed to produce bulk BP crystals by a method modified from Nilges[67] and used in literature.[23,24,26] First, a growth chamber was prepared using a quartz tube (inner diameter: 9.5 mm, outer diameter: 14 mm). It is important to note that this CVT occurs under high-pressure conditions, so the dimensions of the quartz tube are specifically selected to withstand pressures of ~ 40 atm.

After sealing one end of the tube with an oxyhydrogen torch, the quartz tube was loaded with red phosphorus (T_m: 590°C, 0.42 g, 99.9999%) and added precursors Sn (T_m: 232°C, 20 mg, 99.9999%) and SnI_4 (T_m: 144°C, 10 mg, prepared from SnI_2 and I_2) in a nitrogen-filled glovebox (O_2 <1.00 ppm, $H_2O <$ 0.10ppm). To ensure there is not material coating the sides of the ampoule that could impair a good seal of the growth ampoule, a glass pipette was used to transfer the solid material toward the sealed end of the tube (aka the source zone). Then, the open end of the tube was sealed with parafilm.

The quartz tube was removed from the glove box; the parafilm was removed and the tube was immediately placed under vacuum ($\sim 4 \cdot 10^{-3}$ mbar). After allowing the tube to reach the proper vacuum level (~ 2 hours), the open end of the growth chamber was sealed under vacuum using the oxyhydrogen torch at a length of ~ 10 cm. The sealed ampoule was placed into a furnace with at least 2 zones. The source end with solid material was placed in zone A and the growth end was placed in zone B with an insulating disc separating the zones. The sealed ampoule then underwent heating to allow the CVT growth of bulk BP.

<u>CVT conditions for BP</u>:

1. Zones A and B were heated to 500°C at a rate of 250°C per hour.
2. Zones A and B were heated to 600°C at a rate of 50°C per hour.
3. Zones A and B were held at 600°C for 4 hours.
4. Zone B was cooled to 550°C at a rate of 50°C per hour, while zone A was held at 600°C.
5. Zones A and B were cooled at a rate of 50°C per hour for one hour
6. Zones A and B were held at 550/500°C, respectively, for 2 hours.
7. Zones A and B were cooled to 25°C over 8 hours.

The cooled growth chamber was opened in the glove box. The BP crystals were contaminated by the transport agents, so the sample was refluxed in a Soxhlet extractor for 2 hours with anhydrous acetone under a N_2 atmosphere. The acetone changed from clear to yellow as the contaminants are washed from the bulk crystal. Under these growth conditions, the sample yield is $\sim 90\%$. For example, 500 mg of red phosphorus, 12 mg SnI_4, and 24 mg Sn yielded 459 mg BP. During the synthesis, some material may deposit on the quartz tube due to the temperature gradient, sometimes resulting in a tube that is colored from yellow to red to purple to black.

2.1.1.2 MoS_2 CVT Synthesis

MoS_2 is a polymorphic crystal, where the 1T phase is metallic and the 2H phase is semiconducting. As a semiconductor, hexagonal MoS_2 has a band gap that is thickness-dependent (Figure 1.2b,c) and therefore has many interesting properties when prepared as a 2D material. Here, 2H MoS_2 was produced by CVT, modified from other published methods.[68,69] The method of preparing and sealing an ampoule for the CVT, including the loading of material using a pipette, was similar to that of black phosphorus. However, it is important to note that this crystal is not an air-sensitive material and growth occurs at much lower pressures, using added precursors with low T_m.

After sealing one end of a long quartz tube (inner diameter: 9 mm, outer diameter: 15 mm), the sample was loaded with powdered MoS_2 (T_m: 1,185°C, ~6 μm with a maximum of 40 μm particle size), I_2 (T_m:113.7°C, T_b: 184.4°C, 99.99%), and S (T_m: 120°C, 99.998%) under ambient conditions. The sealed tubes were 20-25 cm in length with 125 mg/cm^3 of MoS_2, 5 mg/cm^3 of I_2, and $< 1\%$ by mass of S to prevent sulfur vacancies during crystal growth. Because of the low T_m of iodine, it will become a gas during the sealing of the tube due to heat from the oxyhydrogen torch. Additionally, because of the fine nature of the MoS_2 powder, there is a risk of it being pulled up the tube once the ampoule is placed under vacuum for sealing the second end. To prevent these materials from being lost or impairing the seal, a few approaches were used. First, the tube was sufficiently long such that the sealed end with the material could be placed in an ice bath prior to and during the tube-sealing process. Secondly, the MoS_2 was prevented from being dispersed along the tube when placed under vacuum. This was addressed by adding a quartz wool fiber in the tube near the source material to act as a barrier or reducing the rate at which the vacuum is pulled until a sufficient pressure ($\leq 10^{-3}$ Torr) is attained and then the rate can be increased before sealing the tube. However, another proposed approach for preventing the loss of material is pressing the precursor MoS_2

material in a pellet before loading it in the tube (Note, iodine should not be pressed into the pellet as it may react with metal in the pellet press.).

After allowing the tube to reach a vacuum level $\leq 10^{-3}$ Torr, the open end of the quartz tube was sealed under vacuum using the oxyhydrogen torch. The sealed ampoule was placed into a furnace with at least 2 zones. The source end was placed in zone A and the growth end in zone B with an insulating disc separating the zones. The sealed ampoule then was heated to allow the CVT growth of bulk MoS_2. It is important to note that the cooling rates for this method are slow, to provide sufficient time for nucleation and growth of the crystal.

CVT conditions for MoS_2:

1. Heated zones A and B to 1060°C at a rate of at 100°C per hour.
2. Held both zones at 1060°C for 24 hours.
3. Held zone A at 1060°C and cooled zone B to 1010°C over the course of 24 hours.
4. Held zone A at 1060°C and zone B at 1010°C for >24 hours (ideally, several days).
5. Cooled both zones to 25°C over 100 hours.

The cooled ampoule was opened, yielding a shiny semiconducting MoS_2 crystal, in contrast to the dull black precursor powder. It is important to note that the length of time allowed for for step 4 or step 5 is related to the yield of this CVT, with short times having lower yields. It is important to note that transport agents can dope the material.[68]. However, iodine can be mostly removed by an acetone wash. Crystal defects due to the loss of iodine can be minimized by annealing the sample under vacuum.

2.2 Exfoliation of Bulk Material

There are numerous top-down and bottom-up synthetic techniques that have emerged since the discovery of 2D materials. Top-down techniques, such as mechanical,[70] liquid,[26] and electrochemical[71] exfoliation are used in this dissertation. Top-down synthetic approaches facilitate the production of 2D materials in large quantities.[26] While bottom-up approaches are able to produce consistent thicknesses, production quantity is limited. Furthermore, bottom-up approaches can produce material with properties that are dependent on the exact synthetic conditions (e.g. the humidity and ambient lab temperature); these properties are therefore not

inherent to the material and may not be observable in other samples. Therefore, this work is limited in-scope to top-down approaches.

2.2.1 Mechanical Exfoliation

Mechanical exfoliation of bulk layered materials produces very high-quality 2D flakes. However, with the strengths of interlayer-interactions in the bulk material, intralayer bonds in a 2D sheet, and interfacial interactions between a material and an adhesive, mechanical exfoliation is a simple technique with highly interdependent parameters that vary with each layered material. After exploring many different tapes (e.g. Scotch Magic^{TM} tape, Scotch Transparent^{TM} tape, Nitto SPV 224PRM, Graphene Supermarket PDMS stamps, Graphene Supermarket PMMA thermal transfer tape) with a variety of layered materials, I developed two methods that I found to be widely generalizable to 2D materials (except materials that are oxidized by the hydroxyl -OH functional groups of the adhesive). Herein, these two techniques are referred to as the (i) monolayer (Figure 2.1a,d) or (ii) consistent-thickness method (Figure 2.1b,e).

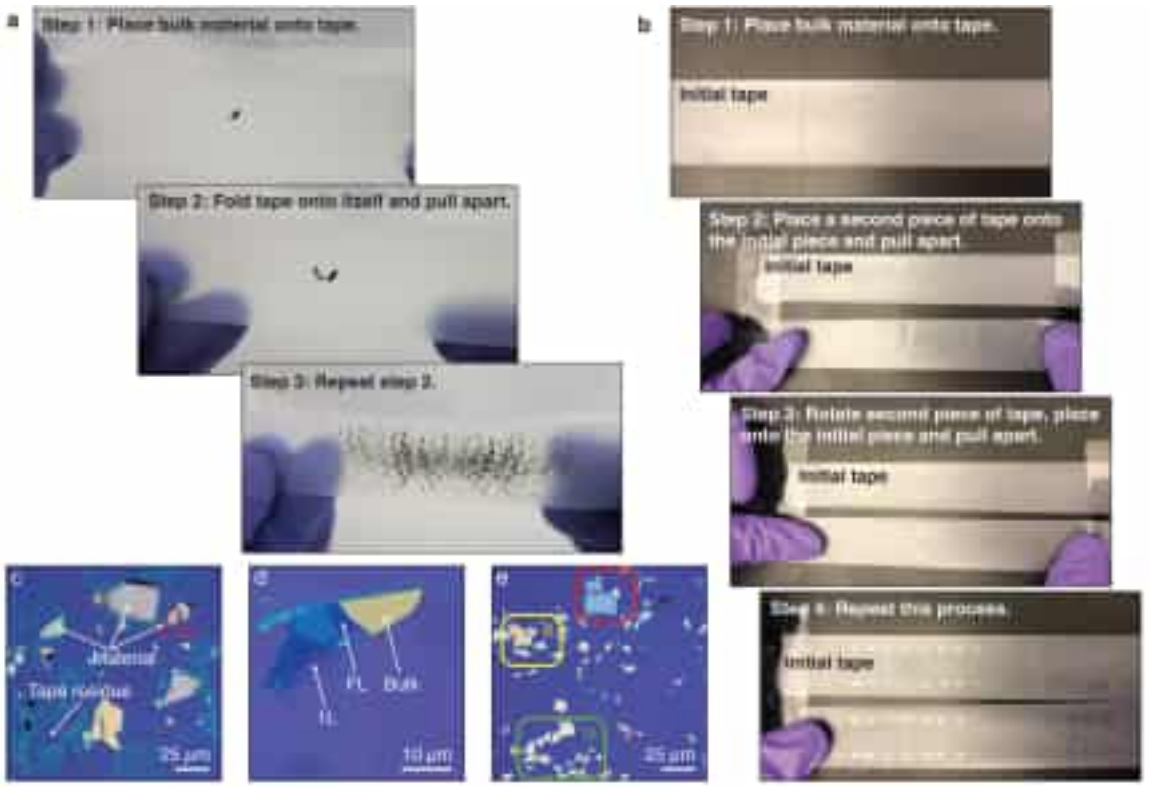


Figure 2.1: Two mechanical exfoliation methods are shown. (a) The *monolayer method* is the repeated exfoliation of a single bulk piece of material, mechanically cleaved by folding a single piece of tape onto itself repeatedly, as shown in steps 1–3. (b) The *consistent-thickness method* requires an initial piece of tape to be adhered to a hard surface with the adhesive side face-up. Then a single bulk flake is placed onto the tape (step 1). A second piece of tape is placed onto the initial tape and removed (step 2). The second piece of tape is rotated and placed onto the initial piece and then cleaved (step 3). This is repeated for the desired number of exfoliations (step 4). (c) To transfer the 2D and few-layer material to a substate, a cleaned substrate can be placed onto the tape and removed. The layered material will transfer and can be distinguished from debris and the amorphous tape residue by the angles θ of the edges of the flakes, which are dependent on the crystal structure. After washing off the tape residue, the flakes can be characterized where (d) the *monolayer method* produces material with single layers 1L and (e) the *consistent-thickness method* produces regions where the thickness is locally uniform. For example, region I is $\sim$ 70 nm thick, while regions II and III are thinner.

2.2.1.1 Monolayer Method

The monolayer method, demonstrated in Figure 2.1a, consistently produces 2D flakes with a thickness of a single layer 1L (Figure 2.1d). In this method, a single flake was placed on the center of a piece of Scotch Magic^{TM} tape. The tape was folded onto itself and unfolded, reducing the layered material thickness. This was repeated typically 8–15 times and the transition to 2D is accompanied by visual cues. For example, as

seen in Figure 2.1a, graphite changes from shiny to dull. Furthermore, it is important to note that the yield of monolayers depends on the material and environment. With the monolayer method, the typical yield is one sheet of graphene per square centimeter of tape when exfoliation is performed in ambient conditions; however, this is reduced to one per five square centimeters when performed under dry, inert atmospheres (e.g. in a N_2 glovebox).

2.2.1.2 Consistent-thickness Method

The consistent-thickness method yields FL flakes with locally similar thicknesses (Figure 2.1b,e). In this method, a piece of Scotch Magic^{TM} tape was placed adhesive side up and taped in place; this is referred to as the initial tape. Then a single flake was placed at the center of the length of the tape on the upper half (Figure 2.1b, step 1). For the first exfoliation, a second piece of tape was placed onto the first and removed, thereby reducing the material thickness by half. With this first exfoliation, there were two exfoliation spots–one on each piece of tape (Figure 2.1b step 2). After repeating the exfoliation, there will be 2^p exfoliation spots, where p is the number of exfoliations. It is important to note that material transfers best from the initial tape, but it can be transferred from secondary pieces.

While this method does not yield monolayers often, it does create FL flakes of similar thicknesses and it is possible to target specific thickness ranges. For example, I exfoliated natural MoS_2 by this method, targeting flakes between 20–25 nm. After characterizing the thicknesses for different exfoliations, I identified that 11 exfoliations yielded flakes predominately between 18–25 nm.

2.2.1.3 Transfer & Cleaning

After exfoliating the material, it is transferred from an adhesive to a substrate for study. While the extent of exfoliation (e.g. the thinness of a material that can be produced) depends interlayer and intralayer forces within the material, and interfacial interactions between a material and an adhesive, the transfer process introduces interfacial-interactions between the material and the substrate. In order for material to transfer from the adhesive to the substrate, the interfacial-interactions between the substrate and the material must be greater than other interfacial and/or interlayer interactions. In order to facilitate this, substrates are selected and prepared to facilitate adequate interactions with the material. For example, graphite adheres more strongly to hydrophilic surfaces than hydrophobic ones. Therefore, a SiO_2 surface that is freshly cleaned is better than a SiO_2 substrate that has hydrocarbons adsorbed to its surface. (Refer to Section 2.3.1 for more details.)

Once exfoliated material was transferred to a substrate, some tape residue also transferred (Figure 2.1c). To remove the residual tape, the sample was placed in a wash bath composed of 3:1 v:v acetone:toluene with stirring for 15 minutes. It is important to place the substrate near the stir bar such sufficient stir rates so the liquid is continually moving over the surface of the substrate. When removing the sample from the wash bath, while it was still wet, the substrate was rinsed with isopropyl alcohol (IPA) and then dried with N_2.

2.2.2 Liquid Exfoliation

Liquid exfoliation is a solution-processing route that allows for bulk layered material to be broken apart by mechanical means, such as tip-sonication, bath ultrasonication, or shear mixing. The resulting slurry is composed to a diverse set of laterally-sized sheets, as well as a broad range of thicknesses. These flakes can be separated based on their thickness and lateral dimensions through techniques such as centrifugation[26] or density gradient ultracentrifugation[16,72] to yield 2D and FL material.

During liquid exfoliation of layered materials, there are numerous interactions between the material and solvent that add complexity to this technique. For each material (e.g. BP, graphite, MoS_2), a solvent must be experimentally evaluated for its effectiveness of (i) facilitating the cleavage of a layered material to yield 2D and FL flakes, (ii) produce flakes of desirable lateral dimensions, and (iii) adequately suspending the exfoliated sheets such that sorting methods may be used to process the slurry.[26,73] After separating exfoliated material, the 2D and FL materials can be investigated in solution, drop-cast on substrates to study individual flakes (Section 2.3.3), or assembled into solid films (Section 2.3.2).

In this dissertation, liquid exfoliation is implemented with the following compounds:

- Graphite in IPA or N-methyl-2-pyrrolidone (NMP)
- MoS_2 in NMP
- BP in NMP
- Ca_2N in 1,3-dioxolane.

Because graphite and MoS_2 are not oxidized in ambient conditions, the liquid exfoliation of these materials was performed on the lab bench and in fume hoods. However, for air-sensitive materials like BP and Ca_2N, extra steps such as using anhydrous solvents and performing all handling under inert atmospheres were required. In this dissertation, only the exfoliation of BP is described in depth (Section 2.2.2.1).

2.2.2.1 Liquid Exfoliation of BP

To investigate the role of the surface composition, I prepared 2D and FL BP for oxidation studies. First, bulk BP crystals were synthesized by CVT (Section 2.1.1.1), refluxed with acetone to remove contaminants, and stored in a nitrogen glovebox ($O_2 \leq 1$ ppm, $H_2O \leq 0.1$ ppm). Under inert atmosphere, the BP was ground in a marble mortar and pestle. Note that due to static buildup within a glove box, the BP may become charged; an anti-static gun is useful to help alleviate the static discharge and loss of material. Then, the material was placed in scintillation vials with anhydrous, degassed NMP with a concentration of $\sim$0.5 mg/mL.[24,26] The vials were capped and sealed with parafilm and removed from the glove box for exfoliation in a bath sonicator. After sonication for 8 cycles of 99 minutes, the suspensions were transferred to Nalgene Oak Ridge FEP 50-ml centrifugation tubes in a glove box. The suspensions were centrifuged at 10,000 revolutions per minute (rpm) for 45 minutes using a Sorvall RC-5B super speed refrigerated centrifuge with a rotor radius of 14.56 cm. The resulting supernatant from the first centrifugation cycle was collected and centrifuged a second time under identical conditions. Due to the high boiling point and low volatility of NMP (T_b: 202°C), it is not easy to process and use BP in this solvent. Therefore, the resulting 2D material is transferred into a more volatile solvent with a lowering boiling point. To transfer the 2D and FL material to IPA (T_b: 82°C), $\sim$10% of the supernatant was removed and IPA was added. The suspension was mixed and centrifuged at 20,000 rpm for 60 minutes. Then $\sim$50% of the supernatant is removed and replaced with IPA. The suspension was mixed and centrifuged again at 20,000 rpm for 60 minutes. Finally, the supernatant was removed and the sediment of 2D material was re-dispersed in IPA. The resulting slurry of 2D and FL material was characterized TEM, determining that the flakes were 1–7 layers (Section 2.5.2.1).

2.2.3 Electrochemical Exfoliation

Another route to produce 2D material is electrochemical exfoliation. This method first requires the insertion of a guest species in the interlayer space. This intercalation is typically associated with a lattice expansion. With sufficient lattice expansion and reduced vdW interactions in the resulting intercalation compound, the layers may be cleaved and produce 2D or FL materials.[7,38,71]

Since electrochemical exfoliation of layered materials may be a desirable or undesirable outcome of intercalation depending on the research application of the material, the parameters that govern the exfoliation must be experimentally determined to be able to incite or prevent the cleavage of the material. For example,

during the intercalation of graphite with HSO_4^-/H_2SO_4, the lattice expands from 0.335 nm to 0.8 nm.[74,75] During the study of this graphite intercalation compound (GIC) in 10 M sulfuric acid or 1 M $(NH_4)_2SO_4$[76] for optoelectronic applications, exfoliation is an undesired result. Therefore, in the 1 M $(NH_4)_2SO_4$ electrolyte, graphite was placed at the anode and platinum at the cathode. The current was systematically increased until the potential reached $\sim$1 V.[71] This caused vigorous bubbling at the graphite as the material oxidized at the edges, the guest species intercalated, and then the lattice was exfoliated. With this insight, during future experiments, experiments were performed using lower current to prevent delamination of the layers.[76]

2.3 2D Flakes

After the exfoliation of bulk layered crystals, the resulting material was characterized. Aggregate behavior emerging from the polydisperse material was observed in solution or thin films. Furthermore, individual flakes and quantum-confined properties that emerge from the nanoscale dimensions, were also investigated. In this section, the preparation of the substrate and the assembly of solid-state films are discussed.

2.3.1 Substrate Preparation

In order to characterize the material, we transferred individual flakes or slurry to a substrate. With the ultra-thin dimensions of these materials, the substrate can play a critical role in the resulting properties of the material.[25,77] Additionally, the interfacial-interactions between the flakes and substrate and the type of substrate determine the characterization techniques and applications. Selecting the appropriate substrate for each material and each study is of great importance, as well as the cleanliness of the substrate surface.

Since the interfacial-interactions between the substrate and the 2D material determine whether the material will adhere and remain adhered during all further processing and handling, it is crucial to properly prepare the substrate surface. Every substrate is first rinsed in electronic grade acetone and then IPA twice and then dried with N_2.

For 2D materials that are in hydrophilic solvents or are hydrophilic, the surface of the substrate needed adsorbed hydrocarbons, which are hydrophobic, to be removed. Hydrocarbons were be removed from substrates by (1) UV-ozone treatment at 150°C for 300 seconds, (2) pirahna cleaning (3:1 v:v H_2SO_4:H_2O_2 for 30–60 minutes, then rinsed and stored in water), or (3) aqua regia. To verify that a surface is hydrophilic, water can be dropped on the surface and it will uniformly spread across the surface. Additionally, it

is important to note that after a cleaned substrate is exposed to ambient conditions for $\sim$ 10 minutes, hydrocarbons readsorb to the surface. These methods of removing hydrocarbons are readily compatible with silicon oxide surfaces (e.g. glass, quartz), however, there are some limitations. Some examples include (1) atomically-smooth surfaces such as silicon oxide wafers should not be exposed to pirahna solution or aqua regia, as these corrosive solutions may cause substrate roughening, (2) metallic substrates should not be cleaned in aqua regia since this solution removes metals, and (3) copper should not be cleaned by UV-ozone treatment as it simply causes oxidation of the metal surface.

Some substrates cannot be cleaned by these methods, such as highly-doped silicon wafers that lack an oxide layer. To clean substrates such as these, the substrate was sonicated in acetone or IPA in the bath sonicator to help remove hydrocarbons. However, without a more rigorous cleaning method, interfacial-interactions were weaker and material did not remain adhered to the surface during more vigorous processing or handling.

In addition to substrate cleaning, substrate selection played a crucial role in characterizing 2D materials. For example, some techniques such as UPS require good electrical contact between a sample, substrate, and the instrument. Therefore, a conductive substrate that has good interfacial interactions and electrical contact with the 2D material is essential. Some examples of conductive substrates used in these experiments include metal-plated silicon oxide wafers (e.g. 5 nm Ti/Cr and 100 nm Au or 5 nm Ti/Cr and 100 nm Pt) or highly-doped semiconductors (e.g. Nb-doped tin oxide (NTO), p-doped silicon wafer with 0.001–0.005 $\Omega \cdot$ cm resistivity). For each characterization method, it was important to select the substrate that was most appropriate for the experiment.

2.3.1.1 Marker Pattern Microfabrication

Patterns were made on substrate to help with repeatedly locating the same flake in various instruments at various stages within an experiment. These positive patterns were microfabricated by two methods: electron-beam lithography (EBL) or photolithography. As depicted in Figure 2.2, EBL produces smaller patterns with a higher resolution than than photolithography, but photolithography is a faster method for patterning larger areas (i.e. a microscope slide or 5 inch silicon wafer).

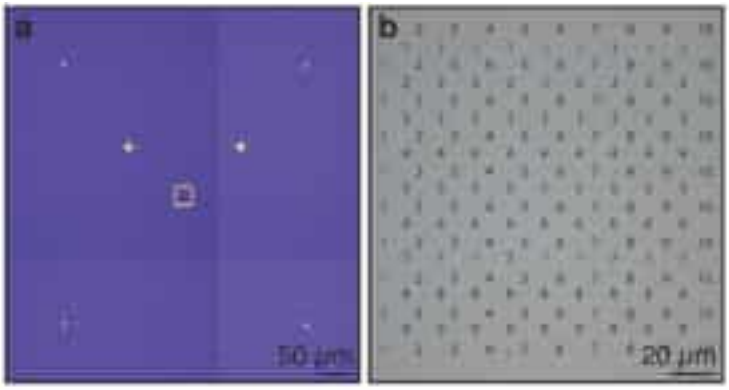


Figure 2.2: Gold marker patterns fabricated by (a) EBL on silicon wafer with 285 nm silicon oxide and (b) photolithography on a glass microscope slide.

To create a positive resist for EBL, 2 layers of MMA and one layer of PMMA (Microchem MMA EL9 and PMMA A2) were spin-coated onto the substrate, typically Si/SiO_2 wafers, using a spin coater (Laurell Technologies Model WS-650-23B). For the spin-coating, each layer was spun at 4000 rpm for 30 seconds and then dried on a hotplate at 180°C for 60 seconds. A pattern was made using a Nanometer Pattern Generation System on a Helios 600 instrument at an accelerating voltage of 30 kV, beam current at 340 pA to 11 nA, and an e-beam dosage of 350 μC/cm^2 at a 100X magnification. Then, the patterned resist was developed in 1:3 methyl isobul isobutyl ketone (MicroChem MIBK):IPA for 60 seconds and then rinsed with IPA. Metal was then deposited by either e-beam evaporation (Thermionics VE-100, $\leq 3 \cdot 10^{-8}$ Torr) or sputter evaporation (Kurt Lesker ® 75, $\leq 5 \cdot 10^{-5}$ Torr). Deposition first involved < 5 nm of a metal that adhered well to the SiO_2 surface, such as Cr or Ti and then, 50 or 100 nm of the desired metal (typically Au or Pt). Finally, the substrate is sonicated in acetone to lift off the undeveloped resist, rinsed in IPA, and dried with N_2. A sample of an entire pattern is shown in Figure 2.2a.

To create a positive resist for photolithography, the substrate was first prepared by spin coating the photoresist (Microchem MCC Primer 80/20) at 3000 rpm for 20 seconds. Then the substrate was baked at 115°C for 1 minute. After baking, S1805 positive resist was deposited onto the substrate at 3000 rpm for 20 seconds. Then, the substrate was baked again at 115°C for < 2 minutes. The sample was loaded into a Karl Suss MA6/BA6 Mask Aligner with a 350W mercury lamp with the i-line 365nm wavelength at 12.0 mW/cm^2 and h-line 405nm wavelength at 23.5 mW/cm^{2}in hard-contact mode with a mask. A reflective substrate (e.g. Si wafer) was exposed for 7 seconds, while a transparent substrate (e.g. glass microscope slide, quartz) was exposed for 9 seconds. The patterned substrate underwent metal deposition, most often by sputter evaporation

(Kurt Lesker ® 75, $\leq 5 \cdot 10^{-5}$ Torr). The deposition method and lift-off method are the same as with EBL. A small subset of the patterned grids covering an entire glass microscope slide is shown in Figure 2.2b.

2.3.2 Doctor Blade Technique

Re-concentrated suspensions of 2D material in a volatile solvent (e.g. BP in isopropanol, Figure 2.3a,b) were used to create thin films (Figure 2.3c,d) of the material by the doctor blade technique. The substrate is immobilized, by adhering it to a surface. In this dissertation, Scotch Transparent^{TM} tape was used to tape two opposite edges of the wafer to a stable surface, each covering the edge of the substrate by approximately 1-2 mm. Then, 3 µL aliquots of the 2D suspension were placed on the surface of the $\sim$ 1 cm^2 substrate near an edge (not adjacent to the tape). A hydrophilic glass microscope slide was slid across the surface, spreading the 2D material across the substrate. This was repeated up to $\sim$400 times (Figure 2.3c,d); it became apparent that the 2D suspension was sufficiently concentrated if a visible color change of the substrate occured at $\sim$30 swipes.

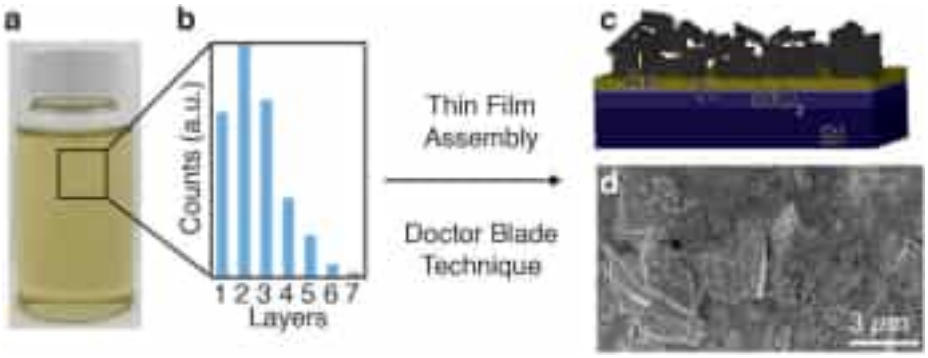


Figure 2.3: Thin film assembly doctor blading. (a) A concentrated suspension of 2D material in a solvent, with (b) the thicknesses shown, is used to (c) assemble a thin film on top of a gold plated substrate. (d) An SEM image shows the top-down view of the resulting film.

2.3.3 Drop-casting

Drop-casting samples of 2D material allows for flakes to be placed on many substrates such as TEM grids. In the preparation of samples for TEM studies, 6 µL aliquots of 2D materials in a lower T_b or volatile solvent were drop-cast onto a TEM grid. More specifically, in the study of the oxidation of 2D and FL BP, BP in IPA was drop-cast onto 300–mesh copper TEM grids with a lacey carbon film (Ted Pella) in the glovebox and allowed to dry for a minimum of 45 minutes. However, for other solvents with a lower T_b, heating of

the sample was sometimes necessary to facilitate the removal of the solvent. It is important to note that drop-casting does not lead to a uniform-distribution of material due to the coffee-ring effect (i.e. there is a higher concentration of the material the edges of the drop due to capillary flow during evaporation).

2.3.4 Sealed Inert Environments

Many 2D materials are sensitive to environmental conditions, resulting in reactivity or degradation of material in O_2, H_2O, and even N_2. Therefore, it is important to handle and characterize samples in an appropriate environment. To address this, I developed numerous methods to seal different samples under appropriate conditions, with generalize schematics shown in Figure 2.4, with the versatility to be characterized by optical or electrochemical methods.

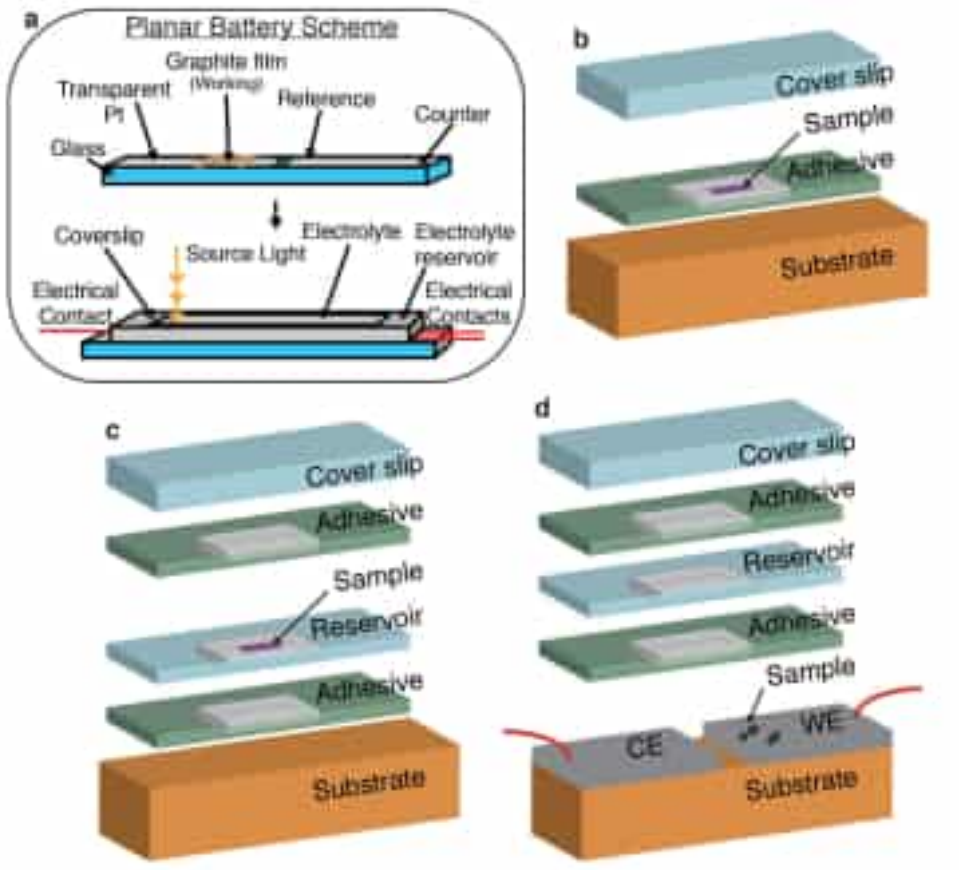


Figure 2.4: Sealed samples under inert atmospheres for characterization. (a) A planar battery scheme for *in situ* optical and electrochemical measurements is shown. Variations on this setup for (b) samples placed directly on a substrate, (c) samples on a secondary substrate being encapsulated within a reservoir which provides space between the substrate and coverslip, and (d) a sample in contact with metal-plated substrate for conductive measurements.

In these setups, a larger area substrate was first selected. While this was often a transparent glass or quartz microscope slide, a number of substrates such as silicon wafers, metal slabs, and metal-plated substrates were used. The substrate was selected for the appropriate experiment (e.g. glass for visible transmission measurements, double sided polished silicon wafers for FTIR, or metal-plated glass slides for electrochemical experiments). After selecting a substrate, a sample was placed directly onto the substrate and then sealed with an adhesive and transparent coverslip (Figure 2.4a). However, if a sample was already adhered to a secondary substrate, the sample was sealed under inert atmosphere with a glass microscope slide with a sand-blasted hole in the center, which served as a reservoir and/or spacer between the substrate and coverslip (Figure 2.4b). Interestingly, the reservoir can be sealed under gaseous or aqueous conditions. Finally, the entire setup was modified for electrochemical measurements by depositing metal or highly-conductive electrodes (e-beam or sputter deposition of Pt, Au, Al, Ag, ITO), filling the reservoir with an electrolyte and sample, and finally adhering wires to the conductive substrate (Figure 2.4a,d).

2.3.4.1 Epoxy Selection

The adhesive sealing a 2D sample under inert environment is extremely important. Many epoxies outgas water, oxygen, or alcohol byproducts during curing. Additionally, some adhesives and epoxies require specific temperatures to cure. Since many materials are sensitive to oxidation and/or degradation by these species and degrade at certain temperatures, each epoxy was selected such that it would not have undesired interactions with each sample it was used to seal. Furthermore, for samples sealed in solutions, the adhesive was tested to ensure compatibility with the solvent and any solutes under the experimental conditions (e.g. during heating or electrochemical measurements).

Several adhesives were identified and used for sealing 2D samples in specific environments in this dissertation. These preferred adhesives are:

- Loctite® Hysol® 1C
- Loctite® Hysol® EA 9340
- Loctite® Hysol® Stycast ES 1901
- Solaronix Meltonix 1170-60.

Loctite® Hysol® 1C is an off-white, two-part epoxy that cures at room temperature over 36 hours. During curing, this adhesive outgasses alcohol. Additionally, this epoxy is compatible with vacuum conditions, so it can be used on samples what will be placed under vacuum. Loctite® Hysol® EA 9340 is a green, two-part epoxy that cures at room temperature over 24 hours or at 60°C in 2 hours. This adhesive has minor outgassing. Interestingly, this epoxy has great chemical-resistance; it was chemically-inert with all electrochemical setups tested, including concentrated acids and halogenated electrolytes. The third epoxy typically used was Loctite® Hysol® Stycast ES 1901. This epoxy was harder to work with, because it is a two-part mixture that requires the use of a dispensing cartridge and two-part mixer nozzle and cures at room temperature in one hour. Interestingly, this epoxy did not outgas water or alcohols, so it is compatible for sealing samples such as Ca_2N under Ar atmospheres. An alternative to epoxies are heat-sensitive polymers. Here, Solaronix Meltonix 1170-60 was often used. This polymer adheres well to SiO_2 substrates when raised to a temperature of ~ 110°C for < 60 seconds. To ensure a good seal was achieved, a uniform pressure was applied to the setup during heating, rubbing the setup to remove any bubbles, ultimately yielding a transparent seal. With a good seal, any of these adhesives maintained a sealed environment when exposed to ambient conditions for weeks to months, enabling the characterization of samples at numerous instruments and at different points in an experiment.

2.4 Oxidation of 2D Black Phosphorus

Thin films of 2D assemblies (Section 2.3.2) or TEM grids with flakes of 2D BP (Section 2.3.3) underwent the same exposure procedures. A sample was placed in an air-tight glass tube inside the glovebox and wrapped in aluminum foil. Then, I removed the sample from the glovebox. The glass tube, shown in Figure 2.5b, was specifically designed for this study; it is equipped with an air-tight screw cap and a Teflon-sealing valve adjacent to a hose connection. For each oxidation environment, the sample was exposed in the dark to a flow of the oxidant gas(es) by opening the Teflon valve and screw cap for 5 minutes. The screw cap is then closed, followed immediately by the Teflon valve. The aluminum foil is removed and the sample is illuminated with a 460 nm LED with a specific power of 0.6 mW/cm^2 for 1, 6, or 18 hours. The 460 nm light source is selected to ensure all material—monolayers to bulk—was photo-excited during oxidation.[26] At the end of the exposure, thin film samples were brought into the glovebox with a minor opening in the Teflon

valve to evacuate the oxidants. For flakes on TEM grids, N_2 was used to purge the glass tube, then it was sealed and taken into the glovebox.

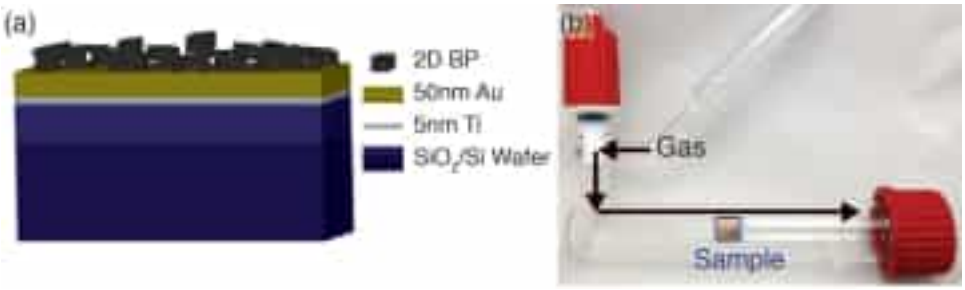


Figure 2.5: Oxidation of thin films of 2D black phosphorus. (a) Thin film of 2D black phosphorus assembled on a conductive, metal-plated thermal oxide silicon wafer. (b) Basic setup for oxidant exposure of 2D black phosphorus samples, showing the glass tube with an air-tight screwcap and a Teflon valve adjacent to a hose connection. The arrows indicate the direction of oxidant gas flow.

To create the O_2 environment, P_2O_5 desiccant ($\sim$ 0.2 g) was placed upstream of the sample, ensuring the environment was devoid of H_2O before reaching the sample. Then, research grade O_2 (99.999%) was flowed over the desiccant and the sample. To create the H_2O/N_2 environment, N_2 gas was bubbled through distilled water for 30-60 minutes and heated to 100°C. The H_2O vapor with N_2 as a carrier gas were used in the sample exposure. To create a H_2O/O_2 environment, O_2 was bubbled through distilled water for 30-60 minutes and heated to 100°C. Then, the sample was exposed to H_2O vapor with O_2 as a carrier gas. For ambient exposures, the samples were exposed to ambient conditions (ca. 50% humidity) for 5 minutes and then sealed.

2.5 2D Flake Characterization

To study the effects of dimensions, composition, and the interlayer space, many techniques were needed to visualize and characterize these ultra-thin materials and their surface, composition, and carrier concentration. Optical microscopy, atomic force microscopy (AFM) and TEM provide quantitative information regarding material dimensions and can provide qualitative insights when coupled with other techniques. X-ray photoemission spectroscopy (XPS) and ultraviolet photoemission spectroscopy (UPS) are surface sensitive techniques that provide insight into the surface composition. When these are coupled with other techniques, such as Raman spectroscopy and DFT, more information about composition and interlayer interactions can be

deduced. The application of these techniques to spatially-resolve compositional data of 2D and FL materials is discussed here.

2.5.1 Optical Microscopy Images

In this dissertation, optical microscopy images were collected using Nikon Eclipse E600 with a Nikon DS-Fi2 color camera. Objectives included a Nikon TU Plan Fluoro with magnifications of 100X (NA: 0.90, WD: 1.0 mm) as well as a Nikon T Plan Super Long Working Distance (SLWD) 50X objective (NA: 0.40, WD: 22 mm).

2.5.1.1 Bright-field and Dark-field Microscopy

Bright-field (BFM) and dark-field (DFM) microscopy images were obtained; these images assist with visualing lateral and thickness dimensions, as well as deducing qualitative observations. Due to the different optical paths by which BFM and DFM images were collected, these techniques can be used to distinguish 2D and FL flakes from amorphous material, debris, or other contaminants. For example, Figure 2.6 shows exfoliated MoS_2. In the BFM image collected in transmission mode (Figure 2.6a), there is an area that appears nearly transparent. Due to the fact that 2H MoS_2 is a hexagonal lattice (Figure 1.2b), exfoliated material is expected to have angles that are multiples of 60° (Figure 2.1c) or multiples of 30° when the 2D flake is cleaved at defect sites. Therefore, the angles of the edges are an indicator that the transparent material might be a 2D MoS_2 sheet. In order to optically investigate this further, the material is imaged in BFM reflection mode (Figure 2.6b). In this image, the same area appears less reflective than other MoS_2, which is expected for thinner material. This further indicates that the sample may be a 2D sheet. Finally, the material is imaged in DFM. In dark-field, scattered photons lead to bright areas in the image. For 2D and FL materials, the edges scatter photons while a flat surface does not scatter light. Therefore, the edges of the 2D and FL material were apparent Figure 2.6c, confirming that the thin sheet observed in Figure 2.6a,b was a 2D sheet and not contamination. Through atomic force microscopy (AFM), this thin material is confirmed to be a monolayer of MoS_2.

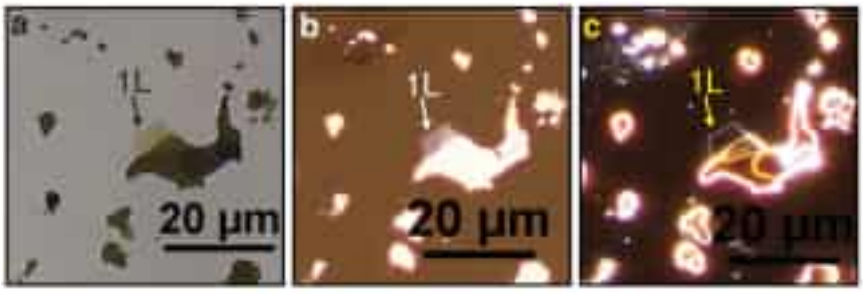


Figure 2.6: Mechanically-exfoliated MoS_2 in (a) BFM transmission, (b) BFM reflection, and (c) DFM reflection with a monolayer identified.

2.5.1.2 Lateral Dimensions

For an optical microscope, the spatial resolution R of lateral sizes that can be accurately observed and measured is determined by the incident light wavelength λ and the NA of the microscope objective, according to Equation 2.1. For example, a white light source, which emits more green photons with an approximate wavelength of 550 nm, with a 50X objective and NA of 0.40 has a theoretical spatial resolution of 839 nm. By using a 100X objective with a NA of 0.90, the spatial resolution can be improved to 373 nm. Therefore, in our microscopy images, lateral dimensions can be resolved for samples larger than R.

$$R = \frac{0.61\lambda}{\text{NA}} \tag{2.1}$$

2.5.2 TEM

A JEOL 100CX II TEM with an accelerating voltage of 60, 80, or 100 kV and a resolution of 2 Å (lattice) and 3 Å (point to point) was used to characterize 2D flakes. The contrast of the 2D material relative to the background is used to determine thickness of FL material; with each additional layer, the contrast changes by an integer value.[26] For example, with the conditions described in Ref. 24, the contrast increases by 25 with each additional BP layer. Moreover, selected area diffraction pattern enables insight into the crystallinity of a material.

2.5.2.1 TEM: Black Phosphorus Oxides

After preparing TEM grids by drop-casting (Section 2.3.3), each grid was sealed and transported in polypropylene bags, then loaded and unloaded at the TEM under N_2 in dim light conditions. After

characterizing unoxidized flakes, samples underwent oxidant exposure. After 1, 6, and 18 hours of exposure, the samples were purged with N_2, and then stored in the glovebox for TEM imaging. At each time interval, all previous flakes were re-imaged to provide information about physical degradation. Additionally, two new flakes were imaged at each time step. Imaging new flakes allowed for physical changes to be observed and for the possibility of knock-on damage to be addressed. Previously imaged flakes did not show any distinguishable differences from flakes characterized at later time steps indicating that knock–on damage did not significantly contribute to the observed physical changes of flakes, in agreement with previous work using the same accelerating voltage.[59]

2.5.2.2 TEM Image Processing

Images were acquired and further processed using Gatan Digital Micrograph. Due to inherent noise present imaging process and the specific 2K X 2K Gatan CCD camera used, a background subtraction was performed post-imaging to reduce the camera detector noise in the image. This image processing technique is demonstrated in Figure 2.7. For each image of a flake, a minimum of two additional images were collected at the same condenser settings with higher magnifications in an area adjacent to the flake, without any portion of the TEM grid present. These higher magnification images were then averaged—herein referred to as the background image—to obtain a representation of the noise inherent to the image acquisition process. Finally, the background image was subtracted from the original image to reduce the detector noise. In each of the images in Figure 2.7, an increased presence of white pixels is evident on the right side of each of the images, implying the noise is inherent to the image acquisition process. An image of a flake was acquired at 72X magnification at an accelerating voltage of 80 kV (Figure 2.7a). Twelve additional images adjacent to the flake were taken at 100X (Figure 2.7b) and 140X at the same condenser setting. The average of these higher magnification images is shown in Figure 2.7c. Finally, the average background is subtracted from the original image, depicted in Figure 2.7d. The images shown in Figure 2.7a,d are at the same brightness, contrast, and gamma values in Gatan Digital Micrograph; the standard deviation in the Figure 2.7a is reduced from 72.68 to 58.32 in Figure 2.7d.

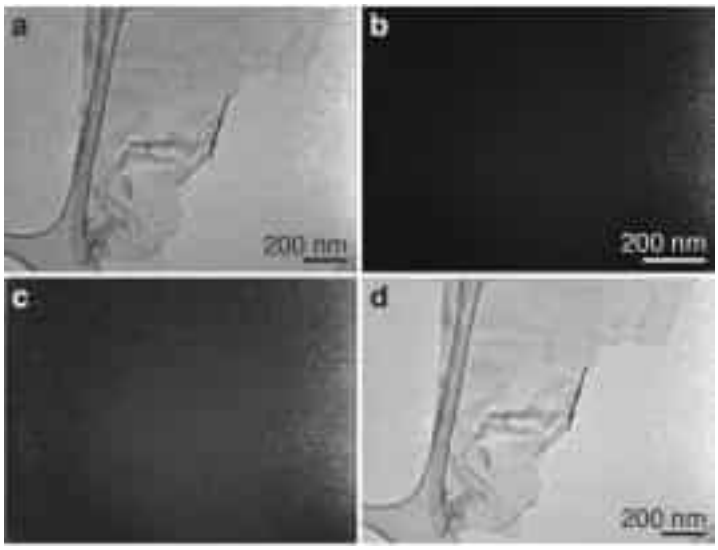


Figure 2.7: Processing of TEM images to reduce camera noise. (a) Image of a 2D BP flake acquired at 72X magnification at an accelerating voltage of 80 kV. (b) To visualize the pixel noise resulting from the TEM instrument and CCD camera, a 100X image was acquired adjacent to the flake at the same condenser settings. (c) The average background image is an average of the images collected adjacent to the flake at 100X and 140X magnifications. (d) The processed TEM image of a 2D BP flake after the average background image (c) was subtracted from the original image (a).

2.5.2.3 Diffraction: Black Phosphorus Oxides

During the time-lapsed TEM study of individual flakes of 2D BP with exposure to oxidants for up to 18 hours, a selected area diffraction pattern of each flake was acquired at each time interval. The orthorhombic crystal structure of 2D BP is observed after exposure to oxidants O_2 (Figure 2.8a), H_2O/N_2 (Figure 2.8b), and ambient conditions of H_2O and O_2 (Figure 2.8c) for 18 hours. This further verifies that not all 2D BP is oxidized.

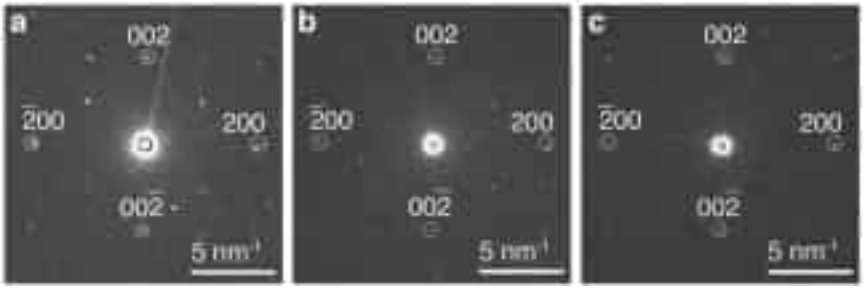


Figure 2.8: Diffraction patterns of 2D BP after 18 hours of oxidant exposure: (a) O_2 (99.999%), (b) H_2O/N_2 (99.998%), and (c) ambient conditions (humidity ca. 50%).

2.5.3 XPS & UPS

Due to the thinness of 2D materials, surface characterization techniques are very useful in the study of these materials. XPS and UPS probe the surface of a material with depths up to 10 nm and 3 nm, respectively. In these techniques, photons interact with core and valence electrons, respectively, thereby providing information about the local surface environment and material. In this dissertation, samples were studied using a Kratos Axis Ultra Delay-Line Detector (DLD) spectrometer under high vacuum ($< 10^{-9}$ Torr) with a monochromatic Al Kα X-ray source (1486.6 eV) and a He I source (21.2 eV) for XPS and UPS measurements, respectively. Air-sensitive samples were loaded under dry N_2 conditions.

2.5.3.1 Introduction to XPS

An incident X-ray photon $h\nu$ causes the ejection of an electron with a kinetic energy E_K through a process known as photoemission, shown in Fig. 2.9. The core electron binding energy E_B^F of the atom is calculated according to $E_K = h\nu - E_B^F$. Variations in local chemical environments cause the core electron binding energy to shift, thereby allowing for local composition to be probed with XPS.

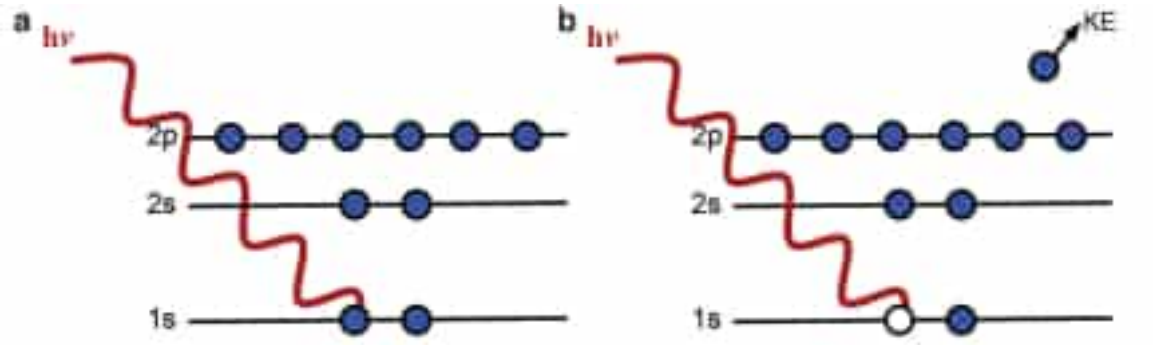


Figure 2.9: Photoemission of core electron: An incident X-ray with energy $h\nu$ (a) collides with a core electron, with binding energy E_B^F, which is then (b) ejected with kinetic energy E_K.

2.5.3.2 Quantification of Composition

In XPS spectra, the peak position is related to the atom and its local chemical environment while the area of the peak is related to the atomic composition. By changing the oxidation state, the binding energy of core electrons are altered and peak positions will shift to higher binding energies. For example, as the BP surface becomes functionalized with electron-withdrawing moieties, the phosphorus 2p core electrons are expected to experience higher valued binding energies, due to the reduced screening of the nuclear charge.

Using the principle n, angular momentum l, and spin angular momentum s quantum numbers, each core electron binding energy is described using nlj, where $j = l \pm s$. For example, a 3d orbital has an $l = 2$, so the core electron binding energies will be written as $3d_{5/2}$ and $3d_{3/2}$. For an s orbital, $l = 0$ and therefore $j = 1/2$. Since there is only one j value, each s orbital has a single binding energy and therefore, a single peak in XPS. However, for a p orbital $l = 1$ and therefore $j = 1/2$ or $3/2$. This results two binding energies, which is a doublet in the spectra. The doublet is a result of spin-orbit coupling and the area of each peak is related to the number of electrons that are degenerate in these spin states. For example, for the six 2p core electrons, there two electrons in each of the $2p_x$, $2p_y$, and $2p_z$ orbitals. The $2p_x$ and $2p_y$ orbitals have degenerate j values of $3/2$, while the $2p_z$ orbital has a j value of $1/2$. This results in an area ratio of 2:1 for the $2p_{3/2}$ and $2p_{1/2}$ peaks in the 2p doublet. For d and f orbitals, the area ratios are 3:2 and 4:3 for the doublets, respectively. Furthermore, the spin-orbit splitting Δ between the doublet peaks is related to the strength of the spin-orbit coupling and is therefore unique to each element. Unlike the binding energy of core electrons, Δ values do not usually change with local composition.

To qualitatively interpret XPS spectra, after performing a Shirley background, each core electron peak was fit with a Voigt function, which is a convolution of Gaussian and Lorentz components. For p, d, and f doublets, the relative area of each peak was fixed to the appropriate area ratio and the peaks were set with a spacing of Δ. When there is more than one oxidation state present, there may be more than one singlet (s orbitals) or doublet (p, d, f orbitals) present. For these cases, more singlets and doublets were added with the same constraints until the cumulative fit of all oxidation states better approximated the raw data. It is important to note that it is possible to overfit the data and that the cumulative fit is only a local fit and not a global fit. Therefore, XPS can provide significant insight only into the relative compositions of oxidation states.

2.5.3.3 Composition of 2D Material Surfaces by XPS

Because of the information about binding energy of core electrons, XPS was used to gain insight into the chemical environment of the surface composition of 2D materials and their oxides, such as Ca_2N and BP.

For Ca_2N, the calcium 2p core electron spectra (Figure 2.10a, Table 2.1) of 2D Ca_2N have a Ca 2p doublet with a spin–orbit splitting $\Delta = 3.5$ eV. The Ca $2p_{3/2}$ peak was centered at 347.5 ± 0.2 eV (Table 2.1) with a FWHM of 1.9 eV. In addition, the Ca 2p spectra showed plasmon loss peaks shifted by 7.9 and 11.4 eV relative to the Ca $2p_{3/2}$ center. Plasmons loss peaks are characteristic of metallic species in XPS. These

values are in agreement with our 3D Ca_2N (Table 2.1) and with previous literature.[78] After the measurement, the 2D Ca_2N samples were exposed to ambient conditions, which caused oxidation and a corresponding color change from black to white. The XPS spectra of these deliberately oxidized samples match that of $Ca(OH)_2$ (Figure 2.10a, Table 2.1). We concluded that the surface of our as-synthesized 2D Ca_2N has not oxidized to $Ca(OH)_2$.

Table 2.1: XPS binding energies (eV) of Ca 2p electrons from Ca_2N & oxides

Material	$2p_{3/2}$	$2p_{1/2}$	plasmon A	plasmon B
Ca_2N	347.5	351.0	355.4	358.9
3D Ca_2N	347.5	351.0	355.5	359.0
Ca_3N_2	346.2	349.7	354.3	358.0
$Ca(OH)_2$	346.7	350.3	354.8	358.3
2D Ca_2N ox.	346.6	350.2	354.7	358.3

Additionally, we examined the nitrogen 1s core electron binding energy (Figure 2.10b). We attributed the singlet peak, centered at 399.2 ± 0.1 eV with a FWHM of 2.2 eV, to the N 1s core electrons in 2D Ca_2N, in agreement with our 3D Ca_2N (399.3 ± 0.1 eV). We noted the N 1s peak is positioned at a different binding energy than previously reported, but we could not compare absolute positions because a carbon reference was not provided.[78] By comparing the area of the peaks of the Ca 2p core electrons to N 1s core electrons and accounting for the atomic sensitivity factors, we measured the ratio of Ca:N for 2D Ca_2N (5.3:1), Ca_3N_2 (4.6:1), and oxidized Ca_2N (18:1). We found that the ratio was significantly calcium-rich in all measurements and the intensity of the nitrogen peak was low in all samples.

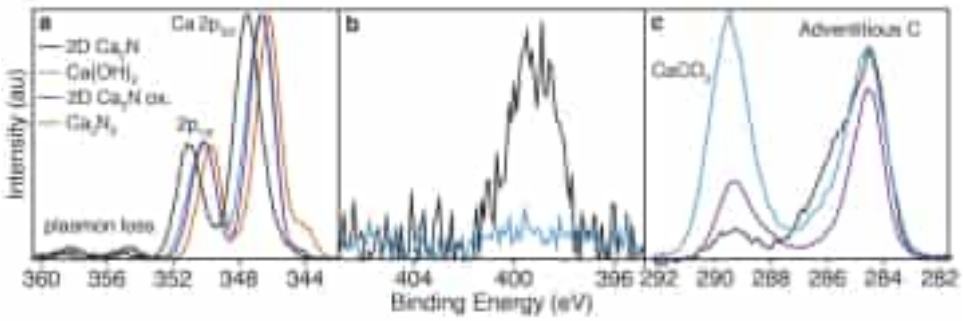


Figure 2.10: Photoemission spectra of calcium nitride and related oxidized species. (a) XPS spectra of core Ca 2p electrons for 2D Ca_2N, deliberately oxidized 2D Ca_2N, Ca_3N_2, and $Ca(OH)_2$. (b) XPS spectra of core N 1s electrons for 2D Ca_2N and $Ca(OH)_2$. (c) C 1s electrons for 2D Ca_2N, deliberately oxidized 2D Ca_2N, and $Ca(OH)_2$.

Furthermore, the C 1s core electron spectra (Figure 2.10c) showed that adventitious carbon species such as adsorbates from 1,3- dioxolane were present on the surface of our 2D Ca_2N. We noticed a trend in the C 1s spectra that the area of the peak at $\sim$289.5 eV increased relative to the area of the peak at 284.6 eV for oxidized 2D Ca_2N, compared to unoxidized Ca_2N (Figure 2.10c). This was observed in all samples and may be indicative of $CaCO_3$ or other C=O bond formation. These species may form when oxidized Ca_2N is exposed to an X-ray.

While the surface composition of Ca_2N and its oxide were characterized, this material likely only had a single oxide product. Therefore, this characterization does not require peak fitting for a surface with multiple oxidation states. To demonstrate this multiple oxidation state peak fitting, the phosphorus 2p core electron peaks of oxidized BP were fit and the the phosphorus oxide on the surface was quantified. The area of the phosphorus oxide peaks were compared to the area of the unoxidized $2p_{3/2}$ and $2p_{1/2}$ peaks, centered at 130.1 eV and 131.0 eV, respectively. The ratio of areas allowed for quantification of the percent of oxide on the surface of the 2D material, summarized in Table 2.2, but could not provide the exact identity of each oxide species. Therefore, we implemented DFT to further interpret this experimental data (Section 2.5.5).

Table 2.2: Percent of phosphorus oxides on thin films of 2D BP

Time (hours)	O_2 (99.999%)	H_2O/N_2 (99.998%)	H_2O/O_2
1	10.7%	8.3%	20.7%
6	23.1%	17.8%	—
1*	20.5 %	22.1%	—
18	33.0%	26.3 %	52.3%

2.5.3.4 Charging

If a sample is not in good electrical contact with the metallic sample holder during XPS, the photoemission of electrons will lead an imbalance of charge. This results in all of the peaks systematically shifting by a finite value. In this dissertation, different substrates were explored in order to facilitate good electrical contact between a material and the instrument. However, this is not always attainable. In cases where samples were insulating or presented evidence of charging, a charge neutralizer was used. The default settings are 1.8 A filament current, 2.8 V charge balance, 0.8 V filament bias. For electrides (Section 2.5.3.5), the settings used

were 2.0 A filament current, 3.2 V charge balance, and 1.0 V filament bias. All spectra were then corrected to the carbon 1s peak for adventitious carbon (284.6 eV).[79]

2.5.3.5 Differential Charging

For conductive homogenous samples in electrical contact with the sample holder, the kinetic energy shifts exactly with the biasing potential; however, if different areas of the sample have different electrical conductivity or photoionization cross sections, then the areas of the sample have different steady-state potentials and some features only shift by a fraction of the biasing potential.[80] Differential charging is more complex than charging because it results in local areas that experience charging differently and therefore, all peaks are offset by non-uniform and inconsistent shifts, resulting in new peaks emerging or peak broadening (Figure 2.11). For example, if a spectra is collected and then the X-ray or UV source illuminates the location for a period of time and a second spectra is then collected, the two spectra will not match. However, if the light is shut-off and the charge within the sample is allowed to dissipate over time, then a third spectra can be collected and it may be similar, but not necessarily identical, to the first. Differential charging presents many challenges for obtaining reliable XPS and UPS spectra.

2.5.3.6 Differential Charging in 2D Electrides

2D electrides are a unique layered material where a free electron gas resides in the interlayer space.[73,81] This highly anisotropic structure leads to complex XPS and UPS, specifically manifesting as different material properties based on orientation and differential charging. As shown in Figure 2.11a, the XPS spectra of Ca 2p core electrons with the charge neutralizer active showed an additional feature that is not present in the spectra when the charge neutralizer is off; this is evidence of differential charging. Similarly in UPS, differential charging affects the secondary electrons emitted and prevented an accurate work function from being measured. The secondary electron cut-off edge E_{SECO} of 2D Ca_2N corrected by the applied bias, shown in Figure 2.11b, have a secondary feature that is induced with increasing applied biases. In Figure 2.11c, the work functions extracted from Figure 2.11b were plotted against the applied bias. The slope of the line ($\Delta\phi/\Delta$bias) varied between samples, but in all cases is much less than 1 (ideally, the slope should be 0, since the ϕ should not change with an applied bias), which suggests that the sample exhibited differential charging. Unfortunately, this also indicated that we could not extract a reliable work function from the surface of the material because the energy of the secondary electrons were dependent on the applied bias and the

degree of differential charging each sample experienced. We tested other metals (eg. Au, Pt) with known work functions and did not observe differential charging. Therefore, we believe that this response was from the Ca_2N sample and not an artifact of the instrument.

While this response could be caused by poor electrical contact between the sample holder and the drop-cast film, this explanation is unlikely because our observation was consistent over many samples and the same observation was made on 3D Ca_2N in two other studies.[78,80] As suggested by others,[78] the response may be related to the highly anisotropic character of the samples that have areas of markedly different work functions.

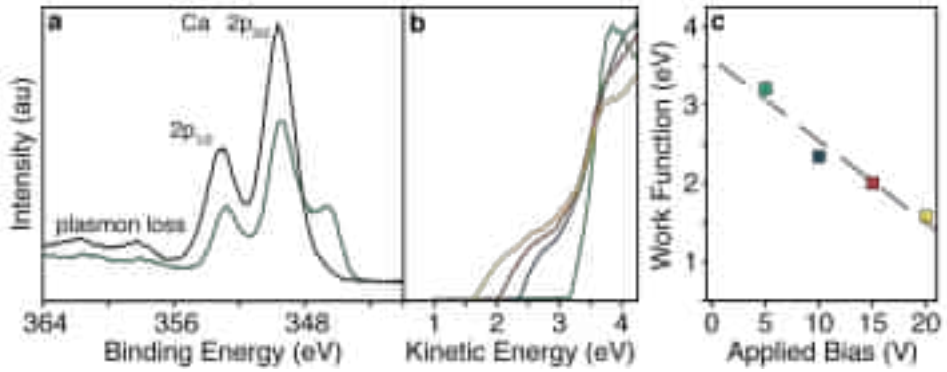


Figure 2.11: Differential charging of samples of 2D Ca_2N. a) XPS spectra of bulk Ca_2N Ca 2p electrons with the charge neutralizer on (green) and with the charge neutralizer off (black). b) UPS spectra of bulk Ca_2N with 5V (green), 10V (blue), 15V (red), and 20V (yellow) applied biases at the secondary cut-off energy, E_{SECO}. The spectra are corrected to account for the different applied biases. (c) Work function ϕ plotted against the applied bias for one sample of 2D Ca_2N.

2.5.3.7 Introduction to UPS

UPS provides information about the valence band of the material and the density of states near the Fermi energy edge, allowing information about the electronic nature of a material to be determined. Generally, UPS allows for calculation of the work function ϕ of a material. The work function is related to the Fermi energy of the instrument E_F, the energy of the incident photon $h\nu$, and the lowest kinetic energy at which electrons are emitted at the secondary electron cut-off energy, E_{SECO}.

$$\phi = h\nu - (E_F - E_{SECO}) \tag{2.2}$$

2.5.3.8 Metallic Nature of 2D Ca_2N by UPS

The density of states at the Fermi energy level E_F demonstrated that the electronic structure of our 2D Ca_2N is metallic (Figure 2.12). The work function of our material could not be quantified because all samples of bulk and 2D Ca_2N showed evidence of differential charging (Figure 2.11), in agreement with previous reports.[78]

In order to measure the metallic character of Ca_2N and not the substrate, we cast films much thicker than the escape depth of electrons. We characterized the films by XPS and then cleaned the surface of the films by argon ion sputtering. The quality of substrate coverage by Ca_2N was assessed by measuring the area of peaks from Pt or Au (Figure 2.12b). We performed sputtering twice for 15 minutes, each time with an accelerating voltage of 1kV and an emission current of 10 mA. The resulting spectra are shown in the Figure 2.12. After sputtering the surface of 2D Ca_2N, we used XPS to determine the relative content of carbon (Figure 2.12a), platinum (Figure 2.12b), calcium (Figure 2.12c), and nitrogen (Figure 2.12d). We found that the carbon content decreased as sputtering time increased and that the calcium and nitrogen content increased. This is consistent with the removal of hydrocarbons from the surface of 2D Ca_2N. Furthermore, the unchanged position and shape of the calcium and nitrogen peaks after the sputtering indicated that we were not changing or damaging our material during the sputtering process. Additionally, this verified that the film is generally thicker than the escape depth of the electrons since peaks from the Pt substrate (Figure 2.12b) were barely detectable. Furthermore, the density of states up to the Fermi edge (Figure 2.12e) became more prominent as hydrocarbons were removed from the surface of our thick film. Because XPS probes even deeper into the sample than UPS, we are confident that the density of states at the Fermi edge probed in our UPS measurements are exclusively attributable to the film of 2D Ca_2N and not the substrate.

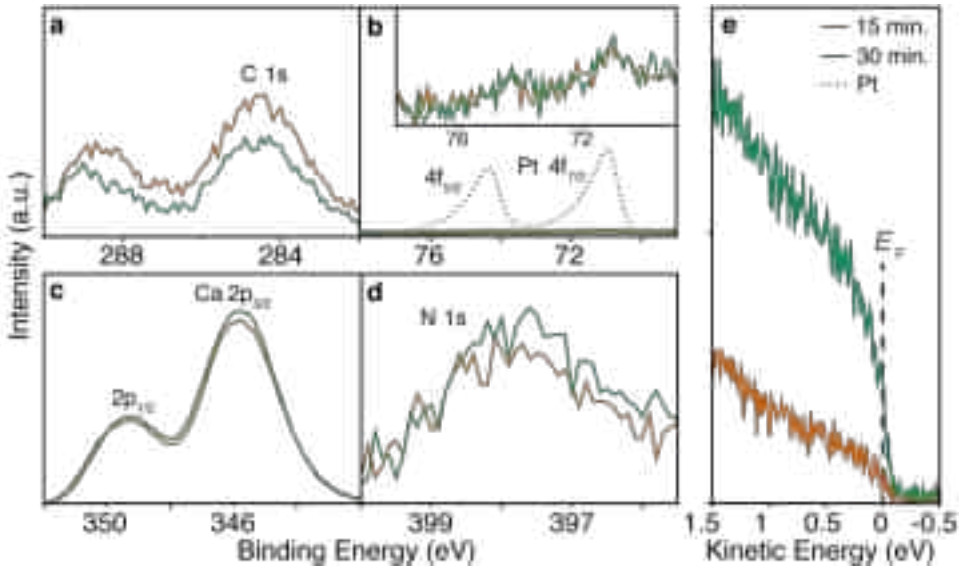


Figure 2.12: Photoemission spectroscopy of a thick film of 2D Ca_2N on a platinum-coated silicon wafer. After sputtering the film with argon ions to remove surface contamination, the film was characterized. In XPS, (a) the carbon content on the surface of 2D Ca_2N decreased as sputtering time increased from 15 minutes (orange) to 30 minutes (green). (b) The Pt film is almost entirely covered by Ca_2N, as shown by the extremely small peaks at 71.1 and 74.4 eV. The dashed line shows the positions of a bare Pt substrate; the intensities of the dashed line were reduced by a factor of 30. The inset shows a magnified version of the intensities for the Pt core electron binding energies on the film with 2D Ca_2N, showing that the Pt signal does not increase with sputtering time. (c) The calcium and (d) nitrogen peaks increase in area as hydrocarbons are removed by sputtering. (e) In UPS measurements, as hydrocarbons are removed, the density of states at the Fermi edge become more prominent and provides evidence for the metallic character of 2D Ca_2N.

2.5.4 UPS & Band Diagram

The work function ϕ of a material determined from UPS can be used to provide insight into the band diagram, as well as the thermodynamic feasibility of subsequent reactions. The work function ϕ determined by UPS is relative to absolute vacuum. In the case of a semiconductor, such as BP, this allowed us to approximate the positions of the valence band and the conduction band (Section 3.3.5, Figure 3.6) relative to vacuum E_{abs}. Therefore, in order to determine whether a reaction with our 2D material is thermodynamically favorable, reduction potentials E of a chemical species and the work function of our material can be compared to determine if a reaction could occur. However, tabulated reduction potentials for chemical half reactions are always determined by a relative difference in potential to another electrode and are often not reported with respect to E_{abs}.

The most common reference electrodes are the standard hydrogen electrode (SHE, Equation 2.3) and normal hydrogen electrode (NHE). As depicted in Equation 2.3, the SHE requires all activities a to be unity. However, this is often not the case and deviations from standard conditions are accounted for in the Nernst Equation (Equation 2.4).

$$\mathrm{H}^+(aq) + e^- \rightleftharpoons \frac{1}{2}\mathrm{H}_2(g) \qquad E^o = 0\ \mathrm{V}, \qquad \mathrm{pH} = 0, \qquad \mathrm{P}_{(\mathrm{H}_2)} = 1\mathrm{atm} \tag{2.3}$$

$$E = E^o - \frac{\mathrm{RT}}{n_e F} \ln Q \tag{2.4}$$

where R is the ideal gas constant, T is temperature, n_e is the number of electrons transferred, and Q is the reaction quotient. To convert from potentials reported with respect to E_{SHE} to E_{abs} at the same temperature of 25°C , Equation 2.5 may be used.

$$-E_{abs} = E_{\mathrm{SHE}} + 4.44(\pm 0.02)\mathrm{V} \tag{2.5}$$

In the NHE, the concentration of H^+ is 1 M. Therefore, the a of the H^+ is ≈ 0.8. By accounting for the change in the activity coefficient of the proton in the Nernst Equation (Equation 2.4), the conversion between the NHE and SHE is shown in Equation 2.6.

$$E^o_{\mathrm{SHE}} = E^o_{\mathrm{NHE}} + 0.006\mathrm{V} \tag{2.6}$$

After converting reduction potentials relative to E_{abs}, the feasibility of an electron or hole transfer between a 2D material and a reaction can be explored. See Section 3.3.5 and Figure 3.6.

2.5.5 DFT

In this dissertation, *ab initio* Density Functional Theory (DFT) was used to theoretically investigate the effect of local chemical environments on binding energies that can be experimentally observed in XPS spectra. A projector augmented wave (PAW) pseudopotentials[82] was implemented in the VASP code[83] and the Perdew-Burke-Ernzerhof (PBE) functional[84] was used to describe the the electronic exchange and correlation. Core-electron binding energies E_B^F were calculated through the implementation of "equivalent

cores" or "Z+1" approximation (Figure 2.13).[85–89] To determine the core-electron binding energy shift ΔE_B^F between different oxidized species, a thermodynamically equivalent Born-Haber cycle was implemented. A linear combination of the energies of each of these steps allows for the calculation of the core-electron binding energy E_B^F of the oxidized atom of interest. This process is discussed with respect to the oxidation of 2D and FL BP in Section 3.3.3 and depicted in Figure 3.4.

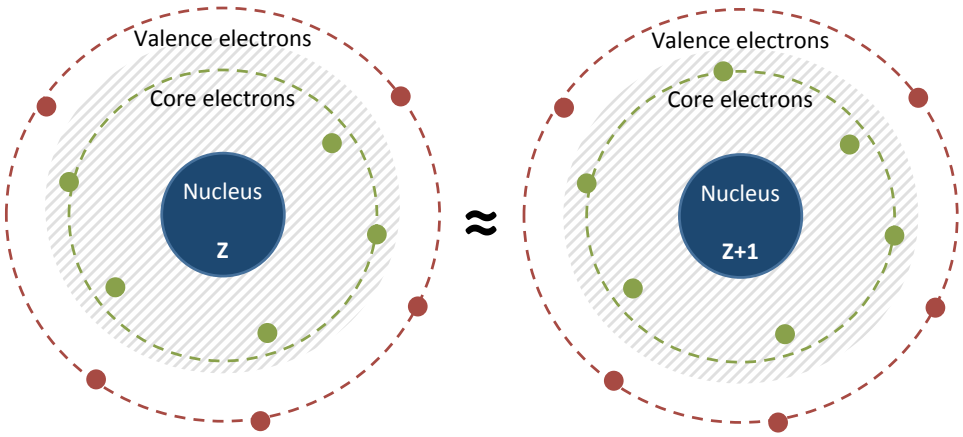


Figure 2.13: Equivalent cores approximation: An atom with a nucleus with Z protons and one removed core-electron is equivalent to a nucleus with $Z + 1$ protons and one valence electron removed.

2.5.6 Raman Spectroscopy

Raman spectroscopy provides information about the vibrational states in polarizable molecules. In Raman spectroscopy, an incident photon interacts with the material. If the interaction is elastic and the photon scatters without any energy loss, Rayleigh scatting (Figure 2.14a,b) occurs and does not provide any insight into the material. However, if the photon inelastically interacts with the material, the photon may be emitted at a lower (Figure 2.14c) or higher (Figure 2.14d) energy than the incident photon (ΔE). These shifts are known as Stokes and anti-Stokes Raman scattering, respectively, and the energy lost or gained is directly proportional to the spacing of vibrational energy levels. Furthermore, the intensity of a peak in a Raman spectra is directly proportional to the concentration of the Raman-active species. Therefore, Raman scattering provides information about the local chemical composition of a material.

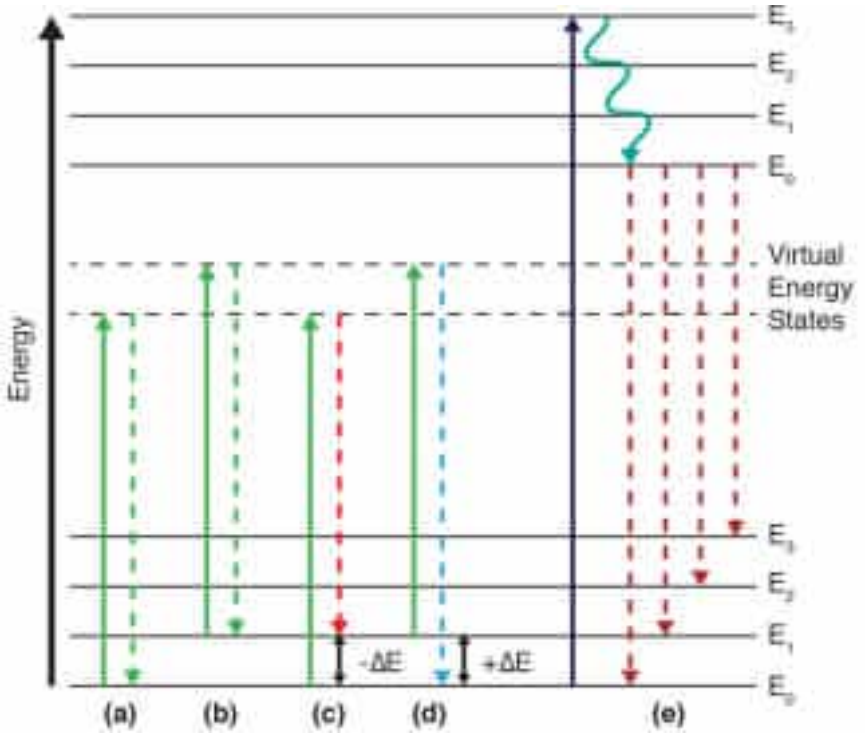


Figure 2.14: The interaction between an incident photon and a material can lead to different excitations (upward arrows) and emissions (downward arrows). Emissions that result in (a,b) elastic Rayleigh scattering and inelastic (c) Stokes or (d) anti-Stokes Raman scattering are the result of incident photons that do not have sufficient energy to cause the material to reach an excited state. However, (e) fluorescence occurs if the excitation wavelength is sufficient to create an excited state and undergo a decay before emitting photon as the material returns to ground state.

The spatial resolution that can be achieved and locally-probed is diffraction limited by the laser excitation wavelength λ_o and the microscope objective. Generally, the diameter of the probed area is determined according to Equation 2.7,

$$D = \frac{1.22\lambda_o}{\text{NA}} \tag{2.7}$$

where D is the spot diameter, λ_o is the excitation wavelength, and NA is the numerical aperture of the microscope objective. For example, a 633 nm laser with a 50X objective and NA of 0.75 has a theoretical diameter of 865 nm. In reality, the area probed by Raman spectroscopy will be larger ($\sim$ 1μm) due to events such as scattering and interactions at interfaces.

Because Raman spectroscopy is solely dependent on the energy of vibrational levels, it is independent of the excitation wavelength. Therefore, using Equation 2.7, it can be seen that the spatial resolution of this

technique can be increased by using shorter wavelength (higher energy) lasers and objectives with higher NAs. However, if an excitation source has sufficient energy, the material can reach an excited state and fluorescence processes can occur (Figure 2.14e). These processes can interfere with Raman scattering and can lead to a drastic increase in the background of a spectra, making data fitting and processing more difficult. It is important to note that a resonance Raman effect might be able to be exploited at shorter wavelengths, despite the fluorescence background. In this dissertation, Stokes Raman scattering was used to observe and characterize 2D materials and excitations wavelengths were selected to minimize fluorescence. For example, the band gap of BP can be excited by wavelengths shorter than ≈ 600 nm, which induce fluorescence in the Raman spectra. Therefore, BP was characterized by 633 or 785 nm laser excitations.

2.5.6.1 Raman Spectroscopy of 2D BP & Oxide

Raman spectra of thin films of 2D BP were attained using a Reinshaw inVia Raman Microscope with an excitation wavelength of 633 nm, a 1200 l/mm grating, and 50X objective. The samples were sealed under N_2 between a glass microscope slide and cover slip, which were sealed with a two-part epoxy (Loctite® Hysol® 1C) which cured at room temperature in a glovebox for a minimum of 36 hours. The Raman active modes of the unoxidized 2D BP thin films, shown in Figure 2.15 were observed at 360.82 cm^{-1}, 438.08 cm^{-1}, and 465.74 cm^{-1} for the A_g^1, B_{2g}, and A_g^2 modes, respectively, in good agreement with previous literature.[59,90,91] While the intensity ratio of the active modes is dependent on sample thickness and orientation due to its anisotropic crystal structure,[92] previously, the ratio of the integrated intensity of the A_g^1 to A_g^2 peak was observed to be sensitive to the degree of oxidation.[59] A ratio greater than 0.2 indicates low degrees of material oxidation.[59] Unoxidized thin films of 2D BP had an average A_g^1 to A_g^2 integrated intensity ratio of 0.71 for 35 spectra acquired from different flakes, further validating the pristine quality of 2D BP. For a thin film exposed to H_2O/O_2 for 18 hours, the A_g^1, B_{2g}, and A_g^2 modes were located at 360.82 cm^{-1}, 466.57 cm^{-1}, and 438.09 cm^{-1}. The intensity ratio of the A_g^1 to A_g^2 peaks was 0.63. Thin films of the material exposed to H_2O for 18 hours had A_g^1, B_{2g}, and A_g^2 modes located at 361.01 cm^{-1}, 438.08 cm^{-1}, and 465.92 cm^{-1}; furthermore, these films had an average integrated intensity ratio of the A_g^1 to A_g^2 peaks of 0.52. This indicates that the degree of oxidation (1) after short-term exposures to ambient conditions and (2) after exposure to a single oxidant cannot be adequately probed by Raman spectroscopy. In previous literature, it was noted that exposure to O_2 or H_2O individually does not exhibit evidence of degradation in Raman spectroscopy,[59] and the results presented here provide evidence that Raman spectroscopy is not a good means of detecting

early stages of oxidation, especially for single-oxidant environments. Therefore, we did not rely on Raman spectroscopy as strong evidence for degradation, but utilized it to confirm that the sample has 2D BP after oxidation.

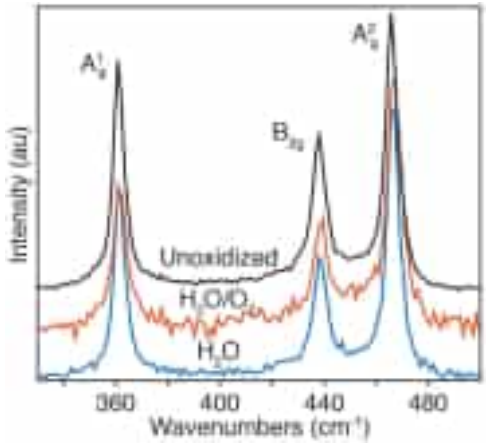


Figure 2.15: Raman spectra of 2D BP thin films for unoxidized material (black) and after 18 hours of exposure to H_2O/O_2 (orange) or H_2O (blue) oxidants.

2.6 Simulations of Optical Response to Carrier Concentration

To calculate optical spectra and local electric field profiles, the finite-difference time-domain software (FDTD Solutions from Lumerical, Inc.) was utilized. A mono- to few-layer anti-dot graphene array was modeled on a $\sim$ 1μm substrate, as shown in Figure 2.16 at wavelengths spanning the UV to THz spectra (300 nm – 20 µm, 500 – 33,333 cm^{-1}, 60 meV – 4.1 eV).

2.6.1 Simulation Environment

A graphene hexagonal anti-dot structure (Figure 2.16) was placed on top of a substrate with holes etched in the simulation environment from the top of the substrate through the graphene and above the surface of the graphene by 5 or 10 nm. To best approximate experimental characterization conditions, a silicon wafer with a thermal oxide was used as the substrate for simulations spanning the MIR and THz spectra, while a glass microscope slide was used for simulations in the NIR and VIS spectra. In the THz and MIR spectra, the substrate is composed of 0.97 μm Si with a constant refractive index of n = 3.4, a 285 nm SiO_2 layer with a constant refractive index of n = 1.45, and 20 nm layer of ITO with a constant refractive index of n =

2.3 (Figure 2.16b). For the NIR and VIS spectra the substrate was SiO_2 with the 20 nm film of ITO (Figure 2.16c). Details of the refractive index of the graphene are provided in Section 2.6.2.

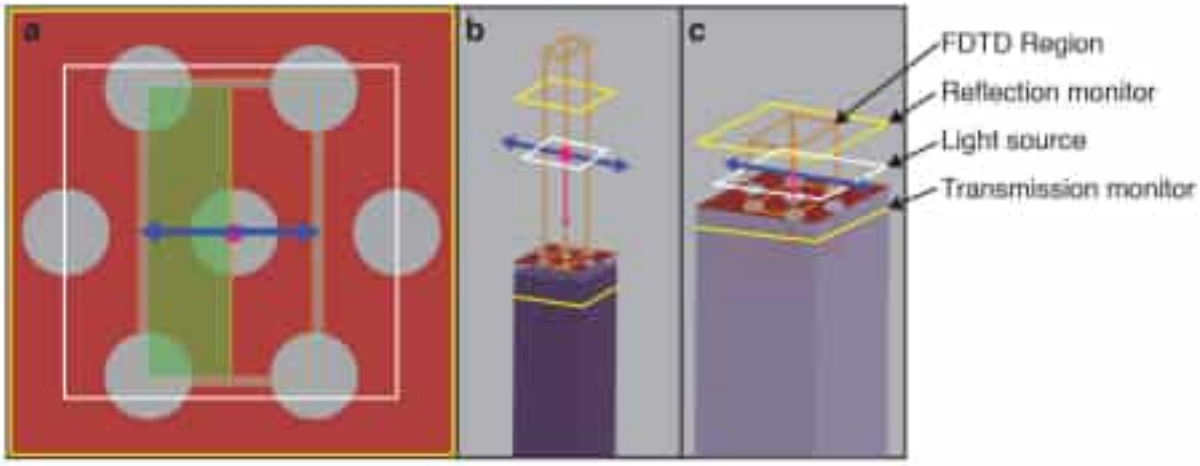


Figure 2.16: Simulation environment of a hexagonal anti-dot array of mono- to few-layer graphene as viewed from (a) the top-down (e.g. xy) plane, (b) a side perspective of the THz and MIR simulated structure, and (c) a side perspective of the NIR and VIS simulated structure. The FDTD calculation region is outlined in orange with the green indicating the anti-symmetric x-plane approximation, the plane-wave light source is outlined in white with the pink arrow indicating the propagation direction and blue arrows indicating the electric-field orientation, and each monitor is outlined in yellow.

2.6.1.1 FDTD Region

The simulation region is composed of the FDTD region, a light source, monitors, and a fine mesh. In this simulation, graphene is placed in the xy-plane. Thus, the boundaries in the x, y, and z-planes were set to be anti-symmetric, periodic, and PML respectively where the x- and y-boundaries encase the smallest unit cell (Figure 2.16a) and the z-boundary is parallel to the graphene vdW surface. By selecting the x- and y-boundaries to be anti-symmetric and periodic, the unit cell is assumed to be infinitely repeating and computation time of the simulations was decreased. The PML boundaries were positioned at $\lambda/2$ from vdW surface of the 2D material, where λ was the longest incident wavelength. For the THz and MIR simulations, which extend to 20 µm, the z-boundaries were 5 µm from the graphene surfaces. For NIR and VIS simulations, which extend to 3 µm, each z-boundary is positioned 750 nm from the graphene surfaces. Furthermore, the type of PML boundaries were stretched coordinate with a steep angle profile with 40 layers.

The simulation time was set to 4000 fs at 300K with an auto shutoff of 10^{-8} at a mesh accuracy of 8. The mesh type was auto non-uniform with a conformal variant 0 mesh refinement and minimum mesh step of

0.0025 nm. The light source used is a Bloch/periodic plane wave at 0° polarization propagating perpendicular to the graphene surface (Figure 2.16). The incident light was laterally larger than the FDTD region, but smaller than the lateral dimensions of the transmission and reflection monitors (Figure 2.16a). This size ratio ensures that the entire unit-cell is properly illuminated, with adequate propagation to the monitors. It is important to note that monitors were not placed within the grey field of the light light source, nor within a PML boundary, as these positions cause artificial artifacts in the optical spectra.

Reflection and transmission monitors were frequency-domain field and power monitors, placed parallel to the graphene vdw surface. The reflection monitor lies behind the light source and the transmission monitor lies 620 nm behind the graphene structure, each with the same lateral dimensions as the substrate. The position of each of these monitors is selected to allow the light to properly propagate in the simulation. Additionally, a frequency-domain field profile monitor is placed at the interface of the graphene and substrate, to measure the local electric field enhancement.

2.6.1.2 Meshing and Mesh Order

Each component of the substrate (e.g. ITO, SiO_2, Si) and sample (e.g. graphite or KC_8) has a mesh order of two, while the holes have a mesh order of three. The mesh order of the holes must be selected to be greater than the material being etched to ensure that the software does not approximate the holes with an incorrect refractive index. Index monitors were used, parallel and perpendicular to the interface between the anti-dot array and the substrate, to ensure the refractive index of each hole (e.g. vacuum n=1), substrate (e.g. ITO n = 2.3), and graphene were accurate. Furthermore, there were discrepancies in the refractive index of the graphene for sufficiently small structures; this was attributed to insufficient mesh sizes. Therefore, for all simulations in this dissertation, a fine mesh was placed around the smallest unit cell of the anti-dot graphene layer, extending 5 nm above and below. The fine mesh size must be at least a fourth of the smallest dimension. Furthermore, it must be symmetric in the xy plane since periodic and anti-symmetric boundaries are used. In the THz and MIR simulations, this fine mesh step-size ranged from one to three nm, depending on the radius of the holes. In the NIR and VIS spectra, the fine mesh step-size was 1/6th of the material thickness.

2.6.2 Doping & Refractive Indicies

When graphene is doped, the E_F shifts as a result of changes in the carrier concentration. The extent of doping alters the refractive index and therefore, the optical properties.[43] Here, we employed low and high levels of doping, which are experimentally attainable by electrostatic and electrochemical methods.

2.6.2.1 Electrostatically Doped-Graphene: Conductivity Model

A conductivity model with an angular frequency ω, chemical potential μ_c, scattering rate Γ, and temperature T can model the inter- and intraband contributions (Equation 2.8) in the optical response of graphene with low doping concentrations.[53] In this dissertation, simulations in the THz and MIR regions defined graphene as a 2D surface conductivity model with infinitesimally small thickness, with a temperature of 300 K, a scattering rate of 0.001 eV, and the chemical potential varied from 0.1 eV to 0.8 eV. In this model, the chemical potential resembles electrostatic doping of the material. Furthermore, as the number of layers increases from one to six, the conductivity of the graphene is linearly scaled.

$$\sigma(\omega, \mu_c, \Gamma, T) = \sigma_{inter}(\omega, \mu_c, \Gamma, T) + \sigma_{intra}(\omega, \mu_c, \Gamma, T) \tag{2.8}$$

The intra- and interband contributions can be described according to Equation 2.9 and 2.10, respectively, where $\hbar$ is the reduced Planck constant.

$$\sigma_{intra}(\omega, \mu_c, \Gamma, T) = -\frac{ie^2}{\pi\hbar^2(\omega + i2\Gamma)} \int_0^\infty \epsilon \frac{\partial f_E(\epsilon) - \partial f_E(\epsilon)}{\partial \epsilon} \partial\epsilon \tag{2.9}$$

$$\sigma_{inter}(\omega, \mu_c, \Gamma, T) = \frac{ie^2(\omega + i2\Gamma)}{\pi\hbar^2} \int_0^\infty \frac{f_E(-\epsilon) - f_E(\epsilon)}{(\omega + i2\Gamma)^2 - 4(\frac{\epsilon}{\hbar})^2} \partial\epsilon \tag{2.10}$$

where f_E is the Fermi-Dirac distribution (Equation 2.11) for energy ϵ and Boltzmann constant k_B.

$$f_E = (exp^{\frac{\epsilon - \mu_c}{k_B T}} + 1)^{-1} \tag{2.11}$$

In this conductivity model, the extent of doping is restricted to the Dirac cone (Figure 4.2), which effectively limits the extent of electrostatic doping to < 1 eV. This is because at frequencies below $2E_F$, intraband transitions dominate in the THz region and MIR region, while interband transitions dominate at

frequencies above $2E_F$ (e.g. NIR and visible regions). Thus, at low doping levels, the interband contributions are negligible and the intraband contributions can be approximated as Drude conductivity according to Equation 2.12 as temperature approaches zero.[13] Therefore, this model is applicable in the THz and MIR regions, but not valid in the NIR and VIS spectra.

$$\sigma_{intra}(\omega, \mu_c, \Gamma, T) = -\frac{ie^2}{\pi\hbar^2(\omega + i2\Gamma)} \tag{2.12}$$

2.6.3 Electrochemically Doped-Graphene: Drude Model of KC_8

With high doping levels, such as those attained in electrochemically produced KC_8, the material can be treated as a metal.[1] Therefore, the Drude model (Equation 1.1) can be used to relate the optical properties to the carrier concentration N.

In this dissertation, an anti-dot structure of KC_8 with a finite thickness was simulated in the NIR and VIS spectra. The frequency-dependent complex dielectric for KC_8 was calculated using Equation 2.13,

$$\varepsilon = \varepsilon_\infty - \frac{\omega_p^2}{\omega(\omega + i\gamma)} \tag{2.13}$$

where γ is the damping factor and ω is the angular frequency of incident light. In our calculations, ω_p and γ were approximated as unit-less quantities 7.3 and 0.383, respectively, and ε_∞ was assumed to be 8, similar to values determined based on experimental data in Ref.[1].

Equation 2.13 can be separated into the real (Equation 2.14) and imaginary (Equation 2.15) components.

$$\varepsilon_1 = \varepsilon_\infty - \frac{\omega_p^2}{\omega^2 + \gamma^2} \tag{2.14}$$

$$\varepsilon_2 = \frac{\omega_p^2\gamma}{\omega(\omega^2 + \gamma^2)} \tag{2.15}$$

Then , the refractive indexes $n + ik$ are calculated according to Equation 2.16, 2.17.

$$n = \sqrt{\frac{\varepsilon_1 + \sqrt{\varepsilon_1^2 + \varepsilon_2^2}}{2}} \tag{2.16}$$

$$k = \sqrt{\frac{\varepsilon_1 - \sqrt{\varepsilon_1^2 + \varepsilon_2^2}}{2}} \tag{2.17}$$

The refractive index of KC_8 (Figure 2.17b) is more similar to metals like Ag and Au (Figure 2.17c,d), than it is to graphene (Figure 2.17a). The validity of the calculated n and k values for KC_8 was determined by comparison of simulated reflection spectra to literature data for freestanding 900 nm[93] and experimental data for 54 nm KC_8.

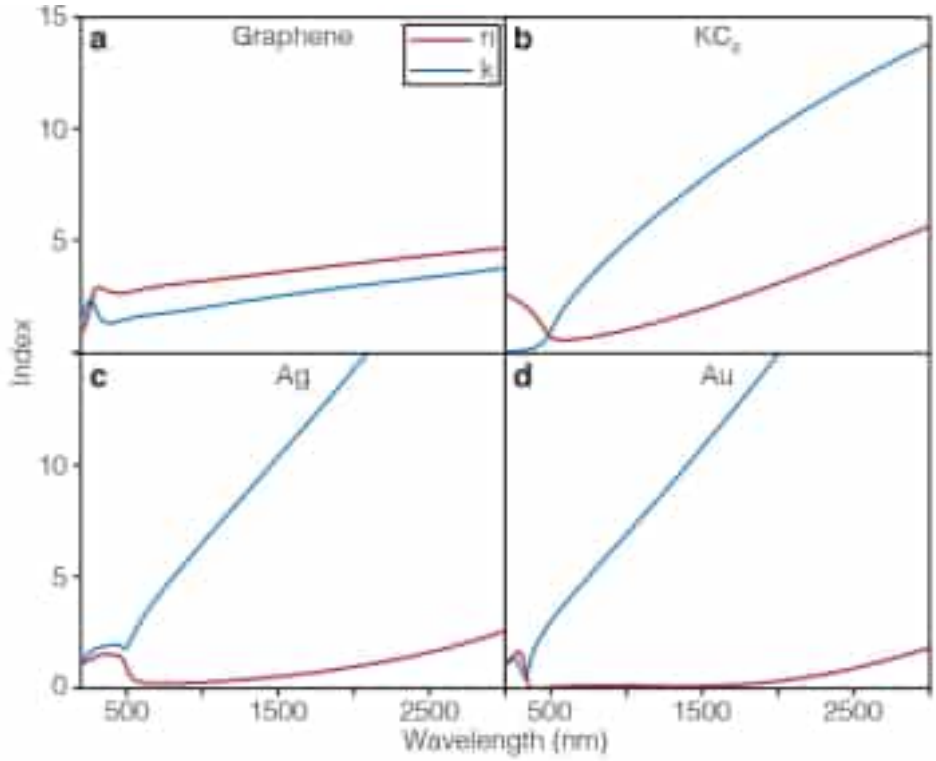


Figure 2.17: Refractive index n, k for (a) graphene, (b) KC_8, (c) Ag, and (d) Au. These refractive indexes are from (a) Ref. 92 and (c,d) Ref. 93.

2.6.4 Parameter Space

In simulations, the plasmonic response of mono- and FLG anti-dot lattices were investigated. We investigated the effect of geometric variations: radius, periodicity, and number of layers. In these, the hole diameter was varied from 10 to 25 nm, the periodicity spanned 60 to 120 nm, and the thickness was 1 to 6 layers. Furthermore, the carrier concentration explored was low to high levels of doping (0.1 – 1.35 eV) corresponding to in-plane carrier concentrations of $1 \cdot 10^{12}$ – $5 \cdot 10^{14}$ cm^{-2}.

2.7 Experimentally Altering Carrier Concentration

Intercalation methods developed for bulk materials were successfully applied to 2D materials in this work. More specifically, thermal intercalation of guest species, such as K [1] or I_2 [6], and electrochemical solution-phase intercalation methods were applied to anionic, neutral, and cationic guests, including HSO_4^-/H_2SO_4,[75,76] $FeCl_3$,[94,95] and K^+.[96,97]

2.7.1 Thermal Intercalation

Isothermal vapor transport is gaseous intercalation method in which the host lattice and guest are held at a temperature at which the guest species vaporizes, enters the lattice, and diffuses in the interlayer space.[39] Stage 1 KC_8 was produced by isothermally intercalating K into graphite and FL graphene at 200°. To synthesize this graphite intercalation compound (GIC), the sample (bulk graphite powder or 2D exfoliated flakes on a SiO_2-based substrate) was placed in a quartz tube with one sealed end. Then, the tube and material were pumped into a nitrogen glovebox. It is important to note that the quartz tube was dry before loading the K. This was achieved by either heating the quartz overnight in a furnace at 150° or placing it under vacuum overnight. In the glovebox, K was cut under heavy mineral oil, to remove any surface oxidation. Then, it is rinsed with anhydrous hexanes. The K was then loaded in the quartz tube and ~ 1 mL of hexanes were placed in the tube, enough to cover the K. Parafilm was placed on the end fo the tube. The tube was removed from the glovebox, immediately placed under vacuum, and sealed with an oxyhydrogen torch.

The tube was heated at 200°C for 24 hours and then the furnace was shutoff and allowed to cool to room temperature. The rate of heating and cooling were not important in the synthesis of this GIC. The quartz tube was opened in a glovebox under dry, inert atmosphere. The host was observed to have a physical color change from dark grey to lustrous gold, shown in Fig. 1.5, both in bulk and 2D form.

Due to the reactivity of K with water, all materials used in the synthesis and handling of KC_8 were cleaned with IPA before being exposed to any water conditions.

2.7.2 Electrochemical Intercalation

With the recent emergence of 2D and few-layer intercalation compounds,[1,6] electrochemical methods facilitate *in situ* study of the intercalation. With electrochemical intercalation, the layered or 2D host must be electrically conductive, although it may be feasible for an ultra-thin material with very low conductivity to be

intercalated electrochemically if placed on a conductive substrate. Additionally, the host (e.g. a thin film or single flake) needs electrical contact with a voltage source (Figure 2.4a,d); a Biologic SP-300 potentiostat was used to intercalate a 2D material by either chronopotentiometry (CP) or cyclic voltammetry (CV). Furthermore, I developed an electrochemical cell, shown in (Figure 2.4a,c,d), that allows for *in situ* optical or electrochemical characterizations to be used.

2.7.2.1 Planar Battery Cell

A planar battery cell was developed to allow for *in situ* optical measurements during electrochemical experiments, depicted in Figure 2.4a,d and described in Section 2.3.4. It is important to note that the metal electrodes, deposited by sputtering in a Kurt Lesker® 75 sputtering instrument at vacuum of $\leq 5 \cdot 10^{-5}$ torr, were selected to be compatible with the aqueous or non-aqueous electrolyte. Additionally, it is important to note that in the cases where an adhesive metal, such as Ti or Cr, was used between the substrate (e.g. glass) and electrode metal (e.g. Au or Pt), Pourbaix diagrams were used to determine the stability of this metal with the given experimental conditions.[98]

In this setup, 2D material was placed on a conductive substrate (e.g. 10 0nm Pt/ 5 nm Ti/ glass microscope slide or a highly p-doped Si wafer). This 2D material can be in the form of a thin film (Figure 2.18a) or individual flakes (Figure 2.18b). For thin films, polyvinylidene fluoride (PVDF) was used as a binding agent to facilitate good adhesion between a film of 2D flakes and a metal substrate. To create these films, slurries of 2D material and PVDF in NMP were drop-cast (Section 2.3.3) onto the substrate and heated at $150°$C for 24 hours. Then this substrate was placed in contact with an external voltage source. Additionally, the counter electrode (e.g. Al for $NH_4(SO_4)_2$, Pt/Ti for H_2SO_4 or $FeCl_3$) was placed in electrical contact with the voltage source. Then the sample was sealed in a reservoir by an epoxy on the microscope slide. An electrolyte (e.g. 1 M $NH_4(SO_4)_2$, 10 M H_2SO_4, or 8-10 M $FeCl_3$ in propylene carbonate) was added and then the sample was sealed with a glass coverslip. It is important to note that the electrolyte was purged of oxygen and all non-aqueous electrolytes were anhydrous. After the epoxy cured, samples were characterized by CP and/or CV with *in situ* optical microscopy techniques.

2.7.2.2 *In situ* Raman Spectroscopy

In addition to observing optical changes of a flake with intercalation, we were able to characterize the charger transfer between the FL host and the guest species by *in situ* Raman Spectroscopy, shown in Figure

2.18, during and after intercalation. As shown in Figure 2.18, as a guest inserts into graphite, the frequency of the G peak shifts to higher energies. This shift is indicative of the graphite materials becoming hole-doped. Additionally, as the material becomes progressively more doped, the G peak shifts to higher energies (Figure 2.18). It is important to note that performing *in situ* Raman spectroscopy in electrolytes with large heat capacities (e.g. water) can cause issues with heat dissipation during characterization. This has lead to local degradation of the material during measurements. It is best practice to minimize the amount of electrolyte and the laser exposure time.

We found that as intercalation proceeded, we observed low stages of doping (e.g. Stage 4) that progressed to high stages of doping (e.g. Stage 1). Shown in Figure 2.18, as intercalation occurred, the G peak of the graphite is seen at ~ 1580 cm^{-1} while a second peak (labeled GIC) emerges at $\sim 1601 - 1605$ cm^{-1} for low doping. With continued intercalation, the second peak shifts to higher energies, ~ 1615 cm^{-1} for stage 2 and ~ 1625 cm^{-1} for stage 1—which is the highest stage of intercalation. These values are in agreement with literature values.[95,99] With this experiment, we were able to observe FL intercalation both qualitatively (optical microscopy images) and quantitatively (CP and Raman spectroscopy), which is exciting for the potential application of these materials in optoelectronic devices.

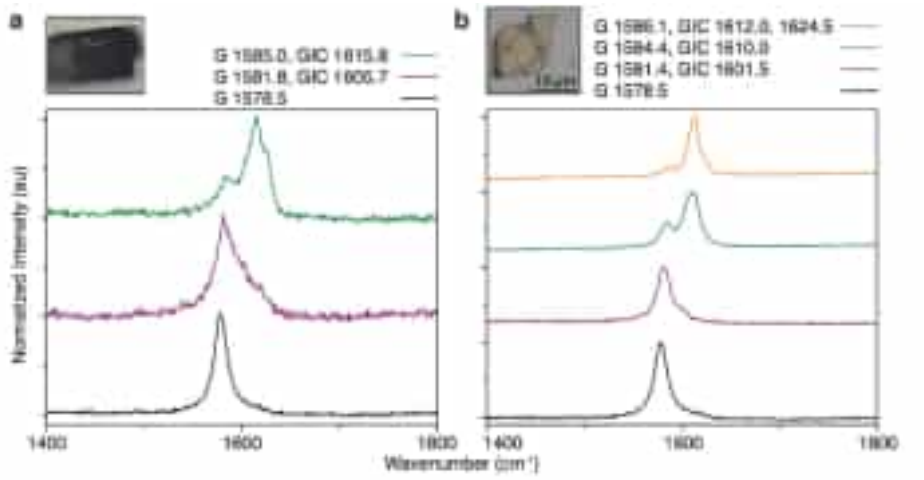


Figure 2.18: *In situ* Raman spectroscopy of intercalation of graphite with 10 M $FeCl_3$ in propylene carbonate for a (a) thin film and (b) individual flakes.

CONTROL OF SURFACE AND EDGE OXIDATION PHOSPHORENE

3.1 Introduction

In two-dimensional (2D) materials, the majority of atoms are located at surfaces, therefore surface chemistry is important in determining intrinsic properties. For example, graphene is a zero gap 2D semimetal with ultrahigh mobility and conductivity,[12,15] while graphene oxide can be insulating or semiconducting.[12,64,65,100] In emerging materials like phosphorene—the 2D form of black phosphorus—understanding and controlling surface chemistry is considered essential to future applications of the material.[61,63,101,102]

Like graphene and graphene oxide, phosphorene and phosphorene oxide have exceptional properties. Phosphorene is especially interesting because it has a thickness-dependent band gap that ranges from 0.3 eV in bulk to approximately 2.1 eV in a monolayer,[26,30–34] a range that is greater than most quantum dots. Furthermore, 2D black phosphorus has optical and electrical anisotropy,[92,103,104] high carrier mobility,[32,105] and both n- and p-type behavior.[32,106,107] These properties suggest potential uses in optoelectronic technologies, including transistors,[106,108,109] solar energy conversion,[23,107,110,111] and photodetectors.[104,112,113] Many other types of applications, including batteries,[114,115] gas sensors,[35,116–118] catalysts,[23,119] and medicine,[119,120] will require control over phosphorene's surface chemistry and reactivity.

Phosphorene and black phosphorus are known to oxidize in ambient conditions,[36,59–61,63,121–123] yielding insulating phosphorene oxides and low atomic weight fragments.[124] These oxides have tunable properties that depend on composition; for example, band gaps up to 8.5 eV have been predicted[35,36] and photoluminescence has been observed.[125] With a tunable band gap from semiconducting to insulating and interesting electronic properties,[35,36,126] 2D phosphorene oxide demonstrates potential use in optoelectronics, such as an electronic on/off switch,[35,36,126] a transparent encapsulation layer,[35,36,126] or a gas sensor.[35] The observation that

[1]This chapter is reproduced from Kuntz, K. L.; Wells, R. A.; Hu, J.; Yang, T.; Dong, B.; Guo, H.; Woomer, A. H.; Druffel, D. L.; Alabanza, A.; Tománek, D.; Warren, S. C. Control of Surface and Edge Oxidation on Phosphorene. *ACS Appl. Mater. Interfaces* **2017**, *9126-9135*. Copyright 2017 American Chemical Society.

phosphorene oxidizes under ambient conditions suggests that oxidation reactions are an important class of surface reaction chemistries that could be used to functionalize phosphorene's surface. The development of oxidation chemistries may also provide new pathways to stabilize phosphorene against degradation under ambient conditions.

This work investigates the oxides of 2D black phosphorus through experimental surface characterization coupled with simulations—exploring how oxidant conditions modify the surface chemistry of 2D phosphorene oxide at defect (edge, step, grain boundary, etc.) and non-defect sites. We present evidence for the selective oxidation of the van der Waals surface (i.e. the basal surface) or edges and other defect sites of few-layer phosphorene through the choice of oxidant. Ultimately, the ability to selectively modify the basal surface or edge states presents opportunities to engineer the properties of 2D materials through covalent functionalization and defect passivation.

Many techniques have been used to study the oxidation of black phosphorus, providing insights into the chemical composition, electronic structure, and physical properties of the material. It is well-documented that black phosphorus oxidizes in ambient conditions, forming various phosphorus oxides, $P_xO_y(OH)_z$.[59,127] These oxidized species include single (P-O) and double (P=O) bonds,[60] which may be dangling (P-OH, P=O) or bridging (P-O-P).[35,63,88] While more needs to be understood about the surface reactivity of black phosphorus, two possible outcomes include the development of a self-limited phosphorene oxide that protects and passivates phosphorene as well as the synthesis of a stable monolayer of phosphorene oxide[35,60,63,121,128,129]— the analogue of graphene oxide.

Water, oxygen, and light are known to play important roles in the rate, composition, and mechanism of black phosphorus oxidation,[59,60,121–123,130] but the contribution of each factor is actively debated with many studies in strong disagreement. Nearly all experiments are performed under ambient conditions, so the effects of single oxidants, O_2 or H_2O, are not well understood. Samples exposed to O_2 and H_2O simultaneously demonstrated a decrease in the ratio of the A_g^1:A_g^2 Raman active modes,[59] degradation in TEM images,[60] and the presence of phosphorus oxides on the surface of the material in XPS.[60,72,119,123] In contrast, for single component (H_2O or O_2 or light) exposures, TEM and Raman spectroscopy indicated that the material did not oxidize.[59,72,119] However, more surface sensitive techniques such as XPS show that phosphorus oxides are present with single-oxidant exposures.[72,119,123] Recent work deconvoluted experimental XPS spectra by simulating the binding energy shifts of a limited number of phosphorus oxides, and demonstrated that oxides of 2D black phosphorus exposed to ambient air or high-purity O_2 are compositionally different.[88] Despite the

advances in characterizing the composition of the oxide, the earlier study neglected low oxidation states of phosphorus and did not examine the composition of the oxide produced by only H_2O exposure. Herein, we characterize the oxide after exposure to high-purity O_2, H_2O, or both oxidants and interpret the resulting XPS spectra by simulating the binding energy shift for several oxides that have not been previously considered, including those that have low oxidation states and that may form at edges of 2D flakes.

In addition to understanding the oxide composition, the mechanism of oxidation of black phosphorus has been explored. Proposed mechanisms involve a multi-step reaction: initially photo-excited black phosphorus transfers one electron to O_2 creating superoxide,[59,127,130] a strong oxidant that then reacts with phosphorene to produce phosphorus oxides. Some of these oxides, such as phosphorus pentoxide, P_2O_5,[127,129] are strong desiccants that readily react with water to produce phosphoric acid or other acids. This model is supported by the observation of a decrease in pH during oxidation.[26] An additional mechanism to O_2-initiated oxidation is one in which H_2O may initiate the oxidization of black phosphorus. Black phosphorus exposed to deoxygenated H_2O exhibited the presence of phosphorus oxides in XPS measurements,[72,119,123] providing strong evidence that oxidation can be initiated by H_2O. With evidence for oxidation by H_2O or O_2, this work characterizes the oxidized material after exposure to O_2, H_2O, or H_2O and O_2 to understand the variations that result from different oxidant exposures. We explore the potential to oxidize defect (e.g. edge states) or non-defect (e.g. basal surface) sites of 2D black phosphorus by the different mechanisms of oxidation by H_2O and O_2.

As with graphene and graphene oxide, the potential to control the composition of the oxide of black phosphorus is a step toward chemical functionalization. Employing this tunable 2D material and its oxide requires: (1) exposing the material to high-purity oxidants, (2) spatially resolving the location and composition of the oxide, and (3) elucidating the mechanism of oxidation, ultimately providing control of the oxide formation by choice of oxidant. This work characterizes 2D black phosphorus thin films and individual flakes through photoemission spectroscopy and TEM after exposure to (i) O_2, (ii) H_2O, and (iii) mixtures of H_2O and O_2, and (iv) N_2 environments. We demonstrate an improved understanding of the resulting oxide composition through deconvolution of XPS spectra and visualization of the oxide location through time-lapsed TEM images. In addition, we find evidence for site-selective oxidation of 2D black phosphorus at defect (e.g. edge states) or non-defect (e.g. basal surface) sites by choice of oxidant and provide a possible mechanism for the oxidation of phosphorene by H_2O.

3.2 Experimental Section

3.2.1 Material Preparation

Bulk black phosphorus crystals were synthesized by an Sn and SnI4 vapor transport method.[26,67] Under an inert atmosphere ($O_2 < 1$ ppm, $H_2O < 0.1$ ppm), we then prepared 2D black phosphorus (Figure 3.1a-b) by liquid exfoliation of bulk crystals in anhydrous N-methyl-2-pyrrolidone (NMP). Centrifugation of the resulting suspension yielded flakes ranging from 1-7 layers with a median of bilayers (Figure 3.1c-d).[26] The diffraction pattern (Figure 3.1b) of the thinnest region of the flake (Figure 3.1a) is consistent with a monolayer of black phosphorus.[131] Under an inert atmosphere, we re-dispersed the 2D material in isopropanol and deposited flakes onto lacey carbon TEM grids by drop casting (Figure 3.1a). We prepared thin films of 2D black phosphorus on hydrophilic gold-plated silicon wafers using the doctor blade technique under an inert atmosphere.[132] A scanning electron microscope (SEM) image of the topology of the 2D black phosphorus film is shown in Figure 3.1e.

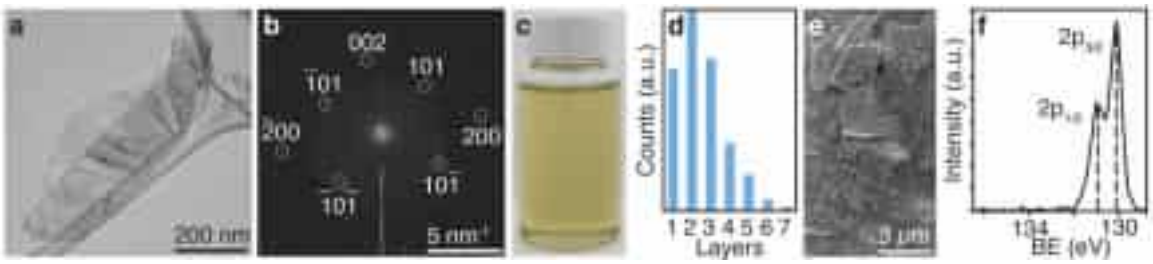


Figure 3.1: Liquid exfoliation of black phosphorus and characterization of thin films. (a) TEM image of an unoxidized 2D black phosphorus flake. (b) The diffraction pattern of the thinner region is consistent with a monolayer of phosphorene. (c) A centrifuged solution of 2D black phosphorus suspended in NMP. (d) The thickness distribution of the 2D suspension ranges from 1 to 7 layers. (e) SEM image showing the topology of a doctor bladed thin film of 2D black phosphorus. (f) The XPS spectra of the phosphorus 2p core electrons of an unoxidized 2D black phosphorus film: the photoemission peaks, $2p_{3/2}$ and $2p_{1/2}$, are centered at 130.1 eV and 131.0 eV, respectively.

3.2.2 Oxidant Exposure

The 2D black phosphorus thin film assemblies and individual flakes were exposed to (i) O_2, (ii) H_2O/N_2, (iii) mixtures of H_2O/O_2, or (iv) maintained under inert atmosphere, N_2. Research grade (i) O_2 (99.999% purity) flowed over a P_2O_5 desiccant prior to reaching the phosphorus sample, ensuring an environment devoid of H_2O. To create (ii) H_2O/N_2 or (iii) H_2O/O_2 oxidants, distilled H_2O was heated to 100°C and

purged with (ii) N_2 (99.998%) or (iii) O_2 for at least 30 minutes; carrier gases of (ii) N_2 or (iii) O_2 were used to flow water vapor over the sample. The thin films (containing < 0.01 micromoles of P) and individual flakes on TEM grids were exposed to oxidant gas flow for 5 minutes, sealed with 5 millimoles of oxidant species—a significant excess of oxidant compared to the phosphorus. In each of these exposures, the oxidants equilibrated to room temperature upon reaching the sample. Then, each sample was illuminated by a 460 nm LED with an intensity of 0.6 mW/cm2 at room temperature ($\sim$25°C). After 1, 6, or 18 hours, the sample was removed from illumination, placed under vacuum, and stored under an inert atmosphere.

3.2.3 Characterization

Samples were maintained under an inert atmosphere during transport and loading procedures, unless otherwise stated. Resulting oxides of the thin films were characterized by XPS using a Kratos Axis Ultra Delay-Line Detector (DLD) spectrometer with monochromatic Al Kα source. Individual flakes were imaged using a low-resolution JEOL 100CX II TEM at an accelerating voltage of 80 kV. Thin films were imaged using a Hitachi S-4700 Cold Cathode Field Emission SEM at an accelerating voltage of 2 kV.

3.3 Results & Discussion

3.3.1 XPS Characterization

We used XPS to investigate the core electron binding energies of phosphorus 2p electrons. Unoxidized 2D black phosphorus films (Figure 3.1f) exhibit $2p_{3/2}$ and $2p_{1/2}$ peaks at 130.1 eV and 131.0 eV, respectively; these values are in good agreement with known bulk black phosphorus 2p peak positions.[63,133–135] Additionally, 2D black phosphorus thin films exposed to a single oxidant, O_2 (Figure 3.2a) or H_2O/N_2 (Figure 3.2b), or two oxidants, H_2O/O_2 (Figure 3.2c), have the same 2p doublet peaks at 130.1 eV and 131.0 eV, confirming that most phosphorus remains unoxidized.

The presence of electronegative groups, such as oxygen or hydroxide, on the surface withdraw charge from black phosphorus, leading to more tightly bound phosphorus electrons. As a result, phosphorus oxide species experience higher phosphorus 2p core electron binding energies, E_B^F, than unoxidized material. Our previous calculations showed that 2D black phosphorus oxides with phosphorus oxidation states of +2, +3, or +5 have binding energies in the range of 132 to 136 eV.[88] The photo-emitted 2p core electrons of oxidized 2D black phosphorus films (Figure 3.2) have a broad phosphorus oxide peak from 132 to 136 eV. As exposure

time of the 2D film increased, the relative quantity of phosphorus oxides increased—indicated by the growth of the oxide peak relative to the black phosphorus doublet (Figure 3.2). Additionally, the peak maximum simultaneously shifted to higher binding energies, indicating a change in the composition of phosphorus oxides.

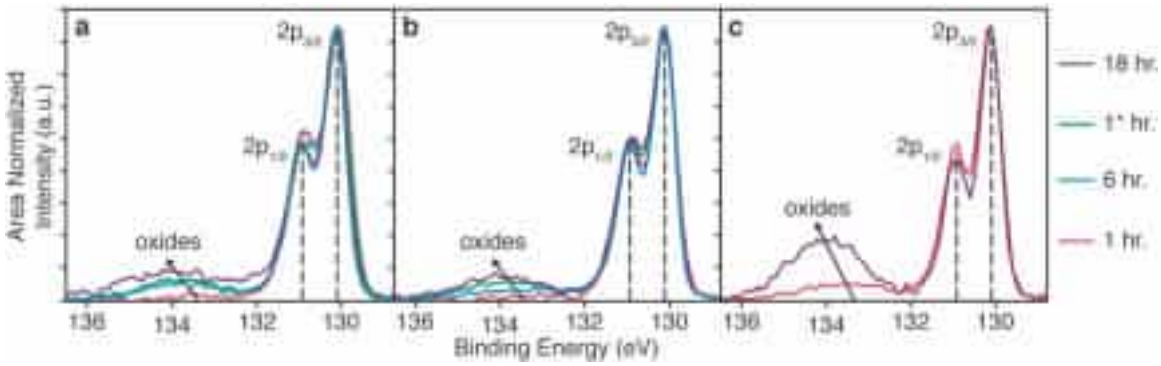


Figure 3.2: XPS spectra of 2D black phosphorus films exposed to various oxidants in the gas phase: (a) O_2 (99.999%), (b) H_2O/N_2 (99.998%), (c) H_2O/O_2. As the time of exposure increased, the quantity of phosphorus oxides increased, shown by the arrows. The red/blue/purple lines indicate 1/6/18 hours of oxidant exposure, respectively. The green line, 1*, represents series-exposed oxidation, in which a sample was exposed to a single oxidant for 5 minutes, evacuated, and then exposed to the other oxidant for 1 hour: (a) H_2O/N_2, then O_2 and (b) O_2, then H_2O/N_2. The 6 hour exposures for H_2O/O_2 oxidants were contaminated and are therefore not shown.

The oxidation of few-layer phosphorene by a single oxidant, O_2 (Figure 3.2a) or H_2O/N_2 (Figure 3.2b), is slower than oxidation by two oxidants, H_2O/O_2 (Figure 3.2c). The accelerated rate of oxidation in the presence of two oxidants may indicate a multi-step or catalyzed mechanism. To explore these possibilities, we exposed 2D black phosphorus films to a series of gases: (i) H_2O/N_2, then O_2 or (ii) O_2, then H_2O/N_2. Herein, we refer to these as series-exposed (i) O_2 or (ii) H_2O samples, respectively. In each of these cases, the first exposure to a single oxidant lasted 5 minutes and was performed in dark conditions, evacuated for 45 minutes, resealed under N_2, and then exposed to the other oxidant and illuminated for 1 hour. Each series-exposed sample formed more oxide than the respective single oxidant sample (Table 2.2). This suggests that trace quantities of residual O_2, H_2O, or reaction byproducts accelerate or catalyze oxidation. Since the residual content of H_2O or O_2 was far less than the amount of oxidized material, we conclude that the reaction byproducts rather than the initial oxidants are primarily responsible for the increased rate of oxidation. This observation is consistent with a mechanism in which the oxide makes the material far more susceptible to

oxidation, possibly by a catalytic process. This observation also highlights the difficulty of designing a self-passivating oxide on phosphorene.

3.3.2 Time-lapsed TEM

In order to understand where oxidation was occurring, we conducted a time-lapsed TEM study of individual flakes to visualize physical modifications after exposure to O_2 (99.999%), H_2O/N_2 (99.998%), or ambient conditions. To verify that observed changes were not attributed solely to knock-on damage from the TEM, we imaged a new flake at each time interval, in addition to imaging all previously-viewed flakes. A representative unoxidized 2D black phosphorus flake is shown in Figure 3.3a. The same flake was then exposed to high-purity O_2 (99.999%) for 1, 6, and 18 cumulative hours, shown in Figure 3.3b-d, respectively. Small changes in diffraction contrast are apparent in these images, which are a consequence of small changes in the tilt of the sample with respect to the electron beam. No other changes, such as etching, bubble formation, or any other large changes in contrast, in O_2-exposed flakes were observed. The absence of these changes as the phosphorus oxide formed (Figure 3.2a) indicates that the oxide layer must be relatively uniform across the basal (i.e. van der Waals) surface of phosphorene, because an inhomogeneous oxide would give rise to considerable mass contrast in our thin 2D phosphorus samples. Thus, we find that exposure to high purity oxygen produces a relatively uniform oxide on the van der Waals surface, and could also lead to novel materials, such as a 2D phosphorene oxide.

For flakes exposed to H_2O/N_2 (99.998%), pitting on the thicker side of steps was observed, as shown in Figure 3.3e. In Sec. 3.5, we examine the mechanism of this observed oxidation. As exposure to H_2O continued, etching at edges and steps was also observed, demonstrated for a step in Figure 3.3f (unoxidized) and Figure 3.3g (18 hrs. in H_2O/N_2). These observations imply that photo-excited 2D black phosphorus can be oxidized by H_2O, validating previous experimental observations.[72,117,119] Our TEM images suggest a mechanism in which water preferentially oxidizes defect sites, especially those at edges and steps.



Figure 3.3: TEM images of 2D black phosphorus exposed to different oxidants. (a) An unoxidized 2D black phosphorus flake, where steps are indicated by dashed lines, was exposed to O_2 (99.999%) for (b) 1, (c) 6, and (d) 18 hours. (e) A flake exposed to H_2O/N_2 (99.998%) demonstrated pitting at the thicker side of a step after 6 hours. (f) An unoxidized black phosphorus flake with the step indicated with a dash-dot line; (g) after exposure to H_2O/N_2 (99.998%) for 18 hours, the step exhibited a loss of material, represented by the highlighted orange region adjacent to the original edge (dash-dot line). (h) After extended exposure to ambient conditions (76 hours), pitting at the thicker side of steps occurred and extended farther into the thicker sides of the flake. Each scale bar is 100 nm. Insets are a lower magnification of the flake shown in the respective image; each inset scale bar is 200 nm.

Samples exposed to ambient conditions (Figure 3.3h) showed the same pitting at steps as observed in H_2O/N_2 environments. We found 94% of flakes exposed to ambient conditions demonstrated pitting for exposure times spanning 1 to 100 hours with a confidence interval of 90 to 100% (Table 3.1). For longer exposure times, pit diameters increased in width, especially in thicker regions of the material (see Figure 3.3h). We refer to this mechanism of oxidation as surface pitting and it was observed in 75% of flakes imaged at consecutive time intervals. Furthermore, loss of material at edges was observed in 62% of flakes consecutively imaged after ambient exposure. For longer exposures, the combination of pitting at steps, loss of edges, and surface pitting can ultimately result in loss of an entire layer of a 2D flake. Table 3.1 summarizes these results.

Table 3.1: Observed oxidation mechanisms in ambient conditions for 1—100 hours

	Mean (%)	Confidence Interval (%)	Sample Size
Pitting at steps	94	90–100	77
Loss of edges	62	54–68	37
Surface pitting	75	65–78	58
Loss of layer(s)	56	50–67	36

Our experiments demonstrate that the mechanism of oxidation of 2D black phosphorus depends on the oxidant; high-purity O_2 leads to an oxide layer on the basal surface of 2D phosphorus, while H_2O causes physical degradation of the material through pitting on the thicker sides of steps and material loss at edges. Recently, s-SNOM was used to characterize the degradation mechanism of mechanically exfoliated bulk black phosphorus and 1 nm Al2O3-encapsulated 2D black phosphorus in air; oxidation began at edges, steps, and surface defects,[121] suggesting a similar mechanism of degradation for ambient-exposed liquid and mechanically exfoliated samples.

3.3.3 Binding energy shift, ΔE_B^F, of Phosphorus Oxides

The ability to characterize the basal surface and edge oxides resulting from high-purity O_2 or H_2O oxidation would provide information about the surface chemistry of 2D black phosphorus. Previous work simulated the XPS binding energy for basal surface and molecular oxides in the +2, +3, and +5 oxidation states.[88] With our new evidence for oxidation at the edge of flakes and the possibility of forming phosphorus in a +1 oxidation state, more simulations are needed to comprehensively characterize the phosphorus oxides from XPS spectra.

A convenient way to calculate the core-level binding energy ΔE_B^F between inequivalent sites in the sample involves a thermodynamic Born-Haber cycle, which subdivides the transition from the initial ground state to the fully screened final state of the solid system into steps involving either ground-state processes such as desorption or adsorption of specific atoms from the solid, or photo-excitation and de-excitation processes in isolated atoms (Figure 3.4). A core assumption is the ”equivalent cores” or ”Z+1” approximation,[89] which considers—for the duration of the photoemission process—a phosphorus atom with a missing core electron to be equivalent to a sulfur atom with an extra proton (“Z+1”) in the nucleus and a missing valence electron. In the fully screened final state, the valence-ionized sulfur atom turns neutral by acquiring an additional valence electron. Thus, the photoemission and screening segments of the Born-Haber cycle involve isolated atoms

only and drop out in the difference of core-level binding energies (Figure 3.4b). The Born-Haber cycle is depicted in Figure 3.4a and details of the Born-Haber cycle as applied to oxidizing phosphorene are provided in Ref. 86.

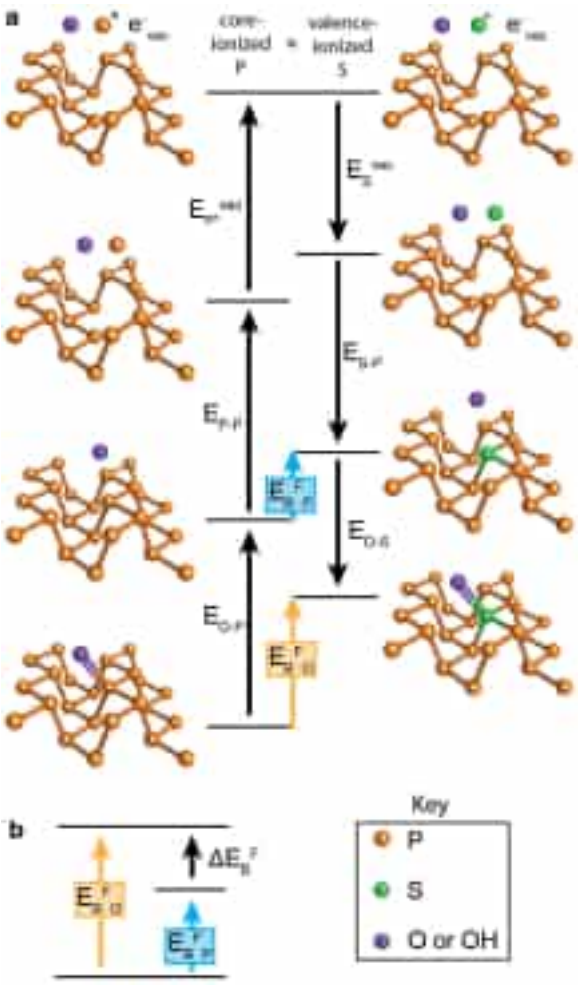


Figure 3.4: Depiction of the thermodynamic Born-Haber cycle for oxidized phosphorene. (a) The thermodynamic Born-Haber cycle allows the core-electron binding energy of unoxidized (E^F_{BP}) and oxidized (E^F_{BO}) phosphorene to be calculated. For unoxidized material, the energy of cohesion (E_{P-P}) of the phosphorus atom is calculated. Then, a core-electron is photo-excited to the vacuum level (E^{vac}_{P*}). The core-ionized phosphorus atom (P*) is approximated to be an equivalent valence-ionized sulfur atom (S^+). As the sulfur ion recombines, the energy released is the calculated ionization energy (E^{vac}_S). Finally, the sulfur is returned to the original phosphorus atom's site, releasing the energy of cohesion (E_{S-P}). The difference between the initial and final states is equivalent to the core-electron binding energy of a phosphorus atom in unoxidized phosphorene (E^F_{BP}). Two additional steps are added to the start and end of the cycle for an oxidized phosphorus atom: the energy required to desorb the oxide species from the phosphorus atom (E_{O-P}) and the energy released when the oxide species adsorbs to the sulfur atom (E_{O-S}). The difference between the initial and final states of this cycle is equivalent to the core-electron binding energy of a phosphorus atom in oxidized phosphorene (E^F_{BO}). (b) The difference in energy between these two processes allows for the core-electron binding energy shift (ΔE^F_B) to be calculated.

The usefulness of this approach has been demonstrated previously.[85–88] In the present case, calculation of a particular phosphorus core-level binding-energy shift ΔE_B^F at a specific site involves the total-energy calculation of an unoxidized or oxidized phosphorene monolayer and of the corresponding system, where the phosphorus atom of interest has been substituted by a sulfur atom (Figure 3.4).[88] Precise differences between these total energies can be obtained using *ab initio* DFT calculations that consider valence electrons only.

The total energy calculations of structures, which are needed to determine specific core-level binding-energy shifts ΔE_B^F have been performed using DFT with a plane-wave basis, similar to our previous study.[88] We used projector augmented wave (PAW) pseudopotentials[82] as implemented in the VASP code.[83] Electronic exchange and correlation have been described by the Perdew-Burke-Ernzerhof (PBE)[84] functional with a 500 eV cutoff energy. A k-mesh of 9×9×1 k-points and 5×5×1 k-points were used for a black phosphorus unit cell and 2×3 supercell, respectively. Through self-consistent iterations, a total convergence of better than 1 meV/atom was achieved. For each phosphorus oxide species simulated, we first relaxed the structure and optimized the geometry. Additionally, we performed Bader population analysis,[136] calculating the net charge of the oxidized phosphorus atom. Unoxidized and related oxidized phosphorene monolayers have been represented using the same approach as in the previous study, which surveyed 2D black phosphorus oxides of the basal surface and oxidic fragments with oxidation states of +2, +3, and +5.[88] Here, we extend the previous DFT survey to comprehensively include lower oxidation states (+1, +2) as well as oxides that can form at the edges and steps of 2D flakes, such as those shown in Figure 3.5a-e. In DFT calculations, edge structures that have been passivated by hydroxyl or peroxy acid groups have been represented by a periodic array of ribbons separated by a vacuum region of $\gtrsim$15 Å.

We observed a correlation between Bader charge and ΔE_B^F of oxidized phosphorus atoms, shown in Figure 3.5f. As the Bader charge of the phosphorus atom increased, the core electron binding energy shift increased, in agreement with previous work.[88] This correlation allowed for the division of oxide species into 5 groups, depicted in Figure 3.5f-g, based on oxidation state and ΔE_B^F: (i) +1 with 3 bonds, 0.90—1.16 eV (Figure 3.5a,c,e), (ii) +2 with 5 bonds, 1.40 eV (Figure 3.5b), (iii) +3 with 5 bonds, 1.98—3.10 eV (Figure 3.5c,d), (iv) +3 with 3 bonds, 3.48—4.01 eV, (v) +5 with 5 bonds, 4.73—5.97 eV. Within the same group, we found that edge oxides have similar binding energy shifts as basal surface oxides. For example, the basal oxide shown in Figure 3.5a has a similar binding energy shift as the edge oxide shown in Figure 3.5d. Thus, XPS cannot distinguish between edge and basal surface oxides.

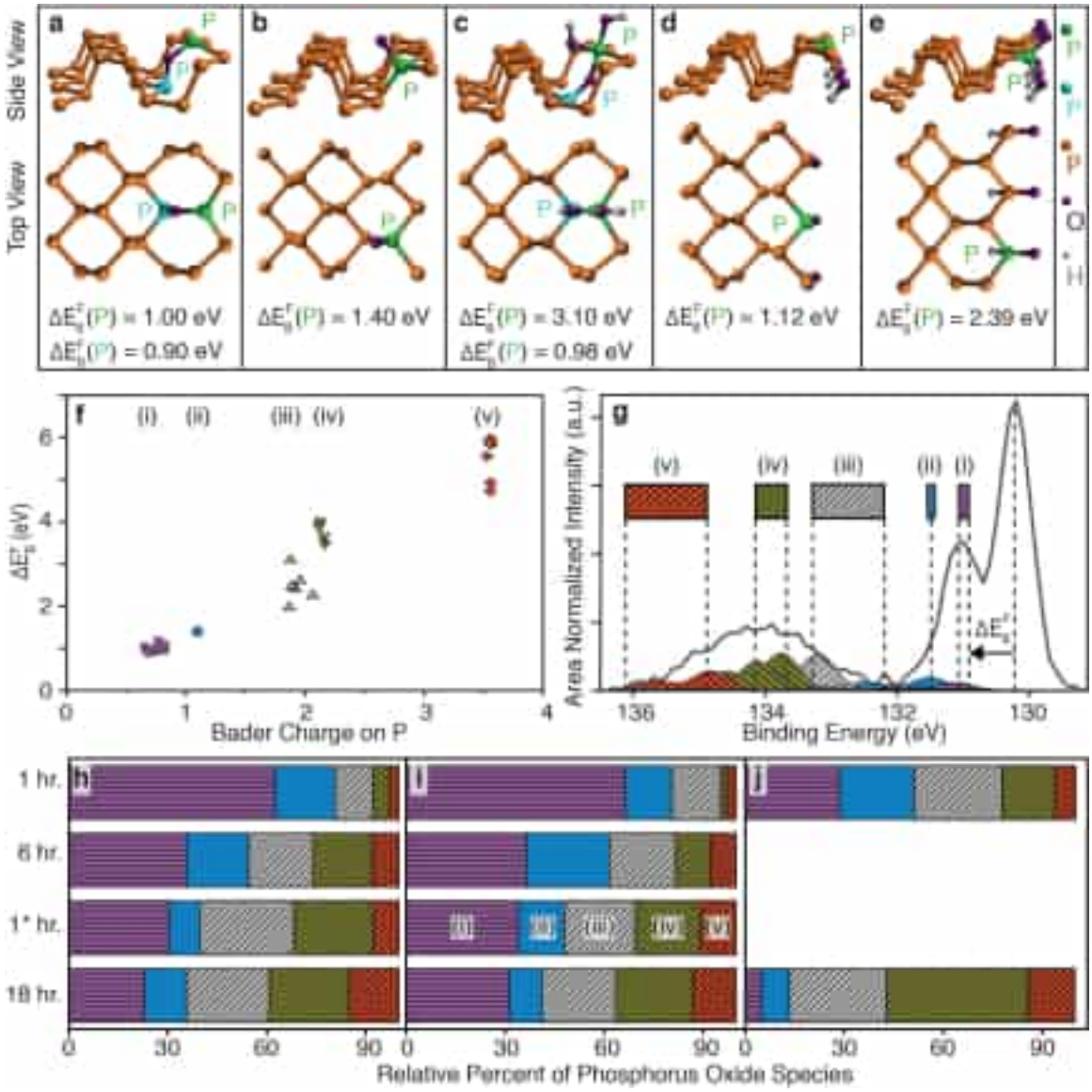


Figure 3.5: Deconvolution of XPS spectra of oxidized phosphorene. (a-e) Ball and stick figures of oxidized black phosphorus structures are shown from the side and top views. (a-c) Surface phosphorus oxides from groups (i), (ii), and (iii) are shown. (d-e) Edge oxidized species from group (i) and (iii) are displayed. ΔE_B^F is shown below each species. (f) Correlation between ΔE_B^F and Bader charge for the 24 calculated structures. The oxide species are easily divided into five groups. (g) Using our five groups, we deconvolute the spectrum of phosphorene exposed to H_2O/O_2 for 18 hours. The deconvoluted doublets have the same FWHM as the parent unoxidized material. (h-j) Percentages of the five classes of oxide species produced from (h) O_2, (i) H_2O/N_2, and (j) H_2O/O_2 after 1, 6, and18 hours. The series-exposed samples are also shown, indicated by the 1* hr. As noted in (i), group (i) is purple, group (ii) is blue, group (iii) is grey, group (iv) is green, and group (v) is orange. The 6 hour exposures for H_2O/O_2 oxidants were contaminated and are therefore not shown.

3.3.4 Deconvolution of XPS Spectra

Using the calculated ΔE_B^F for each oxide, we deconvoluted the experimental spectra from Figure 3.2 using the same method employed in previous literature.[88] To do this, we fit the unoxidized 2D black phosphorus 2p peaks at 130.1 and 131.0 eV and identified the FWHM. We iteratively fit peaks for each oxide group until the cumulative fit converged with a chi-squared tolerance of 10^{-12}. The deconvolution of the 18-hour H_2O/O_2 exposure is shown as an example in Figure 3.5g. In all of our spectra, we did not observe a binding energy shift corresponding to group (v) small molecules, such as H_3PO_4. These molecules have a larger binding energy shift than other group (v) oxides. We suspect that these small molecules were produced but, most likely, these small molecules were removed in the high vacuum conditions (10^{-9} torr) of the XPS instrument.

We calculated the relative abundance of each group of oxide species. Histograms depicting the percent of each oxide group after exposure to oxidants O_2, H_2O/N_2, or H_2O/O_2 are depicted in Figure 3.5h-j, respectively. As exposure time increased, the relative amount of species with low oxidation states decreased while higher oxidation states increased. Moreover, the series-exposed samples, such as the sample oxidized by H_2O/N_2 for 5 minutes and then O_2 for 1 hour represented by the 1* hr. in Figure 3.5h, show more highly oxidized species than exposure to a single-oxidant, such as oxidation by O_2 for 6 hours in Figure 3.5h. These findings are consistent with an oxidation that is catalyzed by the presence of reaction byproducts.

3.3.5 Mechanism of Oxidation by O_2 or H_2O

To understand the mechanisms of basal surface oxidation by O_2 and defect-mediated oxidation by H_2O, we compared the band structure of 2D black phosphorus (Figure 3.6a)[23,26,137,138] and the reduction potentials of likely redox couples (Table 3.2, Figure 3.6a).[98,139–145] As shown in Figure 3.6a, the band gap of the 2D black phosphorus decreases with increasing thickness.[23,137,138] We only consider one-electron transfer from the conduction band and one-hole transfer from the valence band because the illumination intensities in our experiments produce fewer than one photo-excited electron/hole per phosphorene flake at steady state on average. Prior work suggested that a photo-excited electron can be transferred from the conduction band of black phosphorus to O_2, producing the superoxide radical $O_2^{\cdot-}$ as demonstrated in Equation 3.1.[59]

$$O_2 + e_{CB}^- \rightarrow O_2^{\cdot-} \tag{3.1}$$

Based on the reduction potential for forming superoxide (Figure 3.6a, Table 3.2 for neutral and acidic pHs), the proposed one-electron transfer from the conduction band of black phosphorus to oxygen is plausible. The superoxide then reacts with oxidized phosphorene, producing a phosphorus oxide (Figure 3.6b). This model is consistent with XPS observations (Figure 3.2a) which showed the formation of phosphorus oxides across the basal surface of phosphorene, as inferred from TEM images (Figure 3.3a-d).

To understand how H_2O oxidizes 2D black phosphorus, we considered the possibility of a photo-excited hole transfer from the 2D material to H_2O, such as Equation 3.2. Based on the reduction

$$H_2O + h^+_{VB} \rightarrow OH^{\cdot} + H^+ \tag{3.2}$$

potential for forming a radical hydroxide and proton relative to the valence band of bulk and 2D black phosphorus (Table 3.2, Figure 3.6a), it is not thermodynamically favorable for this reaction to occur. Likewise, there is no thermodynamically favorable one-electron transfer from the conduction band to H_2O. We conclude that the first step in the reaction of 2D black phosphorus with H_2O is not an electron or hole transfer.

Table 3.2: Absolute reduction potentials E_{abs} at 25°C

Couple	pH 7	pH
$O_2 + e^- \rightarrow O_2^{\cdot -}$ [136–139]	-4.51 ± 0.02 V	-4.09 ± 0.02 V
$OH^{\cdot} + H^+ + e^- \rightarrow H_2O$	-6.75 ± 0.02 V	7.16 ± 0.02 V

An important observation about the mechanism of water-phosphorene reactions is that the reactions occur at steps, edges, and grain boundaries (Figure 3.3e,g). At these defect sites, atoms are likely to have relatively unstable bonding configurations, such as a phosphorus atom with just two bonds (Figure 3.6b). Therefore, at these defect sites, a direct chemical reaction with H_2O must be thermodynamically favored. The observation that pitting occurs at a step (Figure 3.3e) or edge (Figure 3.3g) is consistent with the need for a defect state to initiate oxidation. Furthermore, due to the relative positions of the reduced band gap with increasing thickness, photo-excited electron-hole pairs preferentially move to thicker regions of the flake. Therefore, it can be inferred that oxidation occurs at a higher rate on the thicker side of the flake. The observed pitting of thicker regions at defect sites of steps is consistent with this proposed mechanism and supports first-principles calculations that H_2O cannot lead to the oxidation of pristine, defect-free material on the basal surface.[130] Our experimental observations suggest that the reaction with H_2O at a defect site does not result in a self-passivating barrier to further reaction: the continued etching of phosphorene flakes

over time indicates that the oxide that forms at defects is relatively unstable. Additionally, it is important to highlight that oxidation by H_2O at defect sites supports our observations of accelerated oxidation in samples exposed to both oxygen and water. When the pristine basal surface of the material reacts with O_2, numerous defect sites are created. The increased concentration of defect sites leads to a faster reaction with water. This experimental observation validates first-principle studies of the susceptibility of the basal oxide to further hydrolysis.[130]

These insights provide a pathway to oxidize the basal surface with O_2 or the defect sites with H_2O. This may lead to improved control over the properties of phosphorene as well as new routes to stabilize the material against oxidation. We emphasize that these insights were made possible only through the use of high purity O_2 and H_2O.

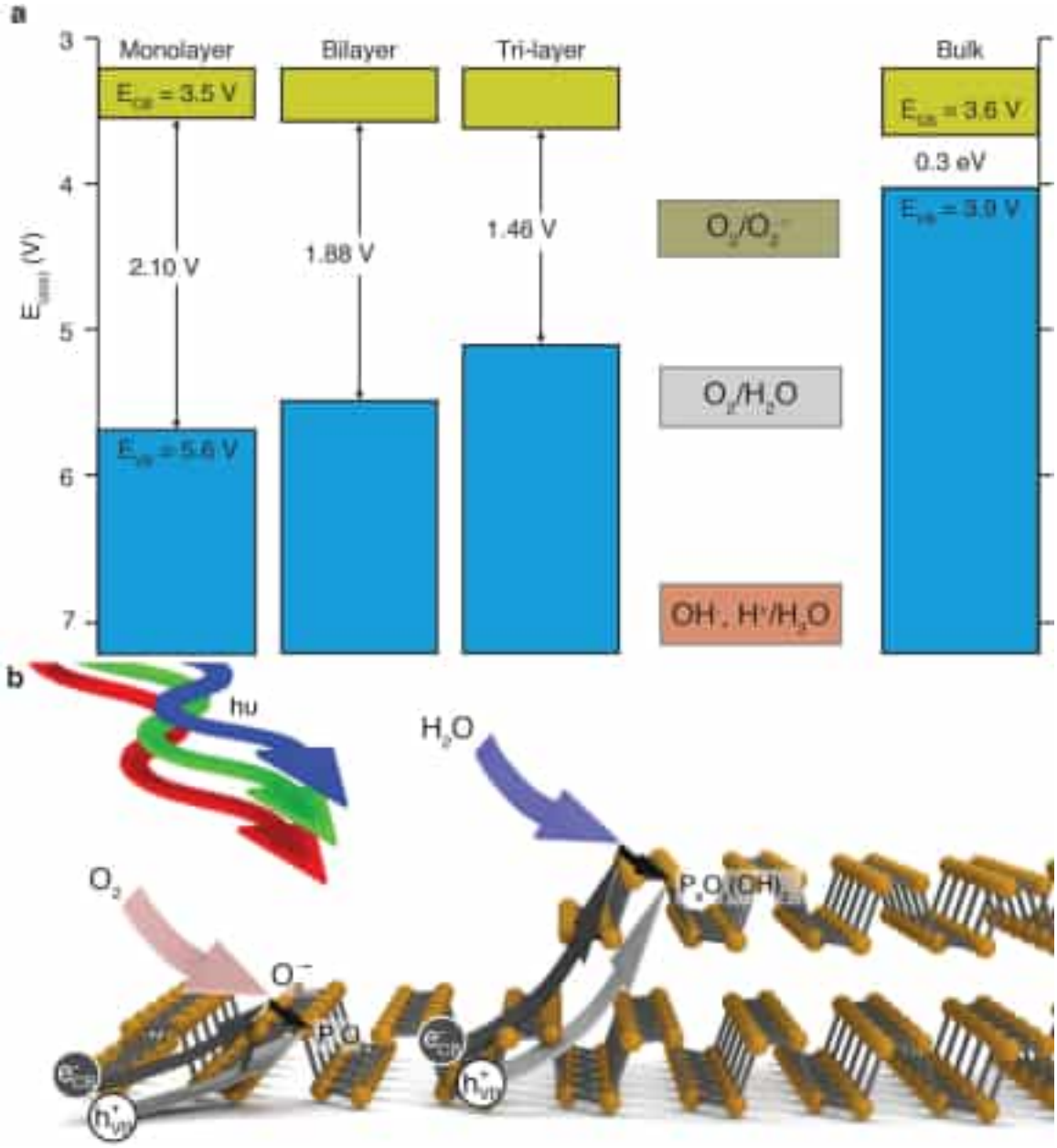


Figure 3.6: Oxidation mechanism of 2D black phosphorus flakes. (a) The band diagram for thicknesses of 1, 2, 3-layers and bulk black phosphorus is depicted. The absolute reduction potentials for $O_2/O_2^{\cdot-}$ and $OH^{\cdot}$, H^+/H_2O at 25°C for acidic to neutral pH values (Table 3.2) are shown. (b) A graphical depiction of the oxidation of 2D black phosphorus by O_2 or H_2O. Photo-excitation of the material produces an electron-hole pair; the electron e^-_{CB} and hole h^+_{VB} preferentially move to the thicker region of the 2D material. Oxidation by H_2O occurs at defect sites, preferentially on thicker regions of a flake. Oxidation by O_2 occurs on the basal surface of 2D black phosphorus, via a one-electron transfer to O_2.

3.4 Conclusion

In this work, we studied the oxidation of thin films and individual flakes of 2D black phosphorus exposed to high-purity O_2, H_2O, and their mixtures. We found that both H_2O and O_2 can oxidize the 2D material. For high-purity, dry O_2 environments, XPS showed the material oxidizes, but we did not observe any changes in the shape or integrity of 2D flakes in TEM images. We observed primarily the presence of low oxidation state species (+1, +2) in short-term exposures to O_2. By investigating the band structure of black phosphorus and the reduction potentials of $O_2/O_2^{\cdot}$, it was easily seen that black phosphorus can be oxidized by O_2. This supports a model in which high-purity O_2 environments lead to oxidation of the van der Waals surface of 2D black phosphorus.

In contrast, oxidation of 2D black phosphorus by H_2O physically degraded the material. Initially, the material exhibited pitting at steps on the thicker side of the flake, which then migrated farther into the thicker region of the flake as exposure to H_2O continued, ultimately resulting in surface pitting. Additionally, edges of the material were corroded during oxidation by H_2O. With continued oxidation, these degradation processes resulted in the loss of layers. The band structure of black phosphorus and the reduction potential of $OH^{\cdot}$, H^+/H_2O provides more insight into the mechanism of oxidation. It is thermodynamically unfavorable for black phosphorus to be oxidized by H_2O. With evidence of oxidation in XPS and TEM, this supports a model in which H_2O reacts preferentially with defect sites, such as those at steps and edges.

Finally, we found that 2D black phosphorus degrades most rapidly in the environments containing both H_2O and O_2, exhibiting a greater abundance of phosphorus in higher oxidation states (+3, +5). From our series-exposed samples, we determined that residual quantities of oxide byproducts accelerate or catalyze the oxidation of the material. Furthermore, the physical degradation of the material after exposure to ambient conditions was the same as in H_2O-only environments. We conclude that H_2O or reaction byproducts from H_2O oxidation catalyze oxidation by O_2.

The use of high purity O_2 or H_2O provides control of the phosphorus oxide composition and site selectivity for oxide formation. This knowledge is a step forward in surface reaction chemistries of 2D black phosphorus. Controlled oxidation of 2D black phosphorus opens pathways to selectively oxidize basal surface and edge sites of the material, opening pathways for site-selective surface functionalization. Additionally, this work may provide an avenue to synthesize 2D phosphorene oxide, but more work is needed to understand if the oxide is self-limited.

TUNING THE PLASMON RESONANCE OF FEW-LAYER GRAPHENE ANTI-DOT ARRAYS

4.1 Introduction

Due to the numerous techniques to pattern graphene with nanometer dimensions[13,47,50,146,147] in conjunction with its high mobility[14–16], graphene is a superb plasmonic material. Exploiting these aspects, while being limited by its low carrier concentration,[1,44] graphene has demonstrated plasmons in the THz[45,46] and mid-infrared (MIR)[47–51] regimes thus far. While it has been used as a plasmonic material primarily at wavenumbers $\lessapprox 2000$ cm^{-1} ($\lessapprox 0.25$eV, $\gtrapprox 5000$ nm), if its plasmons could be engineered to occur in the near-infrared (NIR) or even visible spectra, many new areas of application could emerge. These include sensing (e.g., molecular vibrations in the range of 2000–5000 cm^{-1}),[148] solar-to-electrical or solar-to-chemical energy conversion ($\lessapprox 2500$ nm, $\gtrapprox 4000$ cm^{-1}),[149] and telecommunications (1200–1600 nm, ~ 7000 cm^{-1}).[13] Most commonly, graphene plasmons have been tuned by altering the carrier concentration through electrostatic[47,49,52] or chemical doping[25,53,54] or reducing the dimensions[13]. Here, we combine these strategies in simulations to explore the extent to which the plasmon frequency of monolayer and few-layer graphene (FLG) can be altered.

4.2 Background

Metals with high carrier concentrations, such as gold and silver with $\sim 6 \cdot 10^{22}$ cm^3,[42] have demonstrated plasmons in the visible spectrum.[43] However, these high carrier concentrations limit the ability to shift the plasmonic response by doping.[43] Only select techniques, such as changing the surrounding dielectric medium,[150] have shifted the plasmonic response from the visible and into the NIR. In contrast to these metals, graphene is a 2D semimetal with a low carrier concentration of $\sim 2 \cdot 10^{19}$—$1 \cdot 10^{20}$ cm^{-3}.[1,44] Electrical gating of graphene allows for the carrier concentration to be electrostatically doped at ~ 0.001—0.01 carriers/atom and the concentration attains values on the order of $3 \cdot 10^{19}$—$3 \cdot 10^{20}$ cm^{-3}.[43] In electrostatic doping, the extent to which the concentration of the charge carriers can be altered is limited by the Dirac cone in the

band structure, restricting the Fermi energy level E_F shifts to < 1 eV.[52,151] Since E_F scales linearly with the plasmon resonance, the plasmon resonance can effectively only be shifted by < 1 eV, which limits its application to the MIR region of the electromagnetic spectrum. However, chemical doping provides an attractive pathway to increase the carrier concentration of FLG by several orders of magnitude, reaching values comparable to gold $\sim 1 \cdot 10^{22}$ cm^{-3} in stage I KC_8, Figure 1.5).[1]

Thus, we might expect patterned doped-graphene to be a plasmonic material with responses spanning the THz to MIR to NIR to visible spectra (Figure 1.5). Here, we investigate the plasmonic response of mono- and FLG arrays with these carrier concentrations.

The second common approach to tuning the plasmonic response of graphene is to reduce dimensions of the material. Plasmons have been demonstrated in dot,[46,47,50] ring,[47] ribbon,[45,49,51] and tapered[152,153] structures in the THz (2700 cm^{-1}, 0.34 eV, 3.7 μm) and MIR regions.[47] Interestingly, molecular species of polycyclic aromatic hydrocarbons, which are similar to graphene, exhibit plasmons in the NIR and visible spectra, by restricting dimensions to a finite number of atoms.[154] This phenomenon further supports the idea that the plasmon of graphene should be tunable from the THz to the visible spectra, by constraining the geometry of the graphene arrays. A key challenge to designing these broadly tunable arrays is to synthesize FLG with long plasmon lifetimes. Currently, lithographic and etching techniques[13,47,50,146] introduce a large number of edge sites and reduce the carrier mobility,[13] effectively shortening the lifetime of a plasmon. We propose that a method to address these limitations is to synthesize hole (e.g. anti-dot) arrays, since the number of edge sites is less relative to the surface area of the material. The plasmonic activity of a holey structure has been demonstrated for rod-shaped nanoresonators,[146] however, it has yet to be applied to more hole shapes. Here, we investigate hexagonal anti-dot lattices and structure parameters to shift the plasmon frequency.

4.3 Experimental Methods

We employ a finite-difference time-domain suite (FDTD Solutions in Lumerical, Inc.) to simulate the optical properties and plasmonic response of mono- and FLG anti-dot structures. These structures are described by diameter D, periodicity P, and edge-to-edge E parameters (Figure 4.1a) with a thickness of one to six layers. In the simulation environment, the doped-material is placed on a 20 nm dielectric layer, similar to ITO, on top of a substrate. For THz and MIR simulations, the substrate is a silicon wafer with a

285 nm thermal oxide (Figure 4.1b), while for visible and NIR spectra, the substrate is SiO_2 (Figure 4.1c). Each substrate material is modeled with a constant refractive index.

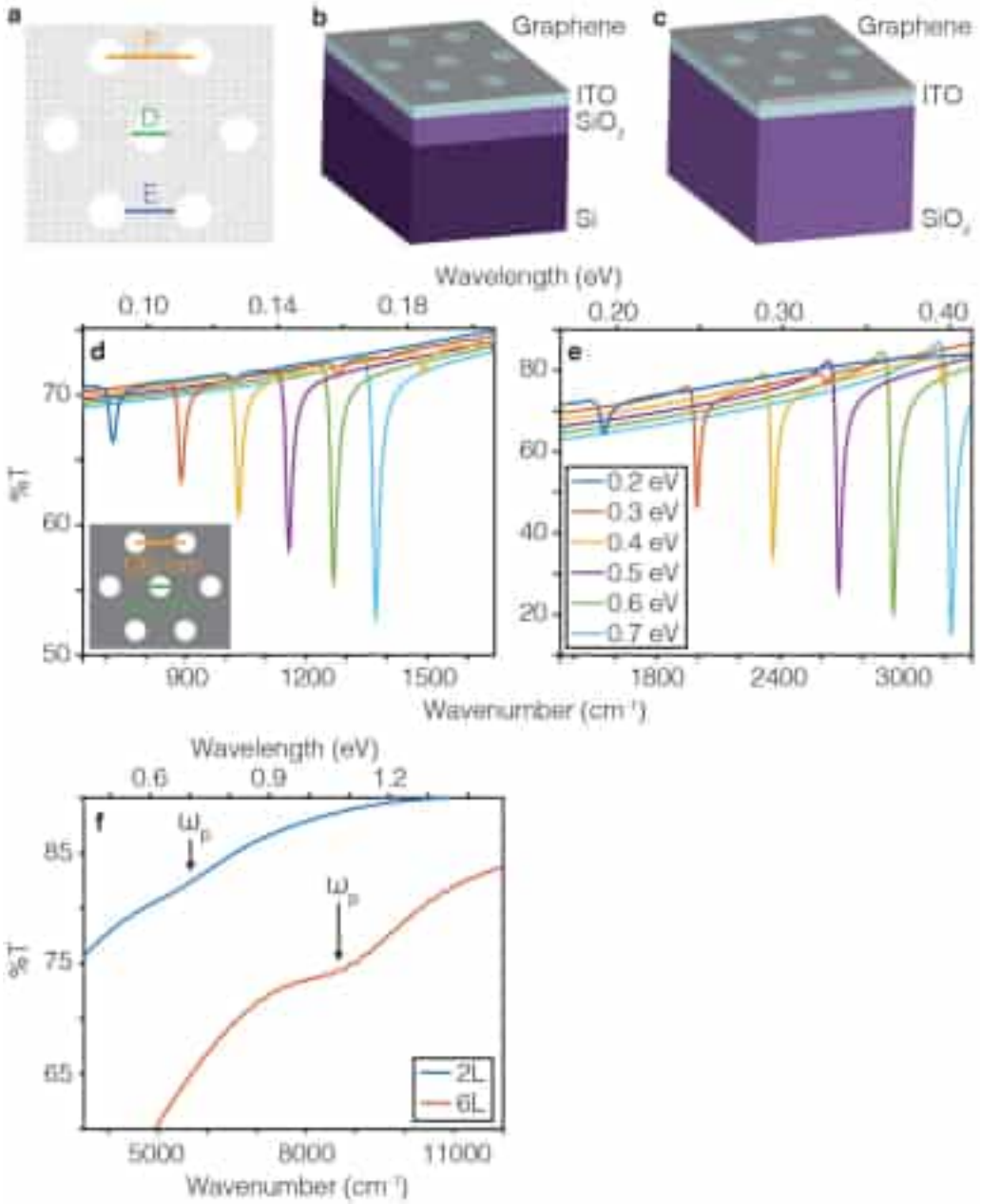


Figure 4.1: Simulation of graphene (a) anti-dot lattices with periodicity P, hole diameter D, and edge-to-edge E separation between the holes. Graphene lattices are on top of a (b) silicon wafer with thermal oxide and ITO layers for THz and MIR simulations and (c) SiO_2 and ITO layers for NIR and VIS simulations. Transmission spectra in the THz and MIR spectra for (d) monolayer (inset shows the lattice parameters) and (e) 6-layer graphene with biases ranging from 0.2 to 0.7 eV, calculated using the 2D conductivity model for graphene. Transmission spectra in the NIR and VIS spectra for (f) 2-layer and 6-layer KC_8, calculated using experimental refractive indexes.

4.3.1 Refractive Index of Doped-Graphene

The refractive index of the doped material is needed to simulate the plasmonic response of graphene with different carrier concentrations. Although the refractive index has inter- and intraband contributions, for low degrees of doping such as those obtained with electrostatic methods, the interband transitions can be ignored and the intraband contributions can be approximated as Drude conductivity as temperature approaches zero.[13] Therefore, for the THz and MIR spectra, we employ a conductivity model where the refractive index depends on angular frequency ω, chemical potential μ_c, scattering rate Γ, and temperature T.[53] In this model, μ_c is the parameter that reflects altering the carrier concentration electrostatically. In our 2D surface conductivity model,[53] we used a temperature of 300 K and a scattering rate of 0.001 eV. We effectively alter the carrier concentration of the graphene by varying the chemical potential from 0.1 to 0.8 eV. Additionally, as the number of layers is increased, the conductivity scales linearly with the thickness. Although the 2D surface conductivity model assumes all carriers are on the surface of the material, the application of this model to FLG is reasonable due to the thinness of the material. At high levels of doping in graphite, such as those achieved with chemical doping, the conductivity model is no longer applicable. In these cases, the material can be treated as a metal. Therefore, we employ the Drude model to calculate the refractive indexes in the visible and NIR spectra of highly-doped graphene. In this work, we use values calculated from experimental data in Ref. 1 to model KC_8.

The Drude model relates the plasmon frequency ω_p to the carrier concentration N and is shown in Equation 4.1

$$\omega_p = \sqrt{\frac{Ne^2}{\epsilon_o m}} \tag{4.1}$$

where e is the charge of an electron, ϵ_o is the permittivity of free space, and m is the effective mass of an electron. In our calculations, ω_p and γ were approximated as unit-less quantities 7.3 and 0.383, respectively, and ε_∞ was assumed to be 8, similar to Ref. 1.

The advantage of the Drude model for metals is that the E_F scales with the square root of the carrier concentration, shown in Equation 4.2. Therefore the E_F also scales linearly with the plasmon resonance where v_F is the Fermi velocity of graphene.

$$E_F = \hbar v_F \sqrt{\pi N} \tag{4.2}$$

Under these assumptions, scaling laws (Equation 4.3) have been developed to determine how the plasmon will shift for any geometrical shape of a 2D conductivity model of graphene in a dot structure,

$$\hbar\omega_p = e\sqrt{-\frac{1}{\pi\eta_j}\Big(\frac{2}{\varepsilon_1+\varepsilon_2}\Big)\frac{E_F}{d}} \tag{4.3}$$

where d is the square root of the graphene area and η_j is a dimensionless value ($\eta_j \approx -\frac{2}{3\pi^2}$ when $\varepsilon_1 = \varepsilon_2 = 1$).[13] These equations provide insights to engineer the plasmon resonance of graphene. As can be seen from Equation 4.1 and 4.3, the ω_p is dependent on the N, E_F, and the dimensions d of a graphene structure. As the N or E_F increase or the dimensions of a structure are reduced, the ω_p will shift to higher frequencies. However, these relations have not been investigated in anti-dot structures. Here, we explore the application and validity of these relations to the low- and high-levels of doped graphene anti-dot arrays.

4.4 Results & Discussion

The plasmonic response of mono- and FLG anti-dot lattices were investigated in simulations. The hole diameter varied from 20 to 50 nm, the periodicity spanned 60 to 120 nm, and flake thickness increased 1 to 6 layers. Furthermore, the carrier concentration doping levels corresponded 0.1 to 1.35 eV with in-plane carrier concentrations of $1 \cdot 10^{12}$ to $5 \cdot 10^{14}$ cm^{-2}. For low-doping levels (e.g. 0.1 - 0.9 eV), a surface conductivity model was used. For higher-doping levels, a 3D model was used.

In the simulations, the incident light interacts most strongly with the carriers at their oscillation frequency. Therefore, the sharp peak in transmission spectra is the ω_p, where the FWHM value is related to the plasmon lifetime. Example transmission spectra of anti-dot arrays with a hole diameter of 40 nm and periodicity of 120 nm (inset, Figure 4.1d) are shown for a monolayer (Figure 4.1d) and 6-layer (Figure 4.1e) graphene flakes. In these spectra, the doping levels span 0.2 – 0.7 eV. Additionally, spectra for 2-layer and 6-layer highly-doped graphite (1.35 eV), simulated using the refractive index of KC_8, are shown (Figure 4.1f). As doping increases from 0.2 to 1.35 eV, the N increases. Based on Equations 4.1 and 4.2, we anticipate a blue-shift in ω_p with doping. In the mono- to 6-layer structures, this is observed in Figure 4.1e-f. More specifically, the ω_p of the monolayer shifts from from $\sim$720 cm^{-1} (THz) at 0.2 eV to $\sim$1,370 cm^{-1} (MIR) at 0.7 eV. For 6-layer graphene, the ω_p shifts from $\sim$1550 cm^{-1} (MIR) at 0.2 eV that shifts to $\sim$3235 cm^{-1} at 0.7 eV. With this anti-dot lattice, the plasmon is pushed very close to the NIR; however the simulated conductivity model is invalid in the NIR and visible spectra. Therefore, we employ a model of KC_8 and find

that the ω_p is positioned at $\sim$8900 cm^{-1} for 2 layers, which are well into the NIR and close to the visible spectra. This structure demonstrates more broadly tunable plasmons in graphene that what have been achieve in any other structure thus far.

As layers increase, the number of carriers increases. Therefore, a blue-shift of the ω_p is expected with thicker samples. This is confirmed in Figure 4.1d-f. We also noted a decrease in the FWHM (Γ_p) as the layers increased (Figure 4.1d-e); this corresponds to an increase in the plasmon lifetime τ_p.[43] Using the uncertainty principle, τ_p is $\hbar/\Gamma_p$, the lifetime increases from 2 fs to 10 fs for monolayer graphene (Figure 4.1d) and from 9 fs to 32 fs for 6 layer graphene (Figure 4.1e), as doping increases from 0.2 to 0.7 eV. The ability to extend the lifetime by a factor of 4-5 with low levels of doping is promising for applications of these anti-dot arrays in sensor applications.

In order to predict what will occur for a given anti-dot array, an understanding is needed of the relationship between the ω_p, the doping level N, the E_F, and the dimensions of the structure. According to the Drude Model shown in Equation 1.1, we anticipated a linear relationship is anticipated between the E_F or $N^{1/2}$ and ω_p for a Drude metal with no interband transitions. However, in these simulations, however, we observed that $\omega_p \propto E_F^{1/2}$, as shown in (Figure 4.2a). This discrepancy is likely due to fact that the 2D conductivity model is the sum of inter-and intraband transitions (Equation 2.8-2.10) and that the interband contributions are not negligible. Furthermore, we explored the application of the scaling law from Equation 4.3 to these anti-dot lattices. As shown in Figure 4.2b, we find that this model applies well to the anti-dot arrays, as indicated by the linear relationship between the area normalized ω_p^2 and E_F. Additionally, it can be seen that the slope is greater for thicker (e.g. 6 layer) than thinner (e.g. 1 layer) graphene (Figure 4.1d-e, 4.2b). This implies that thicker samples can experience large plasmon shifts for a given anti-dot structure than thinner samples.

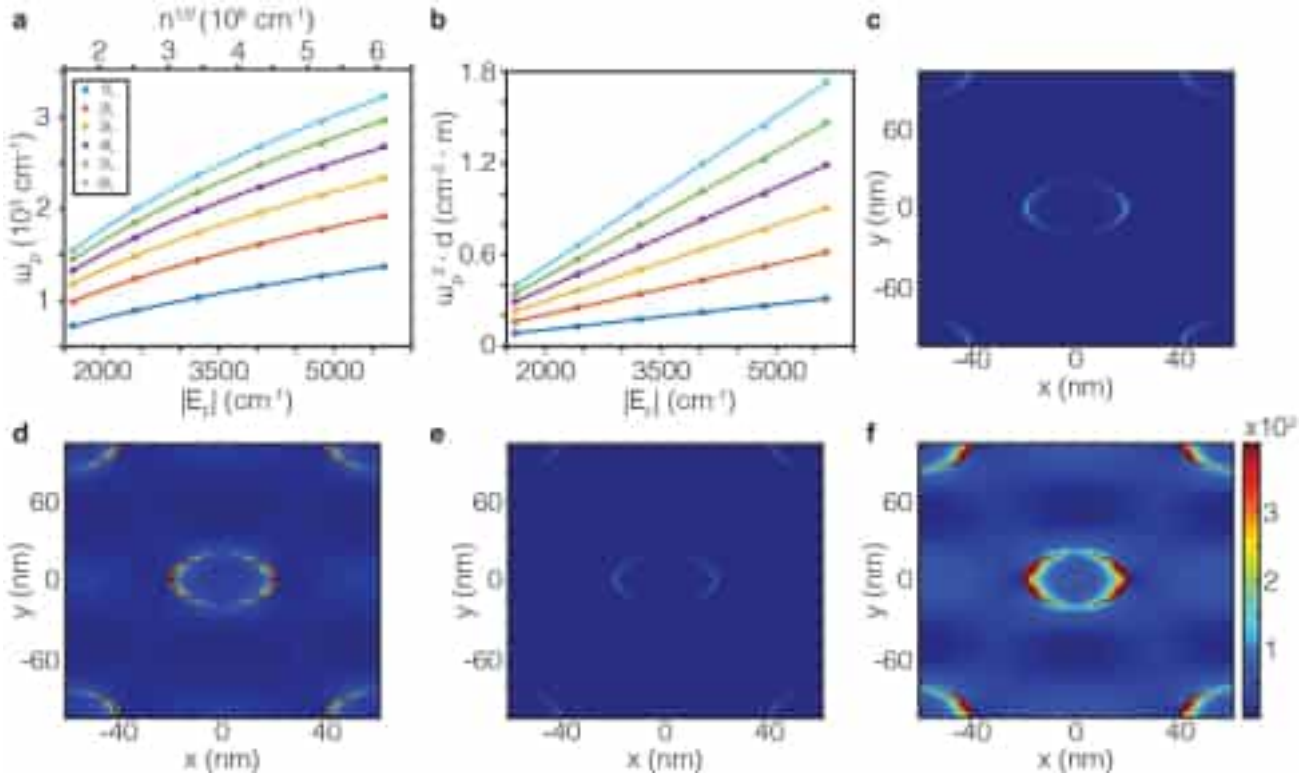


Figure 4.2: For mono- to 6-layer graphene, the (a) non-linear dependence of the ω_p on the fermi energy E_F and carrier concentration $n^{1/2}$ (normalized per layer) and (b) linear dependence of the area normalized ω_p^2 dependence on E_F are shown. The electric field intensity in the graphene anti-dot plane for the 40 nm diameter and 120 nm periodicity structure is depicted for (c) 1 layer with 0.2 eV bias, (d) 1 layer with 0.7 eV bias, (e) 6 layers with 0.2 eV bias, and (f) 6 layers with 0.7 eV bias at each respective ω_p.

Because of the relationships discussed, we expect that the plasmons should be stronger and have longer lifetimes for samples with higher concentrations and a greater number of layers. To investigate this, we simulated the electric field intensity for each structure at its respective ω_p. These electric field intensity profiles are shown for a monolayer (Figure 4.2c-d) and 6-layer graphene structure (Figure 4.2e-f) at 0.2 and 0.7 eV bias, respectively. We observed that the electric field intensity increased as the number of carriers increased (Figure 4.2c-d, e-f). These trends agree with the increased intensity of the ω_p with increased thickness and doping observed in Figure 4.1c-d.

Finally, to understand the effects of geometric parameters on the ω_p, the diameter D, periodicity P, and edge-to-edge E distances were varied (Figure 4.3). We observed that as the D decreases, the ω_p blue-shifts (Figure 4.3 a-c). This trend was consistent for structures where the E distance was constant (70 nm, Figure 4.3a) or P was constant (120 nm, Figure 4.3b). As shown in Figure 4.3 a,b, we did not observe a large

discrepancy between simulations with constant P or constant E when $E > 2D$. Furthermore, as the diameter decreased, ω_p blue-shifted (D = 50 to 20 nm, Figure 4.3c) and the plasmon decreases in intensity (D = 50 to 20 nm, Figure 4.3d,e). Therefore, we observed that the plasmon shift is more sensitive to D and the number of layers than the spacing between the holes in these anti-dot structures.

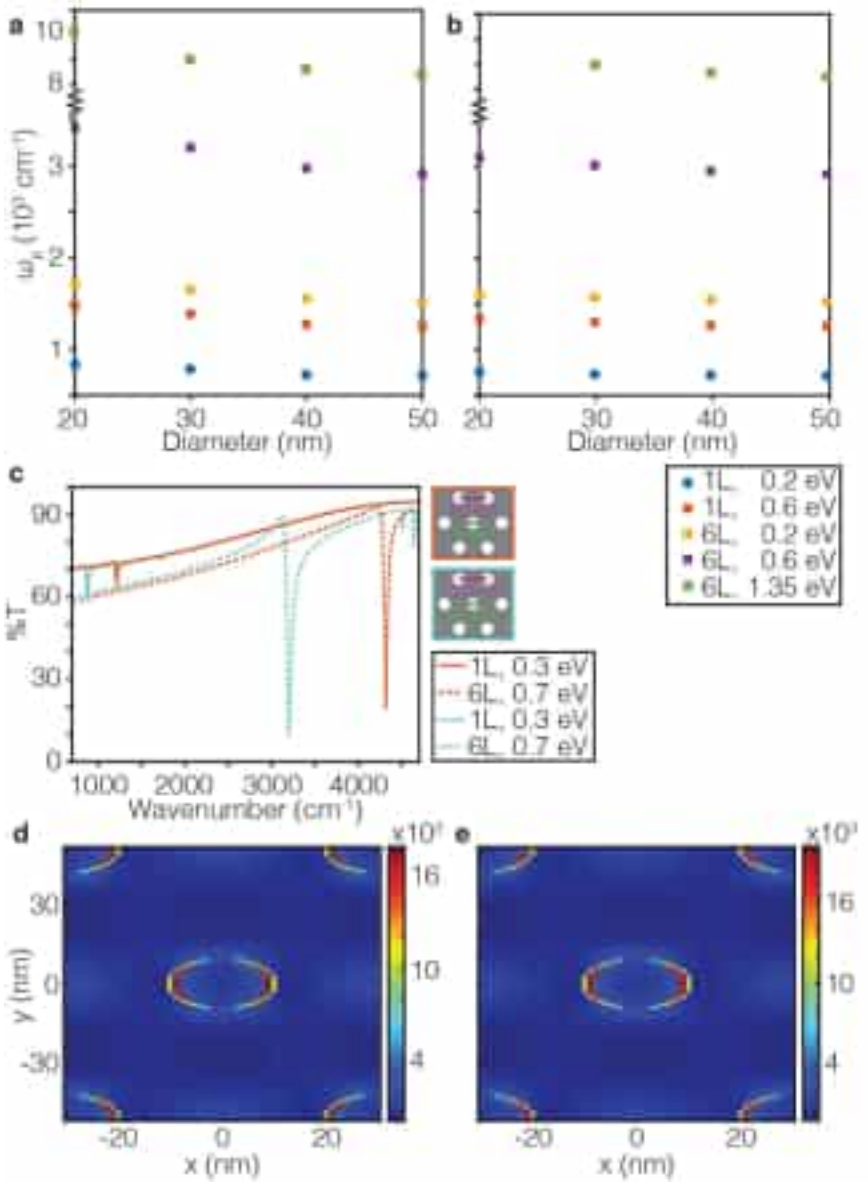


Figure 4.3: The effects of geometric parameters on the ω_p are explored for various diameters with a constant (a) edge-to-edge distance (70 nm) and (b) periodicity (120 nm) at 0.2 eV (circle) and 0.6 eV (square) for monolayers (blue, orange) and 6-layer (yellow, purple) graphene and 6-layer KC_8 (square, green). (c) The transmission spectra for anti-dot structures with a 20 nm diameter, 60 nm periodicity (orange) and 50 nm diameter, 120 nm periodicity (green) are shown for 1 layer at 0.3 eV bias (solid line) and 6 layers at 0.7 eV bias (dashed line). The respective electric field intensity profiles are shown for the 20 nm diameter structure for (d) 1 layer at 0.3 eV, (e) 6 layers at 0.7 eV.

4.5 Conclusion

We find that the ω_p of this anti-dot structure with FLG facilitates the plasmon peak to be shifted from the THz into the NIR, beyond what has been achieved with any other graphene structure.[47] With increased doping and reduced dimensions, we expect that the plasmon should be able to be observed in visible spectrum though varying geometric parameters and doping. We expect that methods such as intercalation may present opportunities to dope FLG sufficiently to blue-shift the plasmon into the visible spectra. This leads to the exciting possibility of promoting NIR and visible graphene plasmonics.

We expect that synthetic methods such as polymer-masking techniques can be utilized to produce large area structures without the need for lithography. Without using typical lithography, we anticipate that these anti-dot structures will experience fewer scattering events due to a lower ratio of edge states, relative to other graphene plasmonic arrays (e.g. dot, ring). Furthermore, since substrates play a crucial role in 2D materials, future work should study the effect of different dielectric environments on ω_p. We anticipate that this hexagonal anti-dot structure will allow for novel and exciting plasmonic modes to be experimentally accessed in mono- and FLG that are readily realizable in experiments.

BIBLIOGRAPHY

"If I have seen further, it is by standing on the shoulders of Giants."

- Isaac Newton

[1] Jung, N.; Kim, B.; Crowther, A. C.; Kim, N.; Nuckolls, C.; Brus, L. E. Optical reflectivity and Raman scattering in few layer thick graphene highly doped by K and Rb. *ACS Nano* **2011**, *5*, 5708–5716.

[2] Bao, W.; Wan, J.; Han, X.; Cai, X.; Zhu, H.; Kim, D.; Ma, D.; Xu, Y.; Munday, J. N.; Drew, H. D.; Fuhrer, M. S.; Hu, L. Approaching the limits of transparency and conductivity in graphitic materials through lithium intercalation. *Nat. Commun.* **2014**, *5*, 4224.

[3] Khrapach, I.; Withers, F.; Bointon, T. H.; Polyushkin, D. K.; Barnes, W. L.; Russo, S.; Craciun, M. F. Novel highly conductive and transparent graphene-based conductors. *Adv. Mater.* **2012**, *24*, 2844–2849.

[4] Xiong, F.; Wang, H.; Liu, X.; Sun, J.; Brongersma, M.; Pop, E.; Cui, Y. Li Intercalation in MoS_2: In Situ observation of its dynamics and tuning optical and electrical properties. *Nano Lett.* **2015**, *15*, 6777–6784.

[5] Sangwan, V. K.; Jariwala, D.; Kim, I. S.; Chen, K. S.; Marks, T. J.; Lauhon, L. J.; Hersam, M. C. Gate-tunable memristive phenomena mediated by grain boundaries in single-layer MoS_2. *Nat. Nanotechnol.* **2015**, *10*, 403–406.

[6] Jung, N.; Kim, N.; Jockusch, S.; Turro, N.; Kim, P.; Brus, L. Charge transfer chemical doping of few layer graphenes: Charge distribution and band gap formation. *Nano Lett.* **2009**, *9*, 4133–4137.

[7] Jung, Y.; Zhou, Y.; Cha, J. J. Intercalation in two-dimensional transition metal chalcogenides. *Inorg. Chem. Front.* **2016**, *3*, 452–463.

[8] Yin, W.; Yan, L.; Yu, J.; Tian, G.; Zhou, L.; Zheng, X.; Zhang, X.; Yong, Y.; Li, J.; Gu, Z.; Zhao, Y. High-throughput synthesis of single-layer MoS_2 nanosheets as a near-infrared photothermal-triggered drug delivery for effective cancer therapy. *ACS Nano* **2014**, *8*, 6922–6933.

[9] Kurapati, R.; Kostarelos, K.; Prato, M.; Bianco, A. Biomedical uses for 2D materials beyond graphene: Current advances and challenges ahead. *Adv. Mater.* **2016**, *28*, 6052–6074.

[10] Jayakumar, A.; Surendranath, A.; Pv, M. 2D materials for next generation healthcare applications. *Int. J. Pharm.* **2018**, *551*, 309–321.

[11] Novoselov, K. S.; Geim, A. K.; Morozov, S. V.; Jiang, D.; Zhang, Y.; Dubonos, S. V.; Grigorieva, I. V.; Firsov, A. A. Electric field effect in atomically thin carbon films. *Science* **2004**, *306*, 666–669.

[12] Zhu, Y.; Murali, S.; Cai, W.; Li, X.; Suk, J. W.; Potts, J. R.; Ruoff, R. S. Graphene and graphene oxide: Synthesis, properties, and applications. *Adv. Mater.* **2010**, *22*, 3906–3924.

[13] García de Abajo, F. J. Graphene plasmonics: Challenges and opportunities. *ACS Photonics* **2014**, *1*, 135–152.

[14] Novoselov, K. S.; Geim, A. K.; Morozov, S. V.; Jiang, D.; Katsnelson, M. I.; Grigorieva, I. V.; Dubonos, S. V.; Firsov, A. A. Two-dimensional gas of massless Dirac fermions in graphene. *Nature* **2005**, *438*, 197–200.

[15] Bolotin, K. I.; Sikes, K. J.; Jiang, Z.; Klima, M.; Fudenberg, G.; Hone, J.; Kim, P.; Stormer, H. L. Ultrahigh electron mobility in suspended graphene. *Solid State Commun.* **2008**, *146*, 351–355.

[16] Green, A. A.; Hersam, M. C. Solution phase production of graphene with controlled thickness via density differentiation. *Nano Lett.* **2009**, *9*, 4031–4036.

[17] Splendiani, A.; Sun, L.; Zhang, Y.; Li, T.; Kim, J.; Chim, C. Y.; Galli, G.; Wang, F. Emerging photoluminescence in monolayer MoS_2. *Nano Lett.* **2010**, *10*, 1271–1275.

[18] Mak, K. F.; Lee, C.; Hone, J.; Shan, J.; Heinz, T. F. Atomically thin MoS_2: A new direct-gap semiconductor. *Phys. Rev. Lett.* **2010**, *105*, 136805.

[19] Radisavljevic, B.; Radenovic, A.; Brivio, J.; Giacometti, V.; Kis, A. Single-layer MoS_2 transistors. *Nat. Nanotechnol.* **2011**, *6*, 147–150.

[20] Molina-Sánchez, A.; Hummer, K.; Wirtz, L. Vibrational and optical properties of MoS_2: From monolayer to bulk. *Surf. Sci. Rep.* **2015**, *70*, 554–586.

[21] Geim, A. K.; Grigorieva, I. V. Van der Waals heterostructures. *Nature* **2013**, *499*, 419–25.

[22] Dean, C. R.; Young, A. F.; Meric, I.; Lee, C.; Wang, L.; Sorgenfrei, S.; Watanabe, K.; Taniguchi, T.; Kim, P.; Shepard, K. L.; Hone, J. Boron nitride substrates for high-quality graphene electronics. *Nature Nanotech.* **2010**, *5*, 722–726.

[23] Hu, J.; Guo, Z.; Mcwilliams, P. E.; Darges, J. E.; Druffel, D. L.; Moran, A. M.; Warren, S. C. Band gap engineering in a 2D material for solar-to-chemical energy conversion. *Nano Lett.* **2015**, *16*, 74–79.

[24] Kuntz, K. L.; Wells, R. A.; Hu, J.; Yang, T.; Dong, B.; Guo, H.; Woomer, A. H.; Dru, D. L.; Alabanza, A.; Tomanek, D.; Warren, S. C. Control of surface and edge oxidation on phosphorene. *ACS Appl. Mater. Interfaces* **2017**, *9*, 9126–9135.

[25] Stark, M. S.; Kuntz, K. L.; Martens, S. J.; Warren, S. C. Intercalation of layered materials from bulk to 2D. *Adv. Mater.* **2019**, *1808213*.

[26] Woomer, A. H.; Farnsworth, T. W.; Hu, J.; Wells, R. A.; Donley, C. L.; Warren, S. C. Phosphorene: Synthesis, scale-up, and quantitative optical spectroscopy. *ACS Nano* **2015**, *9*, 8869–8884.

[27] Rudenko, A. N.; Katsnelson, M. I. Quasiparticle band structure and tight-binding model for single- and bilayer black phosphorus. *Phys. Rev. B* **2014**, *89*, 201408.

[28] Qiao, J.; Kong, X.; Hu, Z.-X.; Yang, F.; Ji, W. High-mobility transport anisotropy and linear dichroism in few-layer black phosphorus. *Nat. Commun.* **2014**, *5*, 1–7.

[29] Liu, Q.; Zhang, X.; Abdalla, L. B.; Fazzio, A.; Zunger, A. Switching a normal insulator into a topological insulator via electric field with application to phosphorene. *Nano Lett.* **2015**, *15*, 1222–1228.

[30] Zhang, S.; Yang, J.; Xu, R.; Wang, F.; Li, W.; Ghufran, M.; Zhang, Y.-W.; Yu, Z.; Zhang, G.; Qin, Q.; Lu, Y. Extraordinary photoluminescence and strong temperature/ angle-dependent raman responses in few-layer phosphorene. *ACS Nano* **2014**, *8*, 9590–9596.

[31] Liang, L.; Wang, J.; Lin, W.; Sumpter, B. G.; Meunier, V.; Pan, M. Electronic bandgap and edge reconstruction in phosphorene materials. *Nano Lett.* **2014**, *14*, 6400–6406.

[32] Akahama, Y.; Endo, S.; Narita, S.-i. Electrical properties of black phosphorus single crystals. *J. Phys. Soc. Jpn.* **1983**, *52*, 2148–2155.

[33] Takao, Y.; Asahina, H.; Morita, A. Electronic structure of black phosphorus in tight binding approach. *J. Phys. Soc. Jpn.* **1981**, *50*, 3362–3369.

[34] Tran, V.; Soklaski, R.; Liang, Y.; Yang, L. Layer-controlled band gap and anisotropic excitons in few-layer black phosphorus. *Phys. Rev. B* **2014**, *89*, 235319.

[35] Lu, J.; Wu, J.; Carvalho, A.; Ziletti, A.; Liu, H.; Tan, J.; Chen, Y.; Castro Neto, A. H.; Özyilmaz, B.; Sow, C. H. Bandgap engineering of phosphorene by laser oxidation toward functional 2D materials. *ACS Nano* **2015**, *9*, 10411–10421.

[36] Ziletti, A.; Carvalho, A.; Trevisanutto, P. E.; Campbell, D. K.; Coker, D. F.; Castro Neto, A. H. Phosphorene oxides: Bandgap engineering of phosphorene by oxidation. *Phys. Rev. B* **2015**, *91*, 085407.

[37] Kim, J.; Baik, S. S.; Ryu, S. H.; Sohn, Y.; Park, S.; Choi, H. J.; Kim, K. S. Observation of tunable band gap and anisotropic Dirac semimetal state in black phosphorus. *Science* **2015**, *349*, 723–727.

[38] Whittingham, M. S.; Jacobson, A. J. *Intercalation chemistry*; 1982.

[39] Dresselhaus, M. S.; Dresselhaus, G. Intercalation compounds of graphite. *Adv. Phys.* **2002**, *51*, 1–186.

[40] Enoki, T.; Suzuki, M.; Endo, M. *Graphite intercalation compounds and applications*; Oxford University Press, 2003.

[41] Nixon, D. E.; Parry, G. S. The expansion of the carbon-carbon bond length in potassium graphites. *J. Phys. C: Solid State Phys.* **1969**, *2*, 1732–1741.

[42] Ashcroft, N. W.; Mermin, N. D. *Solid state physics*, college ed ed.; Brooks/Cole Thomson Learning, Inc.: United States, 1976.

[43] Low, T.; Avouris, P. Graphene plasmonics for terahertz to mid-infrared applications. *ACS Nano* **2014**, *8*, 1086–1101.

[44] Spain, I. In *Chemistry and physics of carbon*; Walker, P., Ed.; 1973; pp 105–110.

[45] Ju, L.; Geng, B.; Horng, J.; Girit, C.; Martin, M.; Hao, Z.; Bechtel, H. A.; Liang, X.; Zettl, A.; Shen, Y. R.; Wang, F. Graphene plasmonics for tunable terahertz metamaterials. *Nature Nanotech.* **2011**, *6*, 630–4.

[46] Yan, H.; Li, Z.; Li, X.; Zhu, W.; Avouris, P.; Xia, F. Infrared spectroscopy of tunable dirac terahertz magneto-plasmons in graphene. *Nano Lett.* **2012**, *12*, 3766–3771.

[47] Fang, Z.; Thongrattanasiri, S.; Schlather, A.; Liu, Z.; Ma, L.; Wang, Y.; Ajayan, P. M.; Nordlander, P.; Halas, N. J.; Garcia de Abajo, F. J. Gated tunability and hybridization of localized plasmons in nanostructured. *ACS Nano* **2013**, *7*, 2388–2395.

[48] Fei, Z.; Andreev, G. O.; Bao, W.; Zhang, L. M.; Mcleod, A. S.; Stewart, M. K.; Zhao, Z.; Dominguez, G.; Thiemens, M.; Fogler, M. M.; Michael, J.; Castro-neto, A. H.; Lau, C. N.; Keilmann, F.; Basov, D. N. Infrared nanoscopy of Dirac plasmons at the graphene-SiO2 interface. *Nano Lett.* **2011**, *11*, 4701–4705.

[49] Abajo, F. J. G. D.; Pruneri, V.; Altug, H. Mid-infrared plasmonic biosensing with graphene. *Science* **2015**, *349*, 165–168.

[50] Fang, Z.; Wang, Y.; Schlather, A. E.; Liu, Z.; Anayan, P. M.; Garcia de Abajo, F. J.; Nordlander, P.; Zhu, X.; Halas, N. J. Active tunable absorption enhancement with graphene nanodisk arrays. *Nano Letters* **2014**, *14*, 299–304.

[51] Chu, H.-s.; Gan, C. H. Active plasmonic switching at mid-infrared wavelengths with graphene ribbon arrays Active plasmonic switching at mid-infrared wavelengths with graphene ribbon arrays. *Appl. Phys. Lett.* **2013**, *102*, 231107.

[52] Chen, C. F.; Park, C. H.; Boudouris, B. W.; Horng, J.; Geng, B.; Girit, C.; Zettl, A.; Crommie, M. F.; Segalman, R. A.; Louie, S. G.; Wang, F. Controlling inelastic light scattering quantum pathways in graphene. *Nature* **2011**, *471*, 617–620.

[53] Hanson, G. W. Dyadic Green's functions and guided surface waves for a surface conductivity model of graphene. *J. Appl. Phys.* **2008**, *103*, 064302.

[54] Shin, S. Y.; Kim, N. D.; Kim, J. G.; Kim, K. S.; Noh, D. Y.; Kim, K. S.; Chung, J. W. Control of the π plasmon in a single layer graphene by charge doping. *Appl. Phys. Lett.* **2011**, *99*.

[55] Ebert, L. B. Intercalation compounds of graphite. *Annu. Rev. Mater. Sci.* **1976**, *6*, 181–211.

[56] Beal, A. R.; Liang, W. Y. Intercalation studies of some transition metal dichalcogenides. *Philos. Mag.* **1973**, *27*, 1397–1416.

[57] Hooley, J. G.; Garby, W. P.; Valentin, J. The effect of sample shape on the bromination of graphite. *Carbon* **1965**, *3*, 7–16.

[58] Hooley, J. G. Physical chemistry and mechanism of intercalation in graphite. *Mater. Sci. Eng.* **1977**, *31*, 17–24.

[59] Favron, A.; Gaufrès, E.; Fossard, F.; Phaneuf-L'Heureux, A.-L.; Tang, N. Y.-W.; Lévesque, P. L.; Loiseau, A.; Leonelli, R.; Francoeur, S.; Martel, R. Photooxidation and quantum confinement effects in exfoliated black phosphorus. *Nat. Mater.* **2015**, *14*, 826–832.

[60] Wood, J. D.; Wells, S. A.; Jariwala, D.; Chen, K.-S.; Cho, E.; Sangwan, V. K.; Liu, X.; Lauhon, L. J.; Marks, T. J.; Hersam, M. C. Effective passivation of exfoliated black phosphorus transistors against ambient degradation. *Nano Lett.* **2014**, *14*, 6964–6970.

[61] Island, J. O.; Steele, G. A.; van der Zant, H. S. J.; Castellanos-Gomez, A. Environmental instability of few-layer black phosphorus. *2D Mater.* **2015**, *2*, 011002.

[62] Ziletti, A.; Carvalho, A.; Campbell, D. K.; Coker, D. F.; Castro Neto, A. H. Oxygen defects in phosphorene. *Phys. Rev. Lett.* **2015**, *114*, 046801.

[63] Edmonds, M. T.; Tadich, A.; Carvalho, A.; Ziletti, A.; O'Donnell, K. M.; Koenig, S. P.; Coker, D. F.; Özyilmaz, B.; Castro Neto, A. H.; Fuhrer, M. S. Creating a stable oxide at the surface of black phosphorus. *ACS Appl. Mater. Interfaces* **2015**, *7*, 14557–14562.

[64] Dreyer, D. R.; Park, S.; Bielawski, C. W.; Ruoff, R. S. The chemistry of graphene oxide. *Chem. Soc. Rev.* **2010**, *39*, 228–240.

[65] Loh, K. P.; Bao, Q.; Eda, G.; Chhowalla, M. Graphene oxide as a chemically tunable platform for optical applications. *Nat. Chem.* **2010**, *2*, 1015–1024.

[66] Schmidt, P.; Binnewies, M.; Glaum, R.; Schmidt, M. *Adv. Top. Cryst. Growth*; 2013; pp 227–305.

[67] Köpf, M.; Eckstein, N.; Pfister, D.; Grotz, C.; Krüger, I.; Greiwe, M.; Hansen, T.; Kohlmann, H.; Nilges, T. Access and in situ growth of phosphorene-precursor black phosphorus. *J. Cryst. Growth* **2014**, *405*, 6–10.

[68] Pisoni, A.; Jacimovic, J.; Barišic, O. S.; Walter, A.; Náfrádi, B.; Bugnon, P.; Magrez, A.; Berger, H.; Revay, Z.; Forrö, L. The role of transport agents in MoS$_2$ single crystals. *J. Phys. Chem. C* **2015**, *119*, 3918–3922.

[69] Vaidya, R.; Dave, M.; Patel, S. S.; Patel, S. G.; Jani, A. R. Growth of molybdenum disulphide using iodine as transport material. *Pramana* **2004**, *63*, 611–616.

[70] Castellanos-Gomez, A.; Buscema, M.; Molenaar, R.; Singh, V.; Janssen, L.; van der Zant, H. S.; Steele, G. A. Deterministic transfer of two-dimensional materials by all-dry viscoelastic stamping. *2D Mater.* **2014**, *1*, 011002.

[71] Parvez, K.; Wu, Z.-S.; Li, R.; Liu, X.; Graf, R.; Feng, X.; Müllen, K. Exfoliation of graphite into graphene in aqueous solutions of inorganic salts. *J. Am. Chem. Soc.* **2014**, *136*, 6083–6091.

[72] Kang, J.; Wells, S. A.; Wood, J. D.; Lee, J.-H.; Liu, X.; Ryder, C. R.; Zhu, J.; Guest, J. R.; Husko, C. A.; Hersam, M. C. Stable aqueous dispersions of optically and electronically active phosphorene. *Proc. Natl. Acad. Sci. U. S. A.* **2016**, *113*, 11688–11693.

[73] Druffel, D. L.; Kuntz, K. L.; Woomer, A. H.; Alcorn, F. M.; Hu, J.; Donley, C. L.; Warren, S. C. Experimental demonstration of an electride as a 2D material. *J. Am. Chem. Soc.* **2016**, *138*, 16089–16094.

[74] Hofmann, U.; Rüdorff, W. The formation of salts from graphite by strong acids. *Trans. Faraday Soc.* **1938**, *34*, 1017–1021.

[75] White, E. R.; Lodico, J. J.; Regan, B. C. Intercalation events visualized in single microcrystals of graphite. *Nat. Commun.* **2017**, *8*, 1–9.

[76] Alcorn, F. M.; Kuntz, K. L.; Druffel, D. L.; Warren, S. C. Aqueous intercalation of graphite at a near-neutral pH. *ACS Appl. Energy Mater.* **2018**, *1*, 5062–5067.

[77] Ponraj, J. S.; Xu, Z.-q.; Chander, S.; Wang, F.; Wang, Z.; Wang, L. 2D materials advances : from large scale synthesis and controlled heterostructures to improved characterization techniques, defects and applications. *2D Mater.* **2016**, *3*, 1–38.

[78] Steinbrenner, U.; Adler, P.; Hölle, W.; Simon, A. Electronic structure and chemical bonding in alkaline earth metal subnitrides: Photoemission studies and band structure calculations. *J. Phys. Chem. Solids* **1998**, *59*, 1527–1536.

[79] Demri, B.; Muster, D. XPS study of some calcium compounds. *J. Mater. Process. Technol.* **1995**, *55*, 311–314.

[80] Lee, K.; Kim, S. W.; Toda, Y.; Matsuishi, S.; Hosono, H. Dicalcium nitride as a two-dimensional electride with an anionic electron layer. *Nature* **2013**, *494*, 336–40.

[81] Druffel, D. L.; Woomer, A. H.; Kuntz, K. L.; Pawlik, J. T.; Warren, S. C. Electrons on the surface of 2D materials: from layered electrides to 2D electrenes. *J. Mater. Chem. C* **2017**, *5*, 11196–11213.

[82] Kresse, G.; Joubert, D. From ultrasoft pseudopotentials to the projector augmented-wave method. *Phys. Rev. B* **1999**, *59*, 1758–1775.

[83] Kresse, G.; Furthmüller, J. Efficient iterative schemes for ab initio total-energy calculations using a plane-wave basis set. *Phys. Rev. B* **1996**, *54*, 11169–11186.

[84] Perdew, J. P.; Burke, K.; Ernzerhof, M. Generalized gradient approximation made simple. *Phys. Rev. Lett.* **1996**, *77*, 3865–3868.

[85] Tománek, D.; Kumar, V.; Holloway, S.; Bennemann, K. H. Semiempirical theory for surface core-level shifts. *Solid State Commun.* **1982**, *41*, 273–279.

[86] Grunze, M.; Brundle, C. R.; Tomanek, D. Adsoprtion and decomposition of ammonia on a W(110) surface: Photoemissison fingerprinting and interpretation of the core level binding energies using the equivalen core approximation. *Surf. Sci.* **1982**, *119*, 133–149.

[87] Tománek, D.; Dowben, P. A.; Grunze, M. Thermodynamic interpretation of core-level binding energies in adsorbates. *Surf. Sci.* **1983**, *126*, 112–119.

[88] Yang, T.; Dong, B.; Wang, J.; Zhang, Z.; Guan, J.; Kuntz, K.; Warren, S. C.; Tom, D. Interpreting core-level spectra of oxidizing phosphorene : Theory and experiment. *Phys. Rev. B* **2015**, *92*, 125412.

[89] Johansson, B.; Mårtensson, N. Core-level binding-energy shifts for the metallic elements. *Phys. Rev. B* **1980**, *21*, 4427–4457.

[90] Sugai, S.; Ueda, T.; Murase, K. Pressure dependence of the lattice vibration in the orthorhombic and rhombohedral structures of black phosphorus. *J. Phys. Soc. Jpn.Jpn.* **1981**, *50*, 3356–3361.

[91] Sugai, S.; Shirotani, I. Raman and infrared reflection spectroscopy in black phosphorus. *Solid State Commun.* **1985**, *53*, 753–755.

[92] Xia, F.; Wang, H.; Jia, Y. Rediscovering black phosphorus as an anisotropic layered material for optoelectronics and electronics. *Nat. Commun.* **2014**, *5*, 5458.

[93] Zhang, J. M.; Eklund, P. C. Optical transmission of graphite and potassium graphite intercalation compounds. *J. Mater. Res.* **2011**, *2*, 858–863.

[94] Zhang, H.; Shen, W.; Wang, Z.; Zhang, F. Formation of iron chloride-graphite intercalation compounds in propylene carbonate by electrolysis. *Carbon* **1997**, *35*, 285–290.

[95] Kang, F.; Leng, Y.; Zhang, T.-Y.; Li, B. Electrochemical synthesis and characterization of ferric chloride-graphite intercalation compounds in aqueous solution. *Carbon* **1998**, *36*, 383–390.

[96] Luo, W.; Wan, J.; Ozdemir, B.; Bao, W.; Chen, Y.; Dai, J.; Lin, H.; Xu, Y.; Gu, F.; Barone, V.; Hu, L. Potassium ion batteries with graphitic materials. *Nano Lett.* **2015**, *15*, 7671–7677.

[97] Zhao, J.; Zou, X.; Zhu, Y.; Xu, Y.; Wang, C. Electrochemical intercalation of potassium into graphite. *Adv. Funct. Mater.* **2016**, *26*, 8103–8110.

[98] Pourbaix M., Atlas of electrochemical equilibria in aqueous solutions version 2. 1974.

[99] Zhao, W.; Tan, P. H.; Liu, J.; Ferrari, A. C. Intercalation of few-layer graphite flakes with FeCl3: Raman determination of Fermi level, layer by layer decoupling, and stability. *J. Am. Chem. Soc.* **2011**, *133*, 5941–5946.

[100] Chen, D.; Feng, H.; Li, J. Graphene oxide: Preparation, functionalization, and electrochemical applications. *Chem. Rev.* **2012**, *112*, 6027–6053.

[101] Ryder, C. R.; Wood, J. D.; Wells, S. A.; Yang, Y.; Jariwala, D.; Marks, T. J.; Schatz, G. C.; Hersam, M. C. Covalent functionalization and passivation of exfoliated black phosphorus via aryl diazonium chemistry. *Nat. Chem.* **2016**, *8*, 597–602.

[102] Hu, W.; Lin, L.; Yang, C.; Dai, J.; Yang, J. Edge-modified phosphorene nanoflake heterojunctions as highly efficient solar cells. *Nano Lett.* **2016**, *16*, 1675–1682.

[103] Wang, X.; Jones, A. M.; Seyler, K. L.; Tran, V.; Jia, Y.; Zhao, H.; Wang, H.; Yang, L.; Xu, X.; Xia, F. Highly anisotropic and robust excitons in monolayer black phosphorus. *Nature Nanotech.* **2015**, *10*, 517–521.

[104] Yuan, H. et al. Polarization-sensitive broadband photodetector using a black phosphorus vertical p–n junction. *Nature Nanotech.* **2015**, *10*, 707–713.

[105] Buscema, M.; Groenendijk, D. J.; Blanter, S. I.; Steele, G. A.; van der Zant, H. S. J.; Castellanos-Gomez, A. Fast and broadband photoresponse of few-layer black phosphorus field-effect transistors. *Nano Lett.* **2014**, *14*, 3347–3352.

[106] Liu, H.; Neal, A. T.; Zhu, Z.; Luo, Z.; Xu, X.; Tománek, D.; Ye, P. D. Phosphorene: an unenexplored 2D semiconductor with a high hole mobility. *ACS Nano* **2014**, *8*, 4033–4041.

[107] Buscema, M.; Groenendijk, D. J.; Steele, G. A.; van der Zant, H. S. J.; Castellanos-Gomez, A. Photovoltaic effect in few-layer black phosphorus PN junctions defined by local electrostatic gating. *Nat. Commun.* **2014**, *5*, 4651.

[108] Li, L.; Yu, Y.; Ye, G. J.; Ge, Q.; Ou, X.; Wu, H.; Feng, D.; Chen, X. H.; Zhang, Y. Black phosphorus field-effect transistors. *Nat. Nanotechnol.* **2014**, *9*, 372–377.

[109] Koenig, S. P.; Doganov, R. A.; Schmidt, H.; Castro Neto, A. H.; Özyilmaz, B. Electric field effect in ultrathin black phosphorus. *Appl. Phys. Lett.* **2014**, *104*, 103106.

[110] Dai, J.; Zeng, X. C. Bilayer phosphorene: Effect of stacking order on bandgap and its potential applications in thin-film solar cells. *J. Phys. Chem. Lett.* **2014**, *5*, 1289–1293.

[111] Deng, Y.; Luo, Z.; Conrad, N. J.; Liu, H.; Gong, Y.; Najmaei, S.; Ajayan, P. M.; Lou, J.; Xu, X.; Ye, P. D. Black phosphorus–monolayer MoS_2 van der Waals heterojunction p–n diode. *ACS Nano* **2014**, *8*, 8292–8299.

[112] Baba, M.; Takeda, Y.; Shibata, K.; Ikeda, T.; Morita, A. Optical properties of black phosphorus and its application to the infrared detector. *Jpn. J. Appl. Phys.* **1989**, *28*, L2104–L2106.

[113] Engel, M.; Steiner, M.; Avouris, P. Black phosphorus photodetector for multispectral, high-resolution imaging. *Nano Lett.* **2014**, *14*, 6414–6417.

[114] Park, C.-M.; Sohn, H.-J. Black phosphorus and its composite for lithium rechargeable batteries. *Adv. Mater.* **2007**, *19*, 2465–2468.

[115] Sun, J.; Zheng, G.; Lee, H.-W.; Liu, N.; Wang, H.; Yao, H.; Yang, W.; Cui, Y. Formation of stable phosphorus-carbon bond for enhanced performance in black phosphorus nanoparticle-graphite composite battery anodes. *Nano Lett.* **2014**, *14*, 4573–4580.

[116] Abbas, A. N.; Liu, B.; Chen, L.; Ma, Y.; Cong, S.; Aroonyadet, N.; Köpf, M.; Nilges, T.; Zhou, C. Black phosphorus gas sensors. *ACS Nano* **2015**, *9*, 5618–5624.

[117] Yasaei, P.; Behranginia, A.; Foroozan, T.; Asadi, M.; Kim, K.; Khalili-Araghi, F.; Salehi-Khojin, A. Stable and selective humidity sensing using stacked black phosphorus flakes. *ACS Nano* **2015**, *9*, 9898–9905.

[118] Yao, Y.; Zhang, H.; Sun, J.; Ma, W.; Li, L.; Li, W.; Du, J. Novel QCM humidity sensors using stacked black phosphorus nanosheets as sensing film. *Sens. Actuators, B* **2017**, *244*, 259–264.

[119] Wang, H.; Yang, X.; Shao, W.; Chen, S.; Xie, J.; Zhang, X.; Wang, J.; Xie, Y. Ultrathin black phosphorus nanosheets for efficient singlet oxygen generation. *J. Am. Chem. Soc.* **2015**, *137*, 11376–11382.

[120] Sun, Z.; Xie, H.; Tang, S.; Yu, X.-F.; Guo, Z.; Shao, J.; Zhang, H.; Huang, H.; Wang, H.; Chu, P. K. Ultrasmall black phosphorus quantum dots: Synthesis and use as photothermal agents. *Angew. Chem., Int. Ed.* **2015**, *54*, 11526–11530.

[121] Gamage, S.; Li, Z.; Yakovlev, V. S.; Lewis, C.; Wang, H.; Cronin, S. B.; Abate, Y. Nanoscopy of black phosphorus degradation. *Adv. Mater. Interfaces* **2016**, *3*, 1600121.

[122] Huang, Y.; Qiao, J.; He, K.; Bliznakov, S.; Sutter, E.; Chen, X.; Luo, D.; Meng, F.; Su, D.; Decker, J.; Ji, W.; Ruoff, R. S.; Sutter, P. Interaction of black phosphorus with oxygen and water. *Chem. Mater.* **2016**, *28*, 8330–8339.

[123] Luo, W.; Zemlyanov, D. Y.; Milligan, C. A.; Du, Y.; Yang, L.; Wu, Y.; Ye, P. D. Surface chemistry of black phosphorus under a controlled oxidative environment. *Nanotechnology* **2016**, *27*, 434002.

[124] Serrano-Ruiz, M.; Caporali, M.; Ienco, A.; Piazza, V.; Heun, S.; Peruzzini, M. The role of water in the preparation and stabilization of high-quality phosphorene flakes. *Adv. Mater. Interfaces* **2016**, *3*, 1500441.

[125] Gan, Z. X.; Sun, L. L.; Wu, X. L.; Meng, M.; Shen, J. C.; Chu, P. K. Tunable photoluminescence from sheet-like black phosphorus crystal by electrochemical oxidation. *Appl. Phys. Lett.* **2015**, *107*, 021901.

[126] Wang, G. X.; Pandey, R.; Karna, S. P. Phosphorene oxide: stability and electronic properties of a novel two-dimensional material. *Nanoscale* **2015**, *7*, 524–531.

[127] Yau, S.-L.; Moffat, T. P.; Bard, A. J.; Zhang, Z.; Lerner, M. M. STM of the (010) surface of orthorhombic phosphorus. *Chem. Phys. Lett.* **1992**, *198*, 383–388.

[128] Pei, J.; Gai, X.; Yang, J.; Wang, X.; Yu, Z.; Choi, D.-Y.; Luther-Davies, B.; Lu, Y. Producing air-stable monolayers of phosphorene and their defect engineering. *Nat. Commun.* **2016**, *7*, 10450.

[129] Kwon, H.; Seo, S. W.; Kim, T. G.; Lee, E. S.; Lanh, P. T.; Yang, S.; Ryu, S.; Kim, J. W. Ultrathin and flat layer black phosphorus fabricated by reactive oxygen and water rinse. *ACS Nano* **2016**, *10*, 8723–8731.

[130] Wang, G.; Slough, W. J.; Pandey, R.; Karna, S. P. Degradation of phosphorene in air: understanding at atomic level. *2D Mater.* **2016**, *3*, 25011.

[131] Castellanos-Gomez, A.; Vicarelli, L.; Prada, E.; Island, J. O.; Narasimha-Acharya, K. L.; Blanter, S. I.; Groenendijk, D. J.; Buscema, M.; Steele, G. A.; Alvarez, J. V.; Zandbergen, H. W.; Palacios, J. J.; van der Zant, H. S. J. Isolation and characterization of few-layer black phosphorus. *2D Mater.* **2014**, *1*, 025001.

[132] Li, L.; Yu, Y.; Meng, F.; Tan, Y.; Hamers, R. J.; Jin, S. Facile solution synthesis of alpha-FeF3 3H2O nanowires and their conversion to alpha-Fe2O3 nanowires for photoelectrochemical application. *Nano Lett.* **2012**, *12*, 724–731.

[133] Hayasi, Y.; Takahashi, T.; Asahina, H.; Sagawa, T.; Morita, A.; Shirotani, I. Electronic structure of black phosphorus studied by polarized soft-x-ray emission and absorption spectroscopy. *Phys. Rev. B* **1984**, *30*, 1891–1895.

[134] Taniguchi, M.; Suga, S.; Seki, M.; Sakamoto, H.; Kanzaki, H.; Akahama, Y.; Terada, S.; Endo, S.; Narita, S. Valence band and core-level photoemission spectra of black phosphorus single crystals. *Solid State Commun.* **1983**, *45*, 59–61.

[135] Moffat, T. P.; Latanision, R. M.; Ruf, R. R. An X-ray photoelectron spectroscopy study of chromium-metalloid alloys-III. *Electrochim. Acta* **1995**, *40*, 1723–1734.

[136] Henkelman, G.; Arnaldsson, A.; Jónsson, H. A fast and robust algorithm for Bader decomposition of charge density. *Comput. Mater. Sci.* **2006**, *36*, 354–360.

[137] Cai, Y.; Zhang, G.; Zhang, Y.-W. Layer-dependent band alignment and work function of few-layer phosphorene. *Sci. Rep.* **2014**, *4*, 6677.

[138] Wang, V.; Kawazoe, Y.; Geng, W. T. Native point defects in few-layer phosphorene. *Phys. Rev. B* **2015**, *91*, 045433.

[139] Koppenol, W. H.; Stanbury, D. M.; Bounds, P. L. Electrode potentials of partially reduced oxygen species, from dioxygen to water. *Free Radicals Biol. Med.* **2010**, *49*, 317–322.

[140] Rao, P. S.; Hayon, E. Experimental determination of the redox potential of the superoxide radical $O_2^{\cdot -}$. *Biochem. Biophys. Res. Commun.* **1973**, *51*, 468–473.

[141] Wood, P. M. The redox potential of the system oxygen-superoxide. *FEBS Lett.* **1974**, *44*, 22–24.

[142] Ilan, Y. A.; Czapski, G.; Meisel, D. The one-electron transfer redox potentials of free radicals. I. The oxygen/superoxide system. *Biochim. Biophys. Acta, Bioenerg.* **1976**, *430*, 209–224.

[143] Sawyer, D. T.; Valentine, J. S. How super is superoxide? *Acc. Chem. Res.* **1981**, *14*, 393–400.

[144] Koppenol, W. H.; Butler, J. Energetics of interconversion reactions of oxyradicals. *Adv. Free Radical Biol. Med.* **1985**, *1*, 91–131.

[145] Buettner, G. R. The pecking order of free radicals and antioxidants: Lipid peroxidation, α-tocopherol, and ascorbate. *Arch. Biochem. Biophys.* **1993**, *300*, 535–543.

[146] Brar, V. W.; Jang, M. S.; Sherrott, M.; Lopez, J. J.; Atwater, H. A. Highly confined tunable mid-infrared plasmonics in graphene nanoresonators. *Nano Letters* **2013**, *13*, 2541–2547.

[147] Bellunato, A.; Tash, H. A.; Cesa, Y.; Schneider, G. F. Chemistry at the edge of graphene. *ChemPhysChem* **2016**, *17*, 785–801.

[148] Li, M.; Cushing, S. K.; Wu, N. Plasmon-enhanced optical sensors: A review. *Analyst* **2015**, *140*, 386–406.

[149] Atwater, H. A.; Polman, A. Plasmonics for improved photovoltaic devices. *Nat. Mater.* **2010**, *9*, 205–213.

[150] Xu, G.; Tazawa, M.; Jin, P.; Nakao, S.; Yoshimura, K. Wavelength tuning of surface plasmon resonance using dielectric layers on silver island films. *Appl. Phys. Lett.* **2003**, *82*, 3811–3813.

[151] Efetov, D. K.; Kim, P. Controlling electron-phonon interactions in graphene at ultrahigh carrier densities. *Phys. Rev. Lett.* **2010**, *105*, 2–5.

[152] Chen, J.; Badioli, M.; Alonzo-Gonzalez, P.; Thongrattanasiri, S.; Huth, F.; Osmond, J.; Spasenovic, M.; Centeno, A.; Pesquera, A.; Godignon, P.; Elorza, A. Z.; Camara, N.; Garcia de Abajo, F. J.; Hillenbrand, R.; Koppens, F. H. L. Optical nano-imaging of gate-tunable graphene plasmons. *Nature* **2012**, *487*, 77–81.

[153] Fei, Z.; Rodin, A. S.; Andreev, G. O.; Bao, W.; Mcleod, A. S.; Wagner, M. Gate-tuning of graphene plasmons revealed by infrared nano-imaging. *Nature* **2012**, *487*, 82–85.

[154] Manjavacas, A.; Marchesin, F.; Thongrattanasiri, S.; Koval, P.; Nordlander, P.; Sánchez-Portal, D.; García De Abajo, F. J. Tunable molecular plasmons in polycyclic aromatic hydrocarbons. *ACS Nano* **2013**, *7*, 3635–3643.